

---

# Information-Driven Design of Imaging Systems

---

Henry Pinkard

Leyla Kabuli

Eric Markley

Tiffany Chien

Jiantao Jiao

Laura Waller

Department of Electrical Engineering and Computer Sciences, UC Berkeley

## Abstract

In modern imaging systems that computationally process raw measurements before or instead of human viewing, information content matters more than visual appearance. However, developing information estimators that can handle the complexity of real-world measurements yet remain practical enough for widespread use has proven challenging. We introduce a data-driven approach for estimating mutual information between unknown objects and their noisy measurements. Our technique fits probabilistic models to measurements and their noise processes, quantifying information content without requiring ground truth data or making assumptions about object structure. We validate our approach across diverse applications—color photography, radio astronomy, lensless imaging, and microscopy—demonstrating that information estimates reliably predict system performance. Finally, we introduce Information-Driven Encoder Analysis Learning (IDEAL), which optimizes imaging systems to maximize information capture. Our work unlocks information theory as a powerful, practical tool for analyzing and designing imaging systems across a broad range of applications.

A video summarizing this work can be found at:

<https://waller-lab.github.io/EncodingInformationWebsite/>

## 1 Introduction

Imaging systems have traditionally been designed to mimic the human eye and produce visually interpretable pictures. Today, however, algorithms process most imaging data before or instead of human viewing.

Unlike human vision, which is inherently sensitive to specific visual patterns [1], algorithms like modern deep neural networks can extract meaning from information encoded in many forms. Computational imaging systems [2] often leverage these capabilities by extracting image features that are not visually apparent in raw measurements.

This shift fundamentally changes what limits performance: not *how well* systems encode information into human-perceptible patterns, but *how much* information they encode, regardless of its form. Quantifying information content thus offers a powerful tool for designing better ways to capture data.

The information content of measurements is often assessed indirectly after computational decoding, which presents significant limitations. In this approach, a decoding algorithm processes raw measurements to perform downstream tasks (e.g., reconstructing the original object), the result of which is compared to ground truth data to calculate performance metrics [2–4]. Since this approach evaluates the encoder (hardware) and decoder (algorithm) simultaneously, it leaves ambiguity about whether to focus improvement efforts on hardware or algorithms. For example, many decoders use

assumptions about the original object that affect performance yet have no relation to measurement quality. Additionally, this method requires ground truth data for comparison, which usually cannot be obtained in experimental settings.

Alternatively, the information content in raw measurements can be directly quantified: mutual information quantifies how much object information survives the encoding and measurement process [5–29, 3]. This approach is independent of measurement visual appearance or downstream processing. It unifies traditionally separate metrics like resolution and signal-to-noise ratio, and accounts for effects such as quantization and sampling [9, 17, 30]. As a result, mutual information enables objective evaluation of design tradeoffs affecting multiple aspects of system performance (**Sec. S1.2**).

Despite these benefits, accurately estimating information content in real imaging systems has proven challenging. Previous approaches fall into two categories. The first calculates theoretical limits [5, 7–10, 15, 20, 29] that, while powerful for communication systems (in which the encoder can map any input to any output), produce overly optimistic bounds that fail to account for the physical constraints of real imaging systems (**Fig. S6**). The second develops analytical probabilistic models of objects that work in specific cases but require domain-specific assumptions that are difficult to validate experimentally.

In this work, we introduce an information estimation framework that achieves the best of both worlds: it inherently captures physical constraints by evaluating real measurements, while avoiding domain-specific model development. Our approach requires just two inputs: a dataset of measurements and a characterization of system noise. First, we estimate the measurements’ entropy by fitting a probabilistic model to them. Then we subtract the estimated entropy due to noise, giving a measure of the information about the object that is passed into the measurement. By eliminating the need for assumptions about the imaged object or imaging system, our approach can evaluate diverse imaging modalities with complicated performance tradeoffs under real-world conditions.

In the following sections, we describe our information estimation framework and experimentally validate its performance. We then demonstrate its practical utility across diverse imaging domains: color photography, black hole radio astronomy, non-traditional optics in lensless cameras, and biological microscopy. Finally, we introduce Information-Driven Encoder Analysis (IDEAL), which transforms our evaluation framework into a design tool by combining it with gradient-based optimization. This enables automated design of imaging systems optimized for maximum information capture.

## 2 Formulation of information estimator

Mutual information estimation requires modeling objects, images, and measurements as probability distributions (**Fig. 1**). For example, a probability distribution over tree **objects** captures the relative likelihood of each possible variation in size, shape, and species. When we apply an encoder (e.g. capturing an image using a camera with a particular lens and position) to each possible object, we obtain a noiseless **image** distribution, such as the images of each possible tree on a 2D sensor. Random noise then corrupts these noiseless images to create the **measurement** distribution we actually observe [5, 14, 22, 31, 32] (**Sec. S1**).

Within this probabilistic framework, we aim to quantify how effectively different encoders preserve information about the object. Each encoder represents a different system design; “good” encoders will preserve information throughout the system. Information can be lost both during the encoding process (e.g. due to finite resolution or sampling) or during the measurement process (e.g. due to noise). The mutual information between object and measurement distributions quantifies how much object information survives this entire process.

Mathematically, we represent an image with  $D$  pixels as a vector  $\mathbf{x} = (x_1, x_2, \dots, x_D)$ , where  $x_k$  is the energy at the  $k$ th pixel of an image sensor. The probability distribution over images is given by the  $D$ -dimensional joint distribution over pixels  $p(\mathbf{x}) = p(x_1, x_2, \dots, x_D)$ , which gives the probability of each possible image. Similarly, we represent the noisy measurement as  $\mathbf{y} = (y_1, y_2, \dots, y_D)$  with probability density  $p(\mathbf{y})$ .

Our goal is to estimate the mutual information between object and measurement,  $I(\mathbf{O}; \mathbf{Y})$ , which quantifies how well measurements can distinguish different objects (**Sec. S2.4**). To accomplish this in

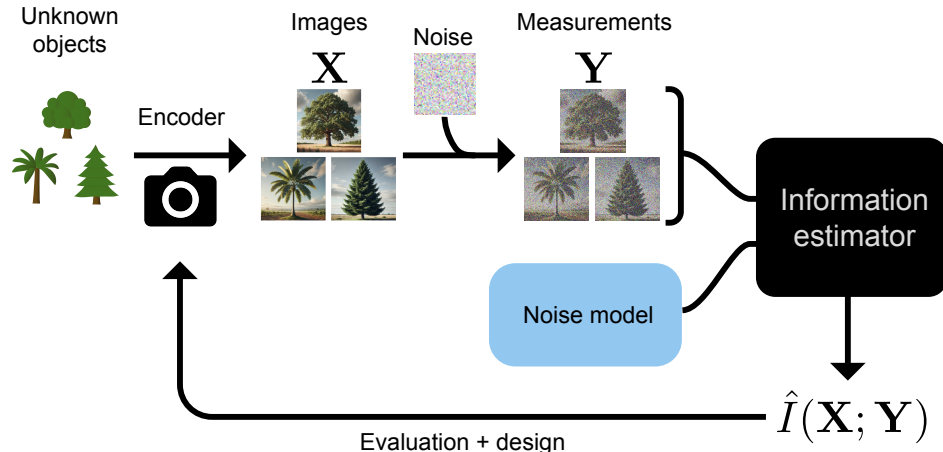


Figure 1: **Information estimation for imaging systems.** An encoder (i.e., an optical system) maps unknown objects to noiseless images  $\mathbf{X}$ , which noise corrupts to produce measurements  $\mathbf{Y}$ . Our information estimator takes these measurements and a noise model as inputs to quantify how well different objects can be distinguished. We can use the estimate  $\hat{I}(\mathbf{X}; \mathbf{Y})$  to evaluate existing systems or guide the design of new ones.

experimental settings, we must work with only a dataset of measurement samples  $\{\mathbf{y}^{(i)}\}_1^N$ , without making any assumptions about the underlying object or image distributions.

We cannot directly estimate  $I(\mathbf{O}; \mathbf{Y})$  without access to the object distribution. Fortunately, for most imaging systems, we can instead focus on  $I(\mathbf{X}; \mathbf{Y})$  (the mutual information between noiseless image and noisy measurement distributions). This approach simplifies our task because it depends only on the noiseless image and noisy measurement distributions. This simplification is valid for imaging systems that always produce the same noiseless image for a given object. In such cases, all information in a noiseless image comes from the object, and any information in an image that is not destroyed by noise during the measurement process must have also come from the object. Mathematically,  $I(\mathbf{O}; \mathbf{Y}) = I(\mathbf{X}; \mathbf{Y})$ . (In situations where  $I(\mathbf{O}; \mathbf{Y}) \neq I(\mathbf{X}; \mathbf{Y})$  because of an additional source of randomness, such as a changing encoder, the estimator can be adapted to account for this using additional system calibration data (Sec. S1.5.1)).

Estimating mutual information between high-dimensional variables from samples is notoriously challenging [33–42]. Without strong assumptions, estimation requires sample sizes that grow exponentially with dimensionality, suffers from high bias and variance, and lacks formal guarantees [43, 38]. While numerous methods exist for estimating using paired samples  $\{\mathbf{x}^{(i)}, \mathbf{y}^{(i)}\}_1^N$ , for physical instruments like imaging systems, we face a fundamental limitation: we typically only have access to noisy measurements  $\{\mathbf{y}^{(i)}\}_1^N$ .

However, imaging systems offer a key simplification: the noise process  $p(\mathbf{y} | \mathbf{x})$  [32] is often well-characterized through physical models or empirical calibration. This enables decomposing  $I(\mathbf{X}; \mathbf{Y})$  into entropy terms that can be estimated from noisy measurements alone:

$$I(\mathbf{X}; \mathbf{Y}) = H(\mathbf{Y}) - H(\mathbf{Y}|\mathbf{X}) \quad (1)$$

These entropies quantify the amount of variation, or diversity, in each distribution; a measure of how unpredictable the pixel values are. Here,  $H(\mathbf{Y})$  quantifies the total entropy in the measurements, arising from both object information and noise. To isolate object information, we subtract  $H(\mathbf{Y}|\mathbf{X})$ , the entropy due to noise alone. This difference,  $I(\mathbf{X}; \mathbf{Y})$ , thus gives our desired metric – the measurement entropy that comes from object variations, which quantifies how well the encoder preserves object information.

The two terms in Eq. 1 can be written explicitly in terms of probability distributions:

$$H(\mathbf{Y}) = \mathbb{E}[-\log p(\mathbf{Y})] \quad (2)$$

$$H(\mathbf{Y}|\mathbf{X}) = \mathbb{E}[-\log p(\mathbf{Y} | \mathbf{X})] \quad (3)$$

The second term (**Eq. 3**) can be simplified when the noise at each pixel is independent of other pixels conditioned on the noiseless image—a common assumption in models of imaging systems [32] (**Sec. S2.3**). This reduces the computation of  $H(\mathbf{Y}|\mathbf{X})$  to a sum  $\sum_{i=1}^D H(Y_i|X_i)$  of the conditional entropies at each pixel (**Sec. S2.3.1**), avoiding an intractable high-dimensional integral.

The first term (**Eq. 2**) presents a greater challenge since we don’t know the true distribution of measurements  $p(\mathbf{y})$ . To address this, we fit a parametric model  $p_\theta(\mathbf{y})$  to a training set of  $N$  measurements  $\{\mathbf{y}^{(i)}\}_i^N$ , then estimate  $H(\mathbf{Y})$  using the cross-entropy upper bound on a held-out test set of  $M$  additional measurements:

$$H(\mathbf{Y}) \leq \hat{H}(\mathbf{Y}) = \mathbb{E}[-\log p_\theta(\mathbf{Y})] \quad (4)$$

$$\approx -\frac{1}{M} \sum_{i=1}^M \log p_\theta(\mathbf{y}^{(i)}) \quad (5)$$

This approach has been shown to reliably estimate entropy in complex real-world distributions, even without direct knowledge of the underlying generative process [44].

Furthermore, since this cross-entropy (between the true and estimated distributions) is always larger than the true entropy, this provides a principled way to compare different models: those that achieve lower cross-entropy values produce more accurate estimates. Subtracting our estimate of  $H(\mathbf{Y}|\mathbf{X})$  from this upper bound on  $H(\mathbf{Y})$  yields our estimate of the mutual information  $\hat{I}(\mathbf{X}; \mathbf{Y})$ .

### 3 Implementation and validation

Practically implementing our theoretical framework for information estimation requires choosing an appropriate probabilistic model to fit to the measurement distributions. This choice carries an inherent trade-off between model expressivity and computational efficiency. We explored three model architectures that offer different compromises for this trade-off.

Our models differ in two key assumptions: (1) whether the measurement distribution is constrained to be multivariate Gaussian, which simplifies computation but limits expressivity for non-Gaussian statistics, and (2) whether the model is translation-invariant (stationary), meaning statistical relationships between pixels depend only on their relative positions rather than absolute locations. Stationarity significantly reduces parameter count but cannot capture position-dependent artifacts like fixed sensor defects or illumination gradients.

The three models, in order from least to most expressive, are:

- A **stationary Gaussian process**, which assumes both a Gaussian distribution and translation invariance. It has the fewest parameters (**Fig. S10**), making it useful with limited data, particularly when the underlying statistics are in fact stationary. This model can be fit in 0.1 seconds using  $20 \times 20$  image patches on an NVIDIA RTX A6000 GPU. We developed an optimization procedure to improve its numerical stability and data efficiency (**Fig. S11**) at the cost of longer ( $\sim 10$ s) training times.
- A **Gaussian process** with no constraints on its covariance matrix (i.e. it is non-stationary). This provides greater flexibility while maintaining good computational efficiency ( $\sim 0.1$ s to fit), but still lacks the ability to accurately fit many real-world distributions.
- An autoregressive **PixelCNN** [45–47] model, which can capture complex non-Gaussian measurement distributions, but requires the most data and computation time ( $\sim 100$ s) (**Fig. S17**).

Which model to choose depends on the specific application: the full Gaussian model is fast for large datasets, PixelCNN is the most accurate when data are abundant, and the stationary Gaussian model

can be used when data are scarce. When computational resources allow, the best approach is to train multiple models and select the lowest entropy estimate, since tighter entropy bounds yield better information estimates.

To increase the practicality of fitting models, we processed images as smaller patches of full images. Though larger patches capture more of the statistical relationships between distant pixels in images and can yield more accurate estimates (Fig. S12), smaller patches increase the number of samples for training while also reducing model complexity and computational burden.

We validated the expressiveness and accuracy of our models through a series of experiments using both simulated and real-world data. First, we used simulated measurement data from an analytic model with a known ground truth mutual information: a stationary Gaussian process with additive noise. All three models converged to the correct value if given sufficient data (Fig. S16a). For real-world non-Gaussian data, PixelCNN achieved tighter bounds than Gaussian models (Fig. S16b,c) as demonstrated by its ability to better capture the measurements’ spatial structure (Fig. S14). This advantage is particularly clear on the MNIST dataset of handwritten digits, where pixels tend to be either black or white, creating a bimodal distribution that Gaussian models cannot model well (Fig. S15). Applied to real microscopy data at different photon counts (Fig. S13), our estimators captured the expected increase in information content with improved signal-to-noise ratio across different contrast modalities. Further validation on optical imaging systems limited by photon shot noise (i.e. Poisson-distributed noise) demonstrated that the conditional entropy  $H(Y|X)$  can be estimated accurately using only noisy measurements, except at very low photon counts (Fig. S18).

## 4 Information estimation on imaging applications

Though theoretical results show that mutual information sets a limit on achievable performance for many types of decoders [48–51], real systems deviate from theoretical assumptions and information estimates are imperfect. To further validate our information estimator, we tested its ability to predict the performance of four real imaging systems. These imaging systems use a range of post-processing decoders to obtain the final image, from traditional signal processing approaches to modern neural networks. Typically, system evaluation computes error relative to ground truth data after applying the decoder algorithm to perform tasks like image reconstruction or classification. Our estimator does not require ground truth data and can still predict the performance of the imaging system for various different objects, noise regimes, tasks, and performance metrics, independent of which type of decoder is used. This validates information estimation as a reliable way to evaluate performance without the need for application-specific decoders or ground truth data.

**Color photography** Our first application example involves analyzing color filter arrays for digital photography. Digital cameras capture color images by placing a color filter in front of each pixel, such that it receives only red, green, or blue light; this is the encoding process. Then, post-processing algorithms interpolate this data and reconstruct a full color image with all three colors at each pixel; this is the decoding process, referred to as “demosaicing.” The widely used Bayer pattern arranges filters in a repeating  $2 \times 2$  grid with two green pixels, one red, and one blue (Fig. 2a, bottom). Recent work has suggested that learned designs (encoders) which include “white” pixels (no color filter) can yield higher fidelity reconstructions when combined with modern demosaicing algorithms [52, 53].

We compared three designs: the traditional Bayer pattern, a random arrangement of red, green, blue and white filters as a baseline, and a learned filter created using the method proposed in [53]. Using the Gehler-Shi dataset of natural images [54, 55], we simulated photon shot noise-limited measurements for each filter design and reconstructed full-color images using a neural network decoder for demosaicing [53]. Information content strongly predicted reconstruction quality across all designs; higher mutual information correlated with better image reconstructions. This held true for multiple image quality metrics: mean squared error (MSE), peak signal-to-noise ratio (PSNR), and structural similarity (SSIM) (Fig. S20). This suggests that different filter designs can be compared using information content alone, avoiding the computational burden of the reconstruction algorithm and the need for ground truth data.

**Black hole imaging** Achieving the necessary angular resolution to image a black hole would require a telescope the size of Earth. While building such a telescope is impossible, astronomers can achieve similar resolution by combining data from radio telescopes across the globe, as demonstrated

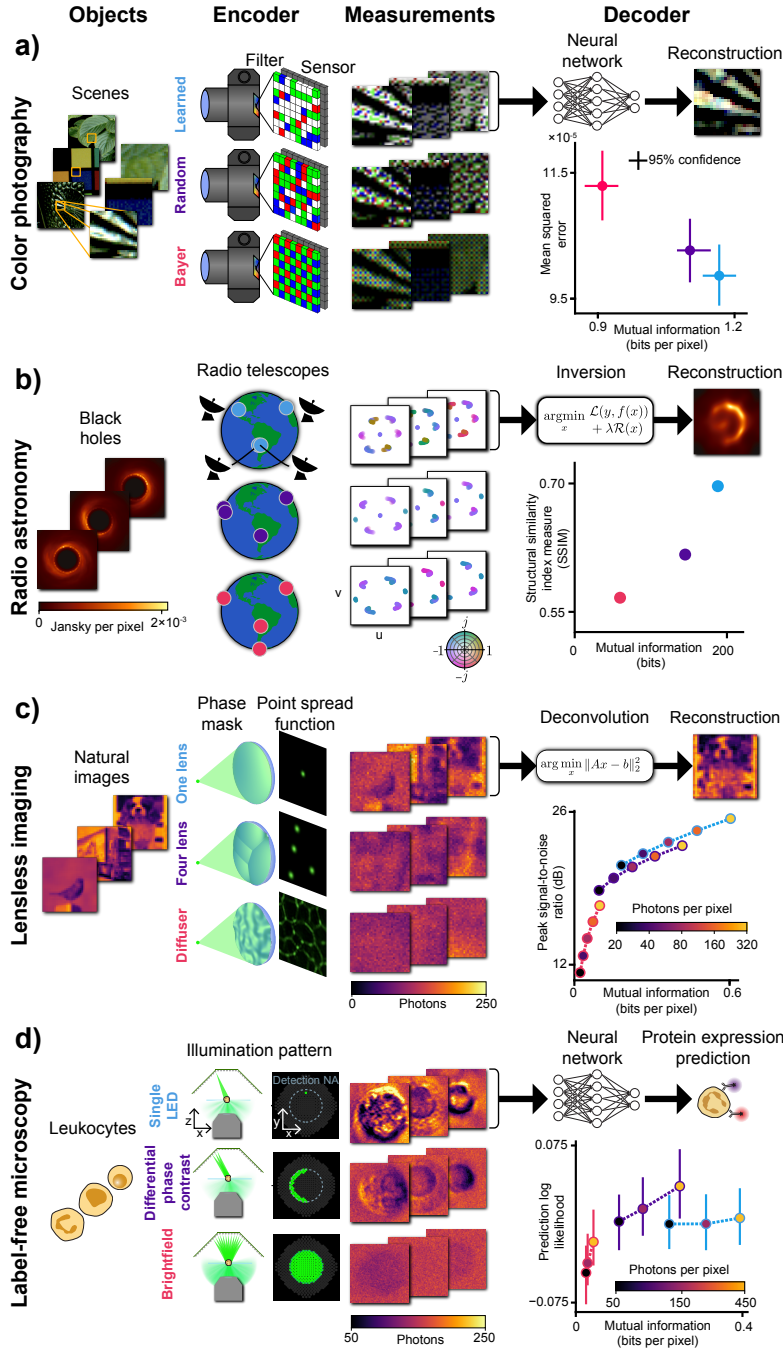


Figure 2: **Four imaging applications demonstrating that our mutual information metric predicts downstream performance of system designs.** **a)** Color filter pattern designs in digital cameras: three example scenes from the object distribution, three different possible encoders and the noisy measurements they produce are shown. We estimated mutual information from the measurements only. We also performed decoding (using a neural network) and calculated mean squared error (MSE) from the ground truth, finding that it correlated with our information estimates. **b)** Potential radio telescope array configurations for black hole imaging. Here, we evaluated three different telescope placements for the Event Horizon Telescope and show that our information estimator predicted the accuracy of recovered black hole structures after decoding by an inverse problem solver. **c)** Optical elements in lensless cameras, evaluated at different signal levels by the error in deconvolved images. **d)** LED array illumination patterns for cellular imaging, tested across multiple illumination intensities and evaluated by accuracy of phenotype predictions. In all these examples, information estimation consistently predicted system performance (Fig. S20), validating its use for evaluating imaging systems without requiring decoders or ground truth data.

by the Event Horizon Telescope’s landmark image of the M87 black hole [56]. The next-generation Event Horizon Telescope aims to go beyond static images to create high-fidelity videos of black holes by adding new radio telescopes at carefully chosen sites around the world [57]. However, determining which telescope sites will produce the best images is challenging. The value of each site depends on its relationship to all others, and while measurements from different configurations can be simulated, performing image reconstructions to evaluate every option is computationally prohibitive. Current approaches therefore rely on simplified metrics that do not account for all features of interest [57].

We tested information estimation on a simplified version of the site selection problem (**Fig. 2b**), selecting combinations of four telescope locations from the original Event Horizon Telescope array. For each configuration, we simulated measurements with additive Gaussian noise and compared our information estimates with quality metrics of the reconstructed image after solving the inverse problem. Measurements with more information consistently produced more accurate reconstructed images of the black hole structure (**Fig. S20**). Information estimation can thus provide an alternative way to evaluate telescope placement that adapts to the data, without requiring complex reconstruction algorithms.

**Lensless imaging** Lensless imagers replace traditional lenses with light-modulating masks, offering compelling advantages: simple hardware, wide field-of-view, and the ability to encode multiple dimensions like depth and time in a single measurement [58]. However, these devices produce encoded measurements that look nothing like the original scene and can vary dramatically between designs, requiring computational reconstruction to recover recognizable images and evaluate performance.

We compared three designs: a traditional lens, a random microlens array [59], and a Gaussian diffuser [60]. Using simulated photon shot noise-limited measurements of natural images at various light levels, we found that information content strongly predicted reconstruction quality across all designs and noise levels (**Fig. 2b**) (**Fig. S20**), demonstrating that information estimation can be used to assess quality without relying on reconstructed images.

**Coded illumination microscopy** LED array microscopy swaps a microscope’s standard lamp with a programmable array of light sources [61, 62]. Images with different types of contrast can be captured by illuminating the sample with LED array patterns that vary the illumination angles, intensity, and spatial coherence. Evaluating these patterns through classical optical theory is challenging because the optimal patterns will depend greatly on the task at hand. Typically, various LED array patterns are compared empirically [63, 64] by evaluating results after the decoding process for a specific task. We choose here the task of predicting protein expression. Using a dataset of white blood cells [65], we compared three illumination patterns: Brightfield, Differential Phase Contrast [66, 67], and Single LED illumination. Measurement contrast correlates to how cellular structures absorb and scatter light, providing label-free measurements of phenotypic features that correlate with protein expression. To study how noise affects system performance, we added simulated photon shot noise to experimental measurements and evaluated both information content and the accuracy of neural networks in predicting the protein level of individual cells.

Mutual information showed a positive correlation with prediction accuracy across all conditions, though single-LED illumination showed higher information content relative to its prediction performance (likely in part due to its sensitivity to optical imperfections inflating information estimates (**Sec. S4.1**)). The ability to predict system performance from information content is particularly significant here because measuring information requires only raw images, while traditional evaluation requires both time-consuming protein labeling experiments to generate ground truth datasets, and decoder training.

#### 4.1 Task-specific information

The microscopy example highlights a key limitation: not all information contributes equally to specific tasks (**Sec. S1.5.2**). While our method estimates total object information in measurements, task-specific applications like classification may only require certain features. Systems that preserve specific task-relevant information can outperform those capturing more total information indiscriminately [23, 68]. This explains why different illumination patterns showed varying correlations between total information and protein prediction accuracy, despite information consistently increasing with signal-to-noise ratio.

We observed this as well in other contexts. For example, in a 10-class object classification task using lensless imaging (**Fig. S22**), different optical designs showed varying classification performance despite similar total information content. While classification accuracy improved with signal-to-noise ratio for each design, the total information measured ( $\sim 100\times$  the amount needed for perfect classification (**Sec. S4.2**)) did not predict performance across designs. Like other global metrics such as image reconstruction error, mutual information may not always directly correlate with information relevant to specialized tasks.

### Information-Driven Encoder Analysis Learning (IDEAL)

Beyond evaluating existing systems, information content can guide the design of new ones. We propose a design framework termed Information-Driven Encoder Analysis Learning (IDEAL), which optimizes imaging systems to maximize the information they capture. IDEAL requires two key components: a differentiable model of the encoder and either a dataset or probabilistic model of the objects being imaged. Because the entropy terms used in our information estimator are also differentiable [69], we can use gradient-based optimization to search for encoder designs that maximize information content (**Fig. 3a**).

We tested IDEAL for designing an improved color filter array for photography (**Fig. 2a**), optimizing the pattern of red, green, blue and white filters to maximize information content. Starting from a random configuration, IDEAL progressively improved the design (**Fig. 3b**). To validate these improvements, we performed two analyses. First, since the optimization objective used the faster but less accurate Gaussian model, we used our most accurate (PixelCNN) estimator to verify that information content increased throughout optimization. Second, we trained image reconstruction algorithms on measurements from different stages of the optimization, finding that the increases in information content corresponded to improvements in reconstruction quality (**Fig. 3c**).

## 5 Discussion

In this work, we developed a practical method for estimating information content in imaging systems using only measurement data and noise characterization. Our approach provides a unified metric that quantifies complex trade-offs between resolution, noise, and other design parameters, as demonstrated across diverse applications from photography to astronomy. Since our estimator requires neither ground truth data nor restrictive assumptions about objects, it can be applied to a wide range of imaging systems. Furthermore, it enables automated, gradient-based optimization of imaging systems designs to maximize information capture.

Our methods address a critical challenge in modern imaging: objectively evaluating systems that rely on computational processing. While algorithms can extract useful information from raw data that is uninterpretable to human observers, evaluating the quality of the measurements is difficult. In the absence of ground truth data, subjective visual assessment of reconstructed images is unreliable, as neural networks can hallucinate convincing but incorrect details [70]. However, ground truth comparisons across multiple experimental systems remain impractical or impossible. By quantifying information content directly from measurements, our approach offers a way to objectively evaluate and compare real-world instruments.

While our approach enables finding optimal data capture methods, it does not solve the separate challenge of decoding measurements into a useful form. High information content indicates potential for excellent performance, but realizing this potential still requires developing appropriate algorithms to extract and interpret the encoded information.

The ability to quantify information may reveal that characteristics of measurements traditionally considered noise actually contain useful signal. Information theory suggests that optimal encoders would produce random-looking measurements to maximize entropy and ensure small object changes remain distinguishable [71, 72]. Such measurements would appear noisy and unintuitive to human observers, who are selectively sensitive to specific visual features [1]. However, it may be possible to extract this signal computationally. For example, laser speckle patterns have traditionally been considered noise and suppressed [32], but more recent work shows they can be effectively interpreted by neural networks [73–75], suggesting that the useful signal they contain is merely unintelligible to human observers.

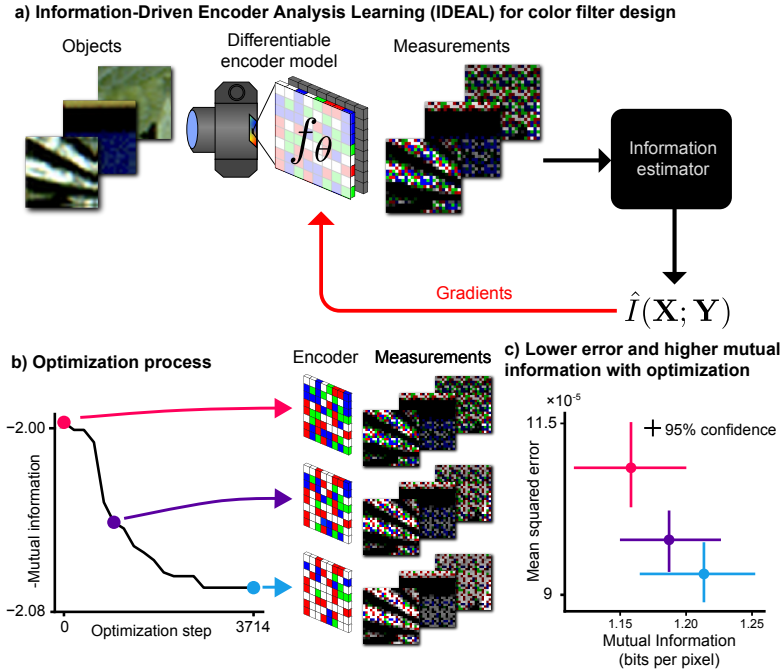


Figure 3: **Information-Driven Encoder Analysis Learning (IDEAL) enables automated design of imaging systems.** **a)** IDEAL combines a differentiable encoder model with our information estimator to optimize system parameters using gradient-based optimization. Here we demonstrate IDEAL on color filter array design for photography using our Gaussian mutual information estimator as an objective. **b)** (Gaussian) information estimates increase over the course of optimization as IDEAL refines the color filter pattern. **c)** Independent validation using the more accurate PixelCNN estimator and reconstruction error confirms that IDEAL’s designs progressively improve both information content and downstream performance.

Future work could advance the accuracy-compute-data Pareto frontier of our estimators. Since our approach reduces to density modeling, it could leverage transformer architectures [76] that exhibit predictable scaling laws [44, 77]. This enables either deploying larger models for more accurate direct estimates or extrapolating the true entropy using scaling relationships on smaller models. Alternatively, specialized architectures might achieve equivalent accuracy with fewer resources. Validating improvements remains straightforward: any model achieving lower cross-entropy on fixed data necessarily tightens the bound on true information content.

Our Information-Driven Encoder Assessment Learning (IDEAL) pipeline shows promising initial results that suggest key computational advantages over existing “end-to-end” optimization methods [78–84]. Unlike end-to-end methods that simultaneously optimize both the imaging system (encoder) and reconstruction algorithm (decoder), IDEAL optimizes only the encoder, allowing decoders to be designed or optimized later. This significantly reduces computation and memory requirements and avoids challenges associated with backpropagating through complex neural network decoders [84, 85], such as vanishing gradients.

IDEAL’s optimization of general information capture, rather than task-specific performance, presents both advantages and limitations. Our experiments show that while general information content correlates with system performance, this relationship weakens for specialized applications that depend on particular object features. Task-specific methods may achieve better performance in these cases, though they typically require specialized training data or specific assumptions about the objects being imaged [23, 68, 86, 85]. When such assumptions or data are unavailable, IDEAL provides a robust default strategy. IDEAL-optimized systems could also serve as effective starting points for task-specific refinement, similar to how machine learning models are pre-trained on large unlabeled datasets before specialized fine-tuning. This hybrid approach would avoid the computational chal-

lenges of full task-specific optimization while still enabling specialized performance with limited additional data.

In summary, our information-based approach offers a versatile tool for evaluating and designing diverse imaging systems. The method's generic probabilistic foundation suggests potential applications beyond imaging, extending to electronic, biological, geological, and chemical sensors.

## **Project website**

<https://waller-lab.github.io/EncodingInformationWebsite/>

## **Code**

<https://github.com/Waller-Lab/EncodingInformation>.

## **Acknowledgements**

For helpful feedback and discussions about this work we thank T. Courtade, E. Aras, K. Lee, K. Bouman, A. Gao, M. Foxxe, C. Degher, S. Degher, D. Degher, S. Baker, J. Goodman, A. Ashok and the UC Berkeley Computational Imaging Lab.

## **Author Contributions**

**Conceptualization:** H.P.

**Methodology:** H.P., L.K., and J.J.

**Data, Experiments and Software:** L.K., H.P., and E.M.

**Funding:** L.W.

**Supervision:** H.P. and L.W.

**Visualization and figures:** H.P., T.C., L.K., E.M., and L.W.

**Writing:** The original draft was written by H.P. with assistance from T.C. and L.K.; all authors contributed to review and editing.

## **Funding**

L.W. is a Chan Zuckerberg Biohub investigator. L.K. was supported by the National Science Foundation Graduate Research Fellowship Program under Grant DGE 2146752.

This work was supported by STROBE: A National Science Foundation Science and Technology Center under Grant No. DMR 1548924, ONR Grant N00014-17-1-2401, and the U.S. Air Force Office Multidisciplinary University Research Initiative (MURI) program under award no. FA9550-23-1-0281.

## References

- [1] David Moshe Fass. *Human sensitivity to mutual information*. Ph.D., Rutgers The State University of New Jersey, School of Graduate Studies, United States – New Jersey, 2006. URL <https://www.proquest.com/docview/305292228/abstract/5B51497B8E7843F2PQ/1?sourcetype=Dissertations%20&%20Theses>. ISBN: 9780542513411.
- [2] Ayush Bhandari, Achuta Kadambi, and Ramesh Raskar. *Computational imaging*. The MIT Press, Cambridge, Massachusetts, 2022. ISBN 978-0-262-04647-3.
- [3] Shaofan Yuan, Chao Ma, Ethan Fetaya, Thomas Mueller, Doron Naveh, Fan Zhang, and Fengnian Xia. Geometric deep optical sensing. *Science*, 379(6637):eade1220, March 2023. doi: 10.1126/science.ade1220. URL <https://www.science.org/doi/10.1126/science.ade1220>. Publisher: American Association for the Advancement of Science.
- [4] Gordon Wetzstein, Aydogan Ozcan, Sylvain Gigan, Shanhui Fan, Dirk Englund, Marin Soljačić, Cornelia Denz, David A.B. Miller, and Demetri Psaltis. Inference in artificial intelligence with deep optics and photonics. *Nature*, 588(7836):39–47, 2020. ISSN 14764687. doi: 10.1038/s41586-020-2973-6.
- [5] P.B. Fellgett and E.H. Linfoot. On the assessment of optical images. *Philosophical Transactions of the Royal Society of London. Series A, Mathematical and Physical Sciences*, 247(931): 369–407, February 1955. ISSN 0080-4614. doi: 10.1098/rsta.1955.0001. URL <https://www.jstor.org/stable/10.2307/j.ctt211qv60.7>. Publisher: Yale University Press.
- [6] G. Toraldo di Francia. Resolving Power and Information. *Journal of the Optical Society of America*, 45(7):497, July 1955. ISSN 0030-3941. doi: 10.1364/JOSA.45.000497. URL <https://www.osapublishing.org/abstract.cfm?URI=josa-46-1-72>.
- [7] G. Toraldo di Francia. Degrees of Freedom of an Image. *Optical Soc America-J*, 59(7): 799–804, 1969.
- [8] Neil J. Bershad. Resolution, Optical-Channel Capacity and Information Theory. *Journal of the Optical Society of America*, 59(2):157, February 1969. ISSN 0030-3941. doi: 10.1364/JOSA.59.000157. URL <https://www.osapublishing.org/abstract.cfm?URI=josa-59-2-157>.
- [9] Carl L. Fales, Friedrich O. Huck, and Richard W. Samms. Imaging system design for improved information capacity. *Applied Optics*, 23(6):872–888, March 1984. ISSN 2155-3165. doi: 10.1364/AO.23.000872. URL <https://opg.optica.org/ao/abstract.cfm?uri=ao-23-6-872>. Publisher: Optica Publishing Group.
- [10] I. J. Cox and C. J. R. Sheppard. Information capacity and resolution in an optical system. *Journal of the Optical Society of America A*, 3(8):1152, August 1986. ISSN 1084-7529. doi: 10.1364/JOSAA.3.001152. URL <https://www.osapublishing.org/abstract.cfm?URI=josaa-3-8-1152>.
- [11] R. Linsker. Self-organization in a perceptual network. *Computer*, 21(3):105–117, March 1988. ISSN 0018-9162. doi: 10.1109/2.36. URL <http://ieeexplore.ieee.org/document/36/>.
- [12] Ralph Linsker. An application of the principle of maximum information preservation to linear systems. In D. Touretzky, editor, *Advances in neural information processing systems*, volume 1. Morgan-Kaufmann, 1988. URL [https://proceedings.neurips.cc/paper\\_files/paper/1988/file/ec8956637a99787bd197eacd77acce5e-Paper.pdf](https://proceedings.neurips.cc/paper_files/paper/1988/file/ec8956637a99787bd197eacd77acce5e-Paper.pdf).
- [13] D. Van Dyck and A.F. de Jong. Ultimate resolution and information in electron microscopy: general principles. *Ultramicroscopy*, 47(1-3):266–281, November 1992. ISSN 03043991. doi: 10.1016/0304-3991(92)90202-U. URL <https://linkinghub.elsevier.com/retrieve/pii/030439919290202U>.

- [14] Friedrich O. Huck, Carl L. Fales, and Zia-ur Rahman. An information theory of visual communication. *Philosophical Transactions of the Royal Society of London. Series A: Mathematical, Physical and Engineering Sciences*, 354(1716):2193–2248, January 1997. doi: 10.1098/rsta.1996.0098. URL <https://royalsocietypublishing.org/doi/abs/10.1098/rsta.1996.0098>. Publisher: Royal Society.
- [15] Mark A. Neifeld. Information, resolution, and space–bandwidth product. *Optics Letters*, 23(18):1477, 1998. ISSN 0146-9592. doi: 10.1364/ol.23.001477.
- [16] J.A. O’Sullivan, R.E. Blahut, and D.L. Snyder. Information-theoretic image formation. *IEEE Transactions on Information Theory*, 44(6):2094–2123, October 1998. ISSN 00189448. doi: 10.1109/18.720533. URL <http://ieeexplore.ieee.org/document/720533/>.
- [17] Rachel Alter-Gartenberg. Information metric as a design tool for optoelectronic imaging systems. *Applied Optics*, 39(11):1743–1760, April 2000. ISSN 2155-3165. doi: 10.1364/AO.39.001743. URL <https://opg.optica.org/ao/abstract.cfm?uri=ao-39-11-1743>. Publisher: Optica Publishing Group.
- [18] Sudhakar Prasad. Information capacity of a seeing-limited imaging system. *Optics Communications*, 177(1):119–134, April 2000. ISSN 0030-4018. doi: 10.1016/S0030-4018(00)00568-X. URL <https://www.sciencedirect.com/science/article/pii/S003040180000568X>.
- [19] Luyin Cao, Stephen E. Reichenbach, and Ram M. Narayanan. Information theoretic assessment and design of hyperspectral imaging systems with nonuniform bandwidths. In Stephen K. Park, Zia-ur Rahman, and Robert A. Schowengerdt, editors, *Aerospace/Defense Sensing, Simulation, and Controls*, pages 72–78, Orlando, FL, August 2001. doi: 10.1117/12.438243. URL <http://proceedings.spiedigitallibrary.org/proceeding.aspx?articleid=914597>.
- [20] Christoph Wagner and Gerd Häusler. Information theoretical optimization for optical range sensors. *Applied Optics*, 42(27):5418, September 2003. ISSN 0003-6935, 1539-4522. doi: 10.1364/AO.42.005418. URL <https://opg.optica.org/abstract.cfm?URI=ao-42-27-5418>.
- [21] Mark A. Neifeld. Information-optimized imaging system design. In Stephen K. Park, Zia-ur Rahman, and Robert A. Schowengerdt, editors, *Aerospace/Defense Sensing, Simulation, and Controls*, pages 113–116, Orlando, FL, August 2001. doi: 10.1117/12.438248. URL <http://proceedings.spiedigitallibrary.org/proceeding.aspx?articleid=914607>.
- [22] Amit Ashok and Mark Neifeld. Information-based analysis of simple incoherent imaging systems. *Optics Express*, 11(18):2153, September 2003. ISSN 1094-4087. doi: 10.1364/OE.11.002153. URL <https://opg.optica.org/oe/abstract.cfm?uri=oe-11-18-2153>.
- [23] Mark A. Neifeld, Amit Ashok, and Pawan K. Baheti. Task-specific information for imaging system analysis. *Journal of the Optical Society of America A*, 24(12):B25, December 2007. ISSN 1084-7529, 1520-8532. doi: 10.1364/JOSAA.24.000B25. URL <https://opg.optica.org/abstract.cfm?URI=josaa-24-12-B25>.
- [24] Yihong Wu and Sergio Verdú. Optimal Phase Transitions in Compressed Sensing, July 2012. URL <http://arxiv.org/abs/1111.6822>. arXiv:1111.6822 [cs, math, stat].
- [25] Amit Ashok, Liang-Chih Huang, and Mark A. Neifeld. Information optimal compressive sensing: static measurement design. *Journal of the Optical Society of America A*, 30(5):831, May 2013. ISSN 1084-7529, 1520-8532. doi: 10.1364/JOSAA.30.000831. URL <https://opg.optica.org/abstract.cfm?URI=josaa-30-5-831>.
- [26] James Huang and Amit Ashok. Information optimal Compressive X-ray Threat Detection. *Imaging and Applied Optics*, 2015.
- [27] Timur E. Gureyev, Alexander Kozlov, Yakov I. Nesterets, David M. Paganin, Andrew V. Martin, and Harry M. Quineya. Signal-to-noise, spatial resolution and information capacity of coherent diffraction imaging. *IUCrJ*, 5:716–726, 2018. ISSN 20522525. doi: 10.1107/S2052252518010941. Publisher: International Union of Crystallography.

- [28] Evgenii Narimanov. Resolution limit of label-free far-field microscopy. *Advanced Photonics*, 1(05):1, 2019. ISSN 2577-5421. doi: 10.1117/1.ap.1.5.056003. arXiv: 1903.05254.
- [29] Florian Willomitzer. *Single-Shot 3D Sensing Close to Physical Limits and Information Limits*. Springer Theses. Springer International Publishing, Cham, 2019. ISBN 978-3-030-10903-5. doi: 10.1007/978-3-030-10904-2. URL <http://link.springer.com/10.1007/978-3-030-10904-2>.
- [30] Amit Ashok, James Huang, Yuzhang Lin, and Ronan Kerviche. Information optimal compressive imaging: design and implementation. In Harrison H. Barrett, John E. Greivenkamp, and Eustace L. Dereniak, editors, *SPIE Optical Engineering + Applications*, page 91860K, San Diego, California, United States, October 2014. doi: 10.1117/12.2063947. URL <http://proceedings.spiedigitallibrary.org/proceeding.aspx?doi=10.1117/12.2063947>.
- [31] Hyun Sung Chang, Yair Weiss, and William T. Freeman. Informative Sensing, January 2009. URL <http://arxiv.org/abs/0901.4275>. arXiv:0901.4275 [cs, math].
- [32] Joseph W. Goodman. *Statistical optics*. Wiley series in pure and applied optics. John Wiley & Sons Inc, Hoboken, New Jersey, second edition edition, 2015. ISBN 978-1-119-00945-0.
- [33] Alexander Kraskov, Harald Stögbauer, and Peter Grassberger. Estimating mutual information. *Physical Review E*, 69(6):066138, June 2004. doi: 10.1103/PhysRevE.69.066138. URL <https://link.aps.org/doi/10.1103/PhysRevE.69.066138>. Publisher: American Physical Society.
- [34] Georges A. Darbellay and Igor Vajda. Estimation of the information by an adaptive partitioning of the observation space. *IEEE Transactions on Information Theory*, 45(4):1315–1321, 1999. ISSN 00189448. doi: 10.1109/18.761290.
- [35] Brian C. Ross. Mutual information between discrete and continuous data sets. *PLoS ONE*, 9(2), 2014. ISSN 19326203. doi: 10.1371/journal.pone.0087357.
- [36] Ben Poole, Sherjil Ozair, Aaron van den Oord, Alexander A. Alemi, and George Tucker. On Variational Bounds of Mutual Information, May 2019. URL <http://arxiv.org/abs/1905.06922>. arXiv:1905.06922 [cs, stat].
- [37] Ziv Goldfeld and Kristjan Greenewald. Sliced mutual information: a scalable measure of statistical dependence. In A. Beygelzimer, Y. Dauphin, P. Liang, and J. Wortman Vaughan, editors, *Advances in neural information processing systems*, 2021. URL <https://openreview.net/forum?id=SvrYl-FDq2>.
- [38] Jiaming Song and Stefano Ermon. Understanding the limitations of variational mutual information estimators. In *International conference on learning representations*, 2020. URL <https://openreview.net/forum?id=B1x62TNtDS>.
- [39] Pawel Czyz, Frederic Grabowski, Julia E Vogt, Niko Beerenwinkel, and Alexander Marx. Beyond normal: On the evaluation of mutual information estimators. In *Thirty-seventh conference on neural information processing systems*, 2023. URL <https://openreview.net/forum?id=25vRtG56YH>.
- [40] Gokul Gowri, Xiao-Kang Lun, Allon M. Klein, and Peng Yin. Approximating mutual information of high-dimensional variables using learned representations. In A. Globerson, L. Mackey, D. Belgrave, A. Fan, U. Paquet, J. Tomczak, and C. Zhang, editors, *Advances in neural information processing systems*, volume 37, pages 132843–132875. Curran Associates, Inc., 2024. URL [https://proceedings.neurips.cc/paper\\_files/paper/2024/file/efa9e3ed9c411aeb53d7bfe38a19d884-Paper-Conference.pdf](https://proceedings.neurips.cc/paper_files/paper/2024/file/efa9e3ed9c411aeb53d7bfe38a19d884-Paper-Conference.pdf).
- [41] Nunzio A. Letizia, Nicola Novello, and Andrea M. Tonello. Mutual information estimation via f-Divergence and data derangements. In A. Globerson, L. Mackey, D. Belgrave, A. Fan, U. Paquet, J. Tomczak, and C. Zhang, editors, *Advances in neural information processing systems*, volume 37, pages 105114–105150. Curran Associates, Inc., 2024. URL [https://proceedings.neurips.cc/paper\\_files/paper/2024/file/bdcfa850adac4a1088153881282ca972-Paper-Conference.pdf](https://proceedings.neurips.cc/paper_files/paper/2024/file/bdcfa850adac4a1088153881282ca972-Paper-Conference.pdf).

- [42] Butakov I. D., Tolmachev A. D., Malanchuk S. V., Neopryatnaya A. M., and Frolov A. A. Mutual information estimation via normalizing flows. In A. Globerson, L. Mackey, D. Belgrave, A. Fan, U. Paquet, J. Tomczak, and C. Zhang, editors, *Advances in neural information processing systems*, volume 37, pages 3027–3057. Curran Associates, Inc., 2024. URL [https://proceedings.neurips.cc/paper\\_files/paper/2024/file/05a2d9ef0ae6f249737c1e4cce724a0c-Paper-Conference.pdf](https://proceedings.neurips.cc/paper_files/paper/2024/file/05a2d9ef0ae6f249737c1e4cce724a0c-Paper-Conference.pdf).
- [43] David McAllester and Karl Stratos. Formal limitations on the measurement of mutual information. In Silvia Chiappa and Roberto Calandra, editors, *Proceedings of the twenty third international conference on artificial intelligence and statistics*, volume 108 of *Proceedings of machine learning research*, pages 875–884. PMLR, August 2020. URL <https://proceedings.mlr.press/v108/mcallester20a.html>.
- [44] Tom Henighan, Jared Kaplan, Mor Katz, Mark Chen, Christopher Hesse, Jacob Jackson, Heewoo Jun, Tom B. Brown, Prafulla Dhariwal, Scott Gray, Chris Hallacy, Benjamin Mann, Alec Radford, Aditya Ramesh, Nick Ryder, Daniel M. Ziegler, John Schulman, Dario Amodei, and Sam McCandlish. Scaling Laws for Autoregressive Generative Modeling, October 2020. URL <http://arxiv.org/abs/2010.14701>. arXiv: 2010.14701.
- [45] Aaron van den Oord, Nal Kalchbrenner, and Koray Kavukcuoglu. Pixel Recurrent Neural Networks, 2016. URL <http://arxiv.org/abs/1601.06759>. arXiv: 1601.06759 ISBN: 9781510829008.
- [46] Aäron van den Oord, Nal Kalchbrenner, Oriol Vinyals, Lasse Espeholt, Alex Graves, and Koray Kavukcuoglu. Conditional Image Generation with PixelCNN Decoders. *arXiv*, pages 4790–4798, 2016. ISSN 10495258. URL <https://papers.nips.cc/paper/6527-conditional-image-generation-with-pixelcnn-decoders>. arXiv: 1606.05328 ISBN: 9781510829008.
- [47] Tim Salimans, Andrej Karpathy, Xi Chen, and Diederik P Kingma. Pixel CNN++: Improving the Pixel CNN With Discretized Logistic Mixture Likelihood. *Iclr*, pages 1–10, 2017. URL <https://openreview.net/forum?id=BJrFC6ceg%0Ahttps://arxiv.org/abs/1701.05517>. arXiv: 1701.05517.
- [48] Eric Clarkson and Johnathan B. Cushing. Shannon information and receiver operating characteristic analysis for multiclass classification in imaging. *Journal of the Optical Society of America A*, 33(5):930, May 2016. ISSN 1084-7529, 1520-8532. doi: 10.1364/JOSAA.33.000930. URL <https://opg.optica.org/abstract.cfm?URI=josaa-33-5-930>.
- [49] Eric Clarkson and Johnathan B. Cushing. Shannon information and ROC analysis in imaging. *Journal of the Optical Society of America A*, 32(7):1288, July 2015. ISSN 1084-7529, 1520-8532. doi: 10.1364/JOSAA.32.001288. URL <https://opg.optica.org/abstract.cfm?URI=josaa-32-7-1288>.
- [50] D. Guo, S. Shamai, and S. Verdu. Mutual Information and Minimum Mean-Square Error in Gaussian Channels. *IEEE Transactions on Information Theory*, 51(4):1261–1282, April 2005. ISSN 0018-9448. doi: 10.1109/TIT.2005.844072. URL <http://ieeexplore.ieee.org/document/1412024/>.
- [51] Dongning Guo, Shlomo Shamai, and Sergio Verdu. Mutual Information and Conditional Mean Estimation in Poisson Channels. *IEEE Transactions on Information Theory*, 54(5): 1837–1849, May 2008. ISSN 0018-9448, 1557-9654. doi: 10.1109/TIT.2008.920206. URL <http://ieeexplore.ieee.org/document/4494688/>.
- [52] Bernardo Henz, Eduardo S. L. Gastal, and Manuel M. Oliveira. Deep Joint Design of Color Filter Arrays and Demosaicing. *Computer Graphics Forum*, 37(2):389–399, May 2018. ISSN 0167-7055, 1467-8659. doi: 10.1111/cgf.13370. URL <https://onlinelibrary.wiley.com/doi/10.1111/cgf.13370>.
- [53] Ayan Chakrabarti. Learning Sensor Multiplexing Design through Back-propagation. In *Advances in Neural Information Processing Systems 29 (NeurIPS 2016)*, 2016.

- [54] Peter Vincent Gehler, Carsten Rother, Andrew Blake, Tom Minka, and Toby Sharp. Bayesian color constancy revisited. In *2008 IEEE Conference on Computer Vision and Pattern Recognition*, pages 1–8, Anchorage, AK, USA, June 2008. IEEE. ISBN 978-1-4244-2242-5. doi: 10.1109/CVPR.2008.4587765. URL <http://ieeexplore.ieee.org/document/4587765/>.
- [55] Lilong Shi and Brian Funt. Re-processed Version of the Gehler Color Constancy Dataset of 568 Images, 2012. URL <http://www.cs.sfu.ca/~colour/data/>.
- [56] The Event Horizon Telescope Collaboration, Kazunori Akiyama, Antxon Alberdi, Walter Alef, Keiichi Asada, Rebecca Azulay, Anne-Kathrin Baczko, David Ball, Mislav Baloković, John Barrett, Dan Bintley, Lindy Blackburn, Wilfred Boland, Katherine L. Bouman, Geoffrey C. Bower, Michael Bremer, Christiaan D. Brinkerink, Roger Brissenden, Silke Britzen, Avery E. Broderick, Dominique Brogiere, Thomas Bronzwaer, Do-Young Byun, John E. Carlstrom, Andrew Chael, Chi-kwan Chan, Shami Chatterjee, Koushik Chatterjee, Ming-Tang Chen, Yongjun Chen, Ilje Cho, Pierre Christian, John E. Conway, James M. Cordes, Geoffrey B. Crew, Yuzhu Cui, Jordy Davelaar, Mariafelicia De Laurentis, Roger Deane, Jessica Dempsey, Gregory Desvignes, Jason Dexter, Sheperd S. Doeleman, Ralph P. Eatough, Heino Falcke, Vincent L. Fish, Ed Fomalont, Raquel Fraga-Encinas, William T. Freeman, Per Friberg, Christian M. Fromm, José L. Gómez, Peter Galison, Charles F. Gammie, Roberto García, Olivier Gentaz, Boris Georgiev, Ciriaco Goddi, Roman Gold, Minfeng Gu, Mark Gurwell, Kazuhiro Hada, Michael H. Hecht, Ronald Hesper, Luis C. Ho, Paul Ho, Mareki Honma, Chih-Wei L. Huang, Lei Huang, David H. Hughes, Shiro Ikeda, Makoto Inoue, Sara Issaoun, David J. James, Buell T. Jannuzi, Michael Janssen, Britton Jeter, Wu Jiang, Michael D. Johnson, Svetlana Jorstad, Taehyun Jung, Mansour Karami, Ramesh Karuppusamy, Tomohisa Kawashima, Garrett K. Keating, Mark Kettenis, Jae-Young Kim, Junhan Kim, Jongsoo Kim, Motoki Kino, Jun Yi Koay, Patrick M. Koch, Shoko Koyama, Michael Kramer, Carsten Kramer, Thomas P. Krichbaum, Cheng-Yu Kuo, Tod R. Lauer, Sang-Sung Lee, Yan-Rong Li, Zhiyuan Li, Michael Lindqvist, Kuo Liu, Elisabetta Liuzzo, Wen-Ping Lo, Andrei P. Lobanov, Laurent Loinard, Colin Lonsdale, Ru-Sen Lu, Nicholas R. MacDonald, Jirong Mao, Sera Markoff, Daniel P. Marrone, Alan P. Marscher, Iván Martí-Vidal, Satoki Matsushita, Lynn D. Matthews, Lia Medeiros, Karl M. Menten, Yosuke Mizuno, Izumi Mizuno, James M. Moran, Kotaro Moriyama, Monika Moscibrodzka, Cornelia Müller, Hiroshi Nagai, Neil M. Nagar, Masanori Nakamura, Ramesh Narayan, Gopal Narayanan, Iniyan Natarajan, Roberto Neri, Chunghong Ni, Aristeidis Noutsos, Hiroki Okino, Héctor Olivares, Tomoaki Oyama, Feryal Özel, Daniel C. M. Palumbo, Nimesh Patel, Ue-Li Pen, Dominic W. Pesce, Vincent Piétu, Richard Plambeck, Aleksandar PopStefanija, Oliver Porth, Ben Prather, Jorge A. Preciado-López, Dimitrios Psaltis, Hung-Yi Pu, Venkatesh Ramakrishnan, Ramprasad Rao, Mark G. Rawlings, Alexander W. Raymond, Luciano Rezzolla, Bart Ripperda, Freek Roelofs, Alan Rogers, Eduardo Ros, Mel Rose, Arash Roshaninshat, Helge Rottmann, Alan L. Roy, Chet Ruszczyk, Benjamin R. Ryan, Kazi L. J. Rygl, Salvador Sánchez, David Sánchez-Arguelles, Mahito Sasada, Tuomas Savolainen, F. Peter Schloerb, Karl-Friedrich Schuster, Lijing Shao, Zhiqiang Shen, Des Small, Bong Won Sohn, Jason SooHoo, Fumie Tazaki, Paul Tiede, Remo P. J. Tilanus, Michael Titus, Kenji Toma, Pablo Torne, Tyler Trent, Sascha Trippe, Shuichiro Tsuda, Ilse Van Bemmelen, Huib Jan Van Langevelde, Daniel R. Van Rossum, Jan Wagner, John Wardle, Jonathan Weintroub, Norbert Wex, Robert Wharton, Maciek Wielgus, George N. Wong, Qingwen Wu, André Young, Ken Young, Ziri Younsi, Feng Yuan, Ye-Fei Yuan, J. Anton Zensus, Guangyao Zhao, Shan-Shan Zhao, Ziyang Zhu, Joseph R. Farah, Zheng Meyer-Zhao, Daniel Michalik, Andrew Nadolski, Hiroaki Nishioka, Nicolas Pradel, Rurik A. Primiani, Kamal Souccar, Laura Vertatschitsch, and Paul Yamaguchi. First M87 Event Horizon Telescope Results. IV. Imaging the Central Supermassive Black Hole. *The Astrophysical Journal Letters*, 875(1):L4, April 2019. ISSN 2041-8205, 2041-8213. doi: 10.3847/2041-8213/ab0e85. URL <https://iopscience.iop.org/article/10.3847/2041-8213/ab0e85>.
- [57] Sheperd S. Doeleman, John Barrett, Lindy Blackburn, Katherine L. Bouman, Avery E. Broderick, Ryan Chaves, Vincent L. Fish, Garret Fitzpatrick, Mark Freeman, Antonio Fuentes, José L. Gómez, Kari Haworth, Janice Houston, Sara Issaoun, Michael D. Johnson, Mark Kettenis, Laurent Loinard, Neil Nagar, Gopal Narayanan, Aaron Oppenheimer, Daniel C. M. Palumbo, Nimesh Patel, Dominic W. Pesce, Alexander W. Raymond, Freek Roelofs, Ranjani Srinivasan, Paul Tiede, Jonathan Weintroub, and Maciek Wielgus. Reference Array and Design Consideration for the Next-Generation Event Horizon Telescope. *Galax-*

- ies, 11(5):107, October 2023. ISSN 2075-4434. doi: 10.3390/galaxies11050107. URL <https://www.mdpi.com/2075-4434/11/5/107>.
- [58] Vivek Boominathan, Jacob T. Robinson, Laura Waller, and Ashok Veeraraghavan. Recent advances in lensless imaging. *Optica*, 9(1):1–16, January 2022. ISSN 2334-2536. doi: 10.1364/OPTICA.431361. URL <https://opg.optica.org/optica/abstract.cfm?uri=optica-9-1-1>. Publisher: Optica Publishing Group.
- [59] Leyla Kabuli, Gina Wu, and Laura Waller. High-Quality Lensless Imaging with a Random Multi-Focal Lenslet Phase Mask. In *Optica Imaging Congress (3D, COSI, DH, FLatOptics, IS, pcAOP)*, page CW3B.2, Boston, Massachusetts, 2023. Optica Publishing Group. ISBN 978-1-957171-28-9. doi: 10.1364/COSI.2023.CW3B.2. URL <https://opg.optica.org/abstract.cfm?URI=COSI-2023-CW3B.2>.
- [60] Nick Antipa, Grace Kuo, Reinhard Heckel, Ben Mildenhall, Emrah Bostan, Ren Ng, and Laura Waller. DiffuserCam: lensless single-exposure 3D imaging. *Optica*, 5(1):1, January 2018. ISSN 2334-2536. doi: 10.1364/OPTICA.5.000001. URL <https://opg.optica.org/abstract.cfm?URI=optica-5-1-1>.
- [61] Guoan Zheng, Christopher Kolner, and Changhuei Yang. Microscopy refocusing and dark-field imaging by using a simple LED array. *Optics Letters*, 36(20):3987, 2011. ISSN 0146-9592. doi: 10.1364/OL.36.003987. URL <https://www.osapublishing.org/abstract.cfm?URI=ol-36-20-3987>. ISBN: 0090-8258 (Print)\r0090-8258 (Linking).
- [62] Zachary F. Phillips, Regina Eckert, and Laura Waller. Quasi-Dome: A Self-Calibrated High-NA LED Illuminator for Fourier Ptychography. In *Imaging and Applied Optics 2017 (3D, AIO, COSI, IS, MATH, pcAOP)*, volume IW4E.5, 2017. doi: 10.1364/isa.2017.iw4e.5.
- [63] Michael R. Kellman, Emrah Bostan, Nicole A. Repina, and Laura Waller. Physics-Based Learned Design: Optimized Coded-Illumination for Quantitative Phase Imaging. *IEEE Transactions on Computational Imaging*, 5(3):344–353, 2019. ISSN 2573-0436. doi: 10.1109/tci.2019.2905434. arXiv: 1808.03571.
- [64] Roarke Horstmeyer, Richard Y. Chen, Barbara Kappes, and Benjamin Judkewitz. Convolutional neural networks that teach microscopes how to image. *arXiv*, September 2017. URL <http://arxiv.org/abs/1709.07223>. arXiv: 1709.07223.
- [65] Henry Pinkard, Cherry Liu, Fanice Nyatigo, Daniel A. Fletcher, and Laura Waller. The Berkeley Single Cell Computational Microscopy (BSCCM) Dataset, February 2024. URL <http://arxiv.org/abs/2402.06191>. arXiv:2402.06191 [cs, q-bio].
- [66] Shalin B Mehta and Colin J R Sheppard. Quantitative phase-gradient imaging at high resolution with asymmetric illumination-based differential phase contrast. *Optics Letters*, 34(13):1924, 2009. ISSN 0146-9592. doi: 10.1364/ol.34.001924. ISBN: 0146-9592.
- [67] Lei Tian and Laura Waller. Quantitative differential phase contrast imaging in an LED array microscope. *Optics Express*, 23(9):11394, 2015. ISSN 1094-4087. doi: 10.1364/OE.23.011394. URL <https://www.osapublishing.org/oe/abstract.cfm?uri=oe-23-9-11394>.
- [68] Amit Ashok, Pawan K. Baheti, and Mark A. Neifeld. Compressive imaging system design using task-specific information. *Applied Optics*, 47(25):4457, September 2008. ISSN 0003-6935, 1539-4522. doi: 10.1364/AO.47.004457. URL <https://opg.optica.org/abstract.cfm?URI=ao-47-25-4457>.
- [69] David J C MacKay. *Information Theory, Inference, and Learning Algorithms David J.C. MacKay*. Cambridge University Press, 2003. ISBN 978-0-521-64298-9. doi: 10.5555/971143. ISSN: 01621459.
- [70] Ziwei Ji, Nayeon Lee, Rita Frieske, Tiezheng Yu, Dan Su, Yan Xu, Etsuko Ishii, Yejin Bang, Delong Chen, Wenliang Dai, Ho Shu Chan, Andrea Madotto, and Pascale Fung. Survey of Hallucination in Natural Language Generation. *ACM Computing Surveys*, 55(12):1–38, December 2023. ISSN 0360-0300, 1557-7341. doi: 10.1145/3571730. URL <http://arxiv.org/abs/2202.03629>. arXiv:2202.03629 [cs].

- [71] Claude E Shannon. A mathematical theory of communication. *The Bell System Technical Journal*, 5(1):3, January 1948. ISSN 15591662. doi: 10.1145/584091.584093. URL <http://portal.acm.org/citation.cfm?doid=584091.584093>. arXiv: [chaodyn/9411012](https://arxiv.org/abs/chaodyn/9411012) ISBN: 0252725484.
- [72] Thomas M Cover and Joy A. Thomas. *Elements of Information Theory*. Wiley, New York, USA, September 2005. ISBN 978-0-471-24195-9. doi: 10.1002/047174882X. URL <http://doi.wiley.com/10.1002/0471200611>. Series Title: Wiley Series in Telecommunications.
- [73] Hengameh Mirzaalian, Mohamed Hussein, and Wael Abd-Almageed. On the Effectiveness of Laser Speckle Contrast Imaging and Deep Neural Networks for Detecting Known and Unknown Fingerprint Presentation Attacks. In *2019 International Conference on Biometrics (ICB)*, pages 1–8, Crete, Greece, June 2019. IEEE. ISBN 978-1-72813-640-0. doi: 10.1109/ICB45273.2019.8987428. URL <https://ieeexplore.ieee.org/document/8987428/>.
- [74] Yunzhe Li, Yujia Xue, and Lei Tian. Deep speckle correlation: a deep learning approach toward scalable imaging through scattering media. *Optica*, 5(10):1181, October 2018. ISSN 2334-2536. doi: 10.1364/OPTICA.5.001181. URL <https://opg.optica.org/abstract.cfm?URI=optica-5-10-1181>.
- [75] Ulas Kürüm, Peter R. Wiecha, Rebecca French, and Otto L. Muskens. Deep learning enabled real time speckle recognition and hyperspectral imaging using a multimode fiber array. *Optics Express*, 27(15):20965–20979, July 2019. ISSN 1094-4087. doi: 10.1364/OE.27.020965. URL <https://opg.optica.org/oe/abstract.cfm?uri=oe-27-15-20965>. Publisher: Optica Publishing Group.
- [76] Ashish Vaswani, Noam Shazeer, Niki Parmar, Jakob Uszkoreit, Llion Jones, Aidan N Gomez, Łukasz Kaiser, and Illia Polosukhin. Attention is all you need. In I. Guyon, U. Von Luxburg, S. Bengio, H. Wallach, R. Fergus, S. Vishwanathan, and R. Garnett, editors, *Advances in neural information processing systems*, volume 30. Curran Associates, Inc., 2017. URL [https://proceedings.neurips.cc/paper\\_files/paper/2017/file/3f5ee243547dee91fbd053c1c4a845aa-Paper.pdf](https://proceedings.neurips.cc/paper_files/paper/2017/file/3f5ee243547dee91fbd053c1c4a845aa-Paper.pdf).
- [77] OpenAI, Josh Achiam, Steven Adler, Sandhini Agarwal, Lama Ahmad, Ilge Akkaya, Florencia Leoni Aleman, Diogo Almeida, Janko Altmenschmidt, Sam Altman, Shyamal Anadkat, Red Avila, Igor Babuschkin, Suchir Balaji, Valerie Balcom, Paul Baltescu, Haiming Bao, Mohammad Bavarian, Jeff Belgum, Irwan Bello, Jake Berdine, Gabriel Bernadett-Shapiro, Christopher Berner, Lenny Bogdonoff, Oleg Boiko, Madelaine Boyd, Anna-Luisa Brakman, Greg Brockman, Tim Brooks, Miles Brundage, Kevin Button, Trevor Cai, Rosie Campbell, Andrew Cann, Brittany Carey, Chelsea Carlson, Rory Carmichael, Brooke Chan, Che Chang, Fotis Chantzis, Derek Chen, Sully Chen, Ruby Chen, Jason Chen, Mark Chen, Ben Chess, Chester Cho, Casey Chu, Hyung Won Chung, Dave Cummings, Jeremiah Currier, Yunxing Dai, Cory Decareaux, Thomas Degry, Noah Deutsch, Damien Deville, Arka Dhar, David Dohan, Steve Dowling, Sheila Dunning, Adrien Ecoffet, Atty Eleti, Tyna Eloundou, David Farhi, Liam Fedus, Niko Felix, Simón Posada Fishman, Juston Forte, Isabella Fulford, Leo Gao, Elie Georges, Christian Gibson, Vik Goel, Tarun Gogineni, Gabriel Goh, Rapha Gontijo-Lopes, Jonathan Gordon, Morgan Grafstein, Scott Gray, Ryan Greene, Joshua Gross, Shixiang Shane Gu, Yufei Guo, Chris Hallacy, Jesse Han, Jeff Harris, Yuchen He, Mike Heaton, Johannes Heidecke, Chris Hesse, Alan Hickey, Wade Hickey, Peter Hoeschele, Brandon Houghton, Kenny Hsu, Shengli Hu, Xin Hu, Joost Huizinga, Shantanu Jain, Shawn Jain, Joanne Jang, Angela Jiang, Roger Jiang, Haozhun Jin, Denny Jin, Shino Jomoto, Billie Jonn, Heewoo Jun, Tomer Kaftan, Łukasz Kaiser, Ali Kamali, Ingmar Kanitscheider, Nitish Shirish Keskar, Tabarak Khan, Logan Kilpatrick, Jong Wook Kim, Christina Kim, Yongjik Kim, Jan Hendrik Kirchner, Jamie Kiros, Matt Knight, Daniel Kokotajlo, Łukasz Kondraciuk, Andrew Kondrich, Aris Konstantinidis, Kyle Kopic, Gretchen Krueger, Vishal Kuo, Michael Lampe, Ikai Lan, Teddy Lee, Jan Leike, Jade Leung, Daniel Levy, Chak Ming Li, Rachel Lim, Molly Lin, Stephanie Lin, Mateusz Litwin, Theresa Lopez, Ryan Lowe, Patricia Lue, Anna Makanju, Kim Malfacini, Sam Manning, Todor Markov, Yaniv Markovski, Bianca Martin, Katie Mayer, Andrew Mayne, Bob McGrew, Scott Mayer McKinney, Christine McLeavey, Paul McMillan, Jake McNeil, David Medina, Aalok Mehta, Jacob Menick, Luke Metz, Andrey Mishchenko, Pamela Mishkin, Vinnie Monaco, Evan Morikawa, Daniel Mossing, Tong Mu, Mira Murati,

- Oleg Murk, David Mély, Ashvin Nair, Reiichiro Nakano, Rajeev Nayak, Arvind Neelakantan, Richard Ngo, Hyeonwoo Noh, Long Ouyang, Cullen O’Keefe, Jakub Pachocki, Alex Paino, Joe Palermo, Ashley Pantuliano, Giambattista Parascandolo, Joel Parish, Emy Parparita, Alex Passos, Mikhail Pavlov, Andrew Peng, Adam Perelman, Filipe de Avila Belbute Peres, Michael Petrov, Henrique Ponde de Oliveira Pinto, Michael, Pokorny, Michelle Pokrass, Vitchyr H. Pong, Tolly Powell, Alethea Power, Boris Power, Elizabeth Proehl, Raul Puri, Alec Radford, Jack Rae, Aditya Ramesh, Cameron Raymond, Francis Real, Kendra Rimbach, Carl Ross, Bob Rotsted, Henri Roussez, Nick Ryder, Mario Saltarelli, Ted Sanders, Shibani Santurkar, Girish Sastry, Heather Schmidt, David Schnurr, John Schulman, Daniel Selsam, Kyla Sheppard, Toki Sherbakov, Jessica Shieh, Sarah Shoker, Pranav Shyam, Szymon Sidor, Eric Sigler, Maddie Simens, Jordan Sitkin, Katarina Slama, Ian Sohl, Benjamin Sokolowsky, Yang Song, Natalie Staudacher, Felipe Petroski Such, Natalie Summers, Ilya Sutskever, Jie Tang, Nikolas Tezak, Madeleine B. Thompson, Phil Tillet, Amin Tootoonchian, Elizabeth Tseng, Preston Tuggle, Nick Turley, Jerry Tworek, Juan Felipe Cerón Uribe, Andrea Vallone, Arun Vijayvergiya, Chelsea Voss, Carroll Wainwright, Justin Jay Wang, Alvin Wang, Ben Wang, Jonathan Ward, Jason Wei, C. J. Weinmann, Akila Welihinda, Peter Welinder, Jiayi Weng, Lilian Weng, Matt Wiethoff, Dave Willner, Clemens Winter, Samuel Wolrich, Hannah Wong, Lauren Workman, Sherwin Wu, Jeff Wu, Michael Wu, Kai Xiao, Tao Xu, Sarah Yoo, Kevin Yu, Qiming Yuan, Wojciech Zaremba, Rowan Zellers, Chong Zhang, Marvin Zhang, Shengjia Zhao, Tianhao Zheng, Juntang Zhuang, William Zhuk, and Barret Zoph. GPT-4 Technical Report, March 2024. URL <http://arxiv.org/abs/2303.08774>. arXiv:2303.08774 [cs].
- [78] Vincent Sitzmann, Steven Diamond, Yifan Peng, Xiong Dun, Stephen Boyd, Wolfgang Heidrich, Felix Heide, and Gordon Wetzstein. End-to-end optimization of optics and image processing for achromatic extended depth of field and super-resolution imaging. *ACM Transactions on Graphics*, 37(4):1–13, August 2018. ISSN 0730-0301, 1557-7368. doi: 10.1145/3197517.3201333. URL <https://dl.acm.org/doi/10.1145/3197517.3201333>.
- [79] Qilin Sun, Ethan Tseng, Qiang Fu, Wolfgang Heidrich, and Felix Heide. Learning Rank-1 Diffractive Optics for Single-Shot High Dynamic Range Imaging. In *2020 IEEE/CVF Conference on Computer Vision and Pattern Recognition (CVPR)*, pages 1383–1393, Seattle, WA, USA, June 2020. IEEE. ISBN 978-1-72817-168-5. doi: 10.1109/CVPR42600.2020.00146. URL <https://ieeexplore.ieee.org/document/9157825/>.
- [80] Christopher A. Metzler, Hayato Ikoma, Yifan Peng, and Gordon Wetzstein. Deep Optics for Single-Shot High-Dynamic-Range Imaging. In *2020 IEEE/CVF Conference on Computer Vision and Pattern Recognition (CVPR)*, pages 1372–1382, Seattle, WA, USA, June 2020. IEEE. ISBN 978-1-72817-168-5. doi: 10.1109/CVPR42600.2020.00145. URL <https://ieeexplore.ieee.org/document/9156877/>.
- [81] Qilin Sun, Congli Wang, Qiang Fu, Xiong Dun, and Wolfgang Heidrich. End-to-end complex lens design with differentiate ray tracing. *ACM Transactions on Graphics*, 40(4):1–13, August 2021. ISSN 0730-0301, 1557-7368. doi: 10.1145/3450626.3459674. URL <https://dl.acm.org/doi/10.1145/3450626.3459674>.
- [82] Ethan Tseng, Shane Colburn, James Whitehead, Luocheng Huang, Seung-Hwan Baek, Arka Majumdar, and Felix Heide. Neural nano-optics for high-quality thin lens imaging. *Nature Communications*, 12(1):6493, November 2021. ISSN 2041-1723. doi: 10.1038/s41467-021-26443-0. URL <https://www.nature.com/articles/s41467-021-26443-0>.
- [83] Ethan Tseng, Ali Mosleh, Fahim Mannan, Karl St-Arnaud, Avinash Sharma, Yifan Peng, Alexander Braun, Derek Nowrouzezahrai, Jean-François Lalonde, and Felix Heide. Differentiable Compound Optics and Processing Pipeline Optimization for End-to-end Camera Design. *ACM Transactions on Graphics*, 40(2):1–19, April 2021. ISSN 0730-0301, 1557-7368. doi: 10.1145/3446791. URL <https://dl.acm.org/doi/10.1145/3446791>.
- [84] Diptodip Deb, Zhenfei Jiao, Ruth Sims, Alex B. Chen, Michael Broxton, Misha B. Ahrens, Kaspar Podgorski, and Srinivas C. Turaga. FourierNets enable the design of highly non-local optical encoders for computational imaging, November 2022. URL <http://arxiv.org/abs/2104.10611>. arXiv:2104.10611 [cs, eess].

- [85] Xinge Yang, Qiang Fu, Yunfeng Nie, and Wolfgang Heidrich. Image Quality Is Not All You Want: Task-Driven Lens Design for Image Classification, May 2023. URL <http://arxiv.org/abs/2305.17185>. arXiv:2305.17185 [physics].
- [86] Jerry Chao, E. Sally Ward, and Raimund J. Ober. Fisher information theory for parameter estimation in single molecule microscopy: tutorial. *JOSA A*, 33(7):B36–B57, July 2016. ISSN 1520-8532. doi: 10.1364/JOSAA.33.000B36. URL <https://opg.optica.org/josaa/abstract.cfm?uri=josaa-33-7-B36>. Publisher: Optica Publishing Group.
- [87] Henry Pinkard and Laura Waller. A visual introduction to information theory, June 2022. URL <http://arxiv.org/abs/2206.07867>. arXiv:2206.07867 [cs, math].
- [88] Vasco Ronchi. Resolving Power of Calculated and Detected Images. *Journal of the Optical Society of America*, 51(4):458–460, April 1961. ISSN 0030-3941. doi: 10.1364/JOSA.51.0458\_1. URL [https://www.osapublishing.org/abstract.cfm?URI=josa-51-4-458\\_1](https://www.osapublishing.org/abstract.cfm?URI=josa-51-4-458_1).
- [89] C.E. Shannon. Communication in the Presence of Noise. *Proceedings of the IRE*, 37(1):10–21, January 1949. ISSN 2162-6634. doi: 10.1109/JRPROC.1949.232969. Conference Name: Proceedings of the IRE.
- [90] Massimo Franceschetti. *Wave Theory of Information*. Cambridge University Press, 1 edition, November 2017. ISBN 978-1-139-13633-4. doi: 10.1017/9781139136334. URL <https://www.cambridge.org/core/product/identifier/9781139136334/type/book>.
- [91] J. L. Harris. Resolving Power and Decision Theory. *Journal of the Optical Society of America*, 54(5):606, May 1964. ISSN 0030-3941. doi: 10.1364/JOSA.54.000606. URL <https://opg.optica.org/abstract.cfm?URI=josa-54-5-606>.
- [92] R. Heintzmann and V. Sarafis. Two point resolution in incoherent imaging. *Optik*, 112(3):114–118, 2001. ISSN 00304026. doi: 10.1078/0030-4026-00022. URL <https://linkinghub.elsevier.com/retrieve/pii/S0030402604700212>.
- [93] Joseph W. Goodman. *Introduction to Fourier optics*. Roberts & Co, Englewood, Colo, 3rd ed edition, 2005. ISBN 978-0-9747077-2-3. OCLC: ocm56632414.
- [94] Benigno Uria, Marc Alexandre Cote, Karol Gregor, Iain Murray, and Hugo Larochelle. Neural autoregressive distribution estimation. *Journal of Machine Learning Research*, 17:1–37, 2016. ISSN 15337928. arXiv: 1605.02226.
- [95] Mathieu Germain, Karol Gregor, Iain Murray, and Hugo Larochelle. MADE: Masked Autoencoder for Distribution Estimation. In Francis Bach and David Blei, editors, *Proceedings of the 32nd International Conference on Machine Learning*, volume 37 of *Proceedings of Machine Learning Research*, pages 881–889, Lille, France, July 2015. PMLR. URL <https://proceedings.mlr.press/v37/germain15.html>.
- [96] Jongchan Park, David J. Brady, Guoan Zheng, Lei Tian, and Liang Gao. Review of bio-optical imaging systems with a high space-bandwidth product. *Advanced Photonics*, 3(04):369–407, June 2021. ISSN 2577-5421. doi: 10.1117/1.AP.3.4.044001. URL <https://royalsocietypublishing.org/doi/10.1098/rsta.1955.0001>.
- [97] H. Nyquist. Certain Topics in Telegraph Transmission Theory. *Transactions of the American Institute of Electrical Engineers*, 47(2):617–644, April 1928. ISSN 2330-9431. doi: 10.1109/T-AIEE.1928.5055024. URL <https://ieeexplore.ieee.org/document/5055024>. Conference Name: Transactions of the American Institute of Electrical Engineers.
- [98] Kevin Smith, Yunpeng Li, Filippo Piccinini, Gabor Csucs, Csaba Balazs, Alessandro Bevilacqua, and Peter Horvath. CIDRE: An illumination-correction method for optical microscopy. *Nature Methods*, 12(5):404–406, 2015. ISSN 15487105. doi: 10.1038/nmeth.3323.
- [99] Tingying Peng, Kurt Thorn, Timm Schroeder, Lichao Wang, Fabian J. Theis, Carsten Marr, and Nassir Navab. A BaSiC tool for background and shading correction of optical microscopy images. *Nature Communications*, 8:1–7, 2017. ISSN 20411723. doi: 10.1038/ncomms14836. URL <http://dx.doi.org/10.1038/ncomms14836>. Publisher: Nature Publishing Group.

- [100] J. Beirlant, E. Dudewicz, L. Györfi, and I. Denes. Nonparametric entropy estimation. An overview. *International Journal of Mathematical and Statistical Sciences*, 6(1):17–39, 1997. URL <https://www.semanticscholar.org/paper/Nonparametric-entropy-estimation.-An-overview-Beirlant-Dudewicz/14ba9dccb06355d1c6478b843ccb8f56d7374409>.
- [101] Lyudmyla F. Kozachenko and Nikolai N. Leonenko. Sample estimate of the entropy of a random vector. *Problemy Peredachi Informatsii*, 23(2):9–16, 1987. Publisher: Russian Academy of Sciences, Branch of Informatics, Computer Equipment and ...
- [102] Damiano Lombardi and Sanjay Pant. A non-parametric k-nearest neighbour entropy estimator. *Physical Review E*, 93(1):013310, January 2016. ISSN 2470-0045, 2470-0053. doi: 10.1103/PhysRevE.93.013310. URL <http://arxiv.org/abs/1506.06501>. arXiv:1506.06501 [cs, math].
- [103] Jiantao Jiao, Weihao Gao, and Yanjun Han. The Nearest Neighbor Information Estimator is Adaptively Near Minimax Rate-Optimal, September 2018. URL <http://arxiv.org/abs/1711.08824>. arXiv:1711.08824 [cs, math, stat].
- [104] Kristina Monakhova, Stephan R. Richter, Laura Waller, and Vladlen Koltun. Dancing under the stars: video denoising in starlight. In *2022 IEEE/CVF Conference on Computer Vision and Pattern Recognition (CVPR)*, pages 16220–16230, New Orleans, LA, USA, June 2022. IEEE. ISBN 978-1-66546-946-3. doi: 10.1109/CVPR52688.2022.01576. URL <https://ieeexplore.ieee.org/document/9879972/>.
- [105] Alexander Krull, Tomáš Vičar, Mangal Prakash, Manan Lalit, and Florian Jug. Probabilistic Noise2Void: Unsupervised Content-Aware Denoising. *Frontiers in Computer Science*, 2:5, February 2020. ISSN 2624-9898. doi: 10.3389/fcomp.2020.00005. URL <https://www.frontiersin.org/article/10.3389/fcomp.2020.00005/full>.
- [106] Ivan Kobyzev, Simon J. D. Prince, and Marcus A. Brubaker. Normalizing Flows: An Introduction and Review of Current Methods. *IEEE Transactions on Pattern Analysis and Machine Intelligence*, 43(11):3964–3979, November 2021. ISSN 0162-8828, 2160-9292, 1939-3539. doi: 10.1109/TPAMI.2020.2992934. URL <http://arxiv.org/abs/1908.09257>. arXiv:1908.09257 [cs, stat].
- [107] Jascha Sohl-Dickstein, Eric A. Weiss, Niru Maheswaranathan, and Surya Ganguli. Deep Unsupervised Learning using Nonequilibrium Thermodynamics, November 2015. URL <http://arxiv.org/abs/1503.03585>. arXiv:1503.03585 [cond-mat, q-bio, stat].
- [108] Yang Song and Diederik P. Kingma. How to Train Your Energy-Based Models, 2021. URL <http://arxiv.org/abs/2101.03288>. arXiv: 2101.03288.
- [109] Lucas Theis, Aäron van den Oord, and Matthias Bethge. A note on the evaluation of generative models, April 2016. URL <http://arxiv.org/abs/1511.01844>. arXiv:1511.01844 [cs, stat].
- [110] Diederik P Kingma, Tim Salimans, Ben Poole, and Jonathan Ho. On density estimation with diffusion models. In A. Beygelzimer, Y. Dauphin, P. Liang, and J. Wortman Vaughan, editors, *Advances in neural information processing systems*, 2021. URL <https://openreview.net/forum?id=2LdBqxc1Yv>.
- [111] Christopher M. Bishop. Mixture Density Networks. Technical Report NCRG/94/004, Aston University, 1994.
- [112] Kurt Hornik, Maxwell Stinchcombe, and Halbert White. Multilayer feedforward networks are universal approximators. *Neural Networks*, 2(5):359–366, January 1989. ISSN 08936080. doi: 10.1016/0893-6080(89)90020-8. URL <https://linkinghub.elsevier.com/retrieve/pii/0893608089900208>.
- [113] Matthew D. Hoffman, David M. Blei, Chong Wang, and John Paisley. Stochastic variational inference. *Journal of Machine Learning Research*, 14(2):1303–1347, 2013. ISSN 15324435. arXiv: 1206.7051.

- [114] Yann LeCun, Léon Bottou, Yoshua Bengio, and Patrick Haffner. Gradient-based learning applied to document recognition. *Proceedings of the IEEE*, 86(11):2278–2323, 1998. ISSN 00189219. doi: 10.1109/5.726791.
- [115] Dongning Guo. The Interplay Between Information and Estimation Measures. *Foundations and Trends® in Signal Processing*, 6(4):243–429, 2013. ISSN 1932-8346, 1932-8354. doi: 10.1561/20000000018. URL <http://nowpublishers.com/articles/foundations-and-trends-in-signal-processing/SIG-018>.
- [116] E.J. Candes and M.B. Wakin. An Introduction To Compressive Sampling. *IEEE Signal Processing Magazine*, 25(2):21–30, 2008. ISSN 1053-5888. doi: 10.1109/MSP.2007.914731. arXiv: 1307.1360v1.
- [117] Sri Rama Prasanna Pavani and Rafael Piestun. High-efficiency rotating point spread functions. *Optics Express*, 16(5):3484, March 2008. ISSN 1094-4087. doi: 10.1364/OE.16.003484. URL <https://opg.optica.org/abstract.cfm?URI=oe-16-5-3484>.
- [118] Sri Rama Prasanna Pavani and Rafael Piestun. Three dimensional tracking of fluorescent microparticles using a photon-limited double-helix response system. *Optics Express*, 16(26):22048–22057, December 2008. ISSN 1094-4087. doi: 10.1364/OE.16.022048. URL <https://opg.optica.org/oe/abstract.cfm?uri=oe-16-26-22048>. Publisher: Optica Publishing Group.
- [119] Yoav Shechtman, Steffen J. Sahl, Adam S. Backer, and W. E. Moerner. Optimal point spread function design for 3D imaging. *Physical Review Letters*, 113(3), September 2014. ISSN 10797114. doi: 10.1103/PhysRevLett.113.133902. Publisher: American Physical Society.
- [120] Ginni Grover, Sri Rama Prasanna Pavani, and Rafael Piestun. Performance limits on three-dimensional particle localization in photon-limited microscopy. *Optics Letters*, 35(19):3306, October 2010. ISSN 0146-9592. doi: 10.1364/OL.35.003306. URL <https://opg.optica.org/abstract.cfm?URI=ol-35-19-3306>.
- [121] Sean Quirin, Sri Rama Prasanna Pavani, and Rafael Piestun. Optimal 3D single-molecule localization for superresolution microscopy with aberrations and engineered point spread functions. *Proceedings of the National Academy of Sciences*, 109(3):675–679, January 2012. ISSN 0027-8424. doi: 10.1073/pnas.1109011108. URL <https://pnas.org/doi/full/10.1073/pnas.1109011108>.
- [122] Elias Nehme, Daniel Freedman, Racheli Gordon, Boris Ferdman, Lucien E. Weiss, Onit Alalouf, Tal Naor, Reut Orange, Tomer Michaeli, and Yoav Shechtman. DeepSTORM3D: dense 3D localization microscopy and PSF design by deep learning. *Nature Methods*, 17(7):734–740, July 2020. ISSN 1548-7105. doi: 10.1038/s41592-020-0853-5. URL <https://www.nature.com/articles/s41592-020-0853-5>. Number: 7 Publisher: Nature Publishing Group.
- [123] Dorian Bouchet, Jonathan Dong, Dante Maestre, and Thomas Juffmann. Fundamental Bounds on the Precision of Classical Phase Microscopes. *Physical Review Applied*, 15(2):024047, February 2021. ISSN 2331-7019. doi: 10.1103/PhysRevApplied.15.024047. URL <https://link.aps.org/doi/10.1103/PhysRevApplied.15.024047>.
- [124] David J. Lee, Michael C. Roggemann, and Byron M. Welsh. Cramér–Rao analysis of phase-diverse wave-front sensing. *Journal of the Optical Society of America A*, 16(5):1005, May 1999. ISSN 1084-7529, 1520-8532. doi: 10.1364/JOSAA.16.001005. URL <https://opg.optica.org/abstract.cfm?URI=josaa-16-5-1005>.
- [125] Jonathan Dong, Dante Maestre, Clara Conrad-Billroth, and Thomas Juffmann. Fundamental bounds on the precision of iSCAT, COBRI and dark-field microscopy for 3D localization and mass photometry. *Journal of Physics D: Applied Physics*, 54(39):394002, September 2021. ISSN 0022-3727, 1361-6463. doi: 10.1088/1361-6463/ac0f22. URL <https://iopscience.iop.org/article/10.1088/1361-6463/ac0f22>.

- [126] Zhou Wang and A.C. Bovik. Mean squared error: Love it or leave it? A new look at Signal Fidelity Measures. *IEEE Signal Processing Magazine*, 26(1):98–117, January 2009. ISSN 1053-5888. doi: 10.1109/MSP.2008.930649. URL <http://ieeexplore.ieee.org/document/4775883/>.
- [127] Richard D. Gill and Boris Y. Levit. Applications of the van Trees Inequality: A Bayesian Cramér-Rao Bound. *Bernoulli*, 1(1/2):59, March 1995. ISSN 13507265. doi: 10.2307/3318681. URL <https://www.jstor.org/stable/3318681?origin=crossref>.
- [128] Efe Aras, Kuan-Yun Lee, Ashwin Pananjady, and Thomas A. Courtade. A Family of Bayesian Cramer-Rao Bounds, and Consequences for Log-Concave Priors, February 2019. URL <http://arxiv.org/abs/1902.08582>. arXiv:1902.08582 [cs, math].
- [129] Trevor Hastie, Robert Tibshirani, and Jerome Friedman. *The Elements of Statistical Learning*. Springer Series in Statistics. Springer New York, New York, NY, 2009. ISBN 978-0-387-84858-7. doi: 10.1007/978-0-387-84858-7. URL <http://link.springer.com/10.1007/978-0-387-84858-7>.
- [130] W. James and Charles Stein. Estimation with Quadratic Loss. In Samuel Kotz and Norman L. Johnson, editors, *Breakthroughs in Statistics*, pages 443–460. Springer New York, New York, NY, 1992. ISBN 978-0-387-94037-3. doi: 10.1007/978-1-4612-0919-5\_30. URL [http://link.springer.com/10.1007/978-1-4612-0919-5\\_30](http://link.springer.com/10.1007/978-1-4612-0919-5_30). Series Title: Springer Series in Statistics.
- [131] Yann Lecun, Yoshua Bengio, and Geoffrey Hinton. Deep learning. *Nature*, 521(7553):436–444, 2015. ISSN 14764687. doi: 10.1038/nature14539. URL <http://www.scopus.com/inward/record.url?eid=2-s2.0-84930630277&partnerID=40&md5=befeefa64ddca265c713cf81f4e2fc54>. arXiv: 1312.6184v5 ISBN: 3135786504.
- [132] Harry L. Van Trees. *Detection, estimation, and modulation theory*. Wiley, New York, 2001. ISBN 978-0-471-09517-0.
- [133] Z. Wang, A.C. Bovik, H.R. Sheikh, and E.P. Simoncelli. Image Quality Assessment: From Error Visibility to Structural Similarity. *IEEE Transactions on Image Processing*, 13(4): 600–612, April 2004. ISSN 1057-7149. doi: 10.1109/TIP.2003.819861. URL <http://ieeexplore.ieee.org/document/1284395/>.
- [134] Richard Zhang, Phillip Isola, Alexei A. Efros, Eli Shechtman, and Oliver Wang. The Unreasonable Effectiveness of Deep Features as a Perceptual Metric, April 2018. URL <http://arxiv.org/abs/1801.03924>. arXiv:1801.03924 [cs].
- [135] S Yu Efroimovich. Information contained in a sequence of observations. *Problems in Information Transmission*, 15:24–39, 1980.
- [136] Kuan-Yun Lee. *New information inequalities with applications to statistics*. phd, University of California, Berkeley, 2022.
- [137] D. Guo, S. Shamai, and S. Verdu. Mutual Information and Minimum Mean-Square Error in Gaussian Channels. *IEEE Transactions on Information Theory*, 51(4):1261–1282, April 2005. ISSN 0018-9448. doi: 10.1109/TIT.2005.844072. URL <http://ieeexplore.ieee.org/document/1412024/>.
- [138] Emmanuel J. Candès and Mark A. Davenport. How well can we estimate a sparse vector?, March 2013. URL <http://arxiv.org/abs/1104.5246>. arXiv:1104.5246 [cs, math, stat].
- [139] Ashish Bora, Ajil Jalal, Eric Price, and Alexandros G. Dimakis. Compressed Sensing using Generative Models, March 2017. URL <http://arxiv.org/abs/1703.03208>. arXiv:1703.03208 [cs, math, stat].
- [140] Xiaohan Wei, Zhuoran Yang, and Zhaoran Wang. On the statistical rate of nonlinear recovery in generative models with heavy-tailed data. In Kamalika Chaudhuri and Ruslan Salakhutdinov, editors, *Proceedings of the 36th international conference on machine learning*, volume 97 of *Proceedings of machine learning research*, pages 6697–6706. PMLR, June 2019. URL <https://proceedings.mlr.press/v97/wei19b.html>.

- [141] Dustin G. Mixon and Soledad Villar. SUNLayer: Stable denoising with generative networks, March 2018. URL <http://arxiv.org/abs/1803.09319>. arXiv:1803.09319 [cs, stat].
- [142] Richard G. Baraniuk, Volkan Cevher, Marco F. Duarte, and Chinmay Hegde. Model-Based Compressive Sensing, December 2009. URL <http://arxiv.org/abs/0808.3572>. arXiv:0808.3572 [cs, math].
- [143] Martin J. Wainwright. Information-theoretic limits on sparsity recovery in the high-dimensional and noisy setting, February 2007. URL <http://arxiv.org/abs/math/0702301>. arXiv:math/0702301.
- [144] Yihong Wu and Sergio Verdu. Rényi Information Dimension: Fundamental Limits of Almost Lossless Analog Compression. *IEEE Transactions on Information Theory*, 56(8):3721–3748, August 2010. ISSN 0018-9448, 1557-9654. doi: 10.1109/TIT.2010.2050803. URL <http://ieeexplore.ieee.org/document/5508633/>.
- [145] David L. Donoho, Adel Javanmard, and Andrea Montanari. Information-Theoretically Optimal Compressed Sensing via Spatial Coupling and Approximate Message Passing, January 2013. URL <http://arxiv.org/abs/1112.0708>. arXiv:1112.0708 [cond-mat, stat].
- [146] Galen Reeves and Michael Gastpar. The Sampling Rate-Distortion Tradeoff for Sparsity Pattern Recovery in Compressed Sensing, June 2012. URL <http://arxiv.org/abs/1006.3128>. arXiv:1006.3128 [cs, math].
- [147] Aviad Levis, Daeyoung Lee, Joel A. Tropp, Charles F. Gammie, and Katherine L. Bouman. Inference of Black Hole Fluid-Dynamics from Sparse Interferometric Measurements. In *2021 IEEE/CVF International Conference on Computer Vision (ICCV)*, pages 2320–2329, Montreal, QC, Canada, October 2021. IEEE. ISBN 978-1-66542-812-5. doi: 10.1109/ICCV48922.2021.00234. URL <https://ieeexplore.ieee.org/document/9711239/>.
- [148] Andrew A. Chael, Michael D. Johnson, Katherine L. Bouman, Lindy L. Blackburn, Kazunori Akiyama, and Ramesh Narayan. Interferometric Imaging Directly with Closure Phases and Closure Amplitudes. *The Astrophysical Journal*, 857(1):23, April 2018. ISSN 0004-637X, 1538-4357. doi: 10.3847/1538-4357/aab6a8. URL <https://iopscience.iop.org/article/10.3847/1538-4357/aab6a8>.
- [149] Yvette Y. Lin, Angela F. Gao, and Katherine L. Bouman. Imaging An Evolving Black Hole By Leveraging Shared Structure. In *ICASSP 2024 - 2024 IEEE International Conference on Acoustics, Speech and Signal Processing (ICASSP)*, pages 2475–2479, Seoul, Korea, Republic of, April 2024. IEEE. doi: 10.1109/ICASSP48485.2024.10445896. URL <https://ieeexplore.ieee.org/document/10445896/>.
- [150] Alex Krizhevsky. *Learning Multiple Layers of Features from Tiny Images*. PhD thesis, University of Toronto, 2009.
- [151] Gao Huang, Zhuang Liu, Laurens Van Der Maaten, and Kilian Q. Weinberger. Densely connected convolutional networks. *Proceedings - 30th IEEE Conference on Computer Vision and Pattern Recognition, CVPR 2017*, 2017-Janua:2261–2269, 2017. ISSN 0022-4790. doi: 10.1109/CVPR.2017.243. arXiv: 1608.06993 ISBN: 9781538604571.

## **Supplementary materials**

## Contents

<b>S1 Information encoding formalism</b>	<b>27</b>
S1.1 Minimal probabilistic model of an imaging system	27
S1.1.1 Separation of encoding and noise	28
S1.1.2 Visualizing high-dimensional distributions in energy coordinates	28
S1.1.3 Mathematical formalism for encoders	29
S1.2 Probabilistic two-point resolution	31
S1.3 Encoder inefficiency in 1D	32
S1.4 Effects of signal-to-noise ratio, resolution, and sampling on information	36
S1.4.1 Full mathematical treatment of two-point resolution	38
S1.5 Expanded model	40
S1.5.1 Encoder uncertainty and calibration	40
S1.5.2 Task-specific information	41
<b>S2 Estimating information: Theory</b>	<b>42</b>
S2.1 Background	42
S2.2 Mutual information estimator	42
S2.3 Estimating conditional entropy of measurement noise	43
S2.3.1 Conditionally independent noise at each pixel	44
S2.3.2 Conditional entropy with additive Gaussian noise	44
S2.3.3 Conditional entropy with shot noise	45
S2.4 Estimating entropy of noisy images	46
S2.5 Probabilistic models	47
S2.5.1 Full Gaussian process	47
S2.5.2 Stationary Gaussian process	47
S2.5.3 PixelCNN	48
S2.6 Sampling and likelihood evaluation	49
S2.7 Accounting for encoder uncertainty	50
<b>S3 Estimating information: Experiments</b>	<b>50</b>
S3.1 Fitting stationary Gaussian processes	50
S3.2 Comparing stationary Gaussian process and PixelCNN estimates	51
S3.3 Failures of stationary Gaussian estimates on highly non-Gaussian data	54
S3.4 Model training times	56
S3.5 Conditional entropy estimates on noisy data	56
S3.6 Comparing analytic and upper bound entropy estimates	58
<b>S4 Additional decoder experiments</b>	<b>59</b>
S4.1 Experimental evidence of encoder uncertainty effects	59
S4.2 Task-specific information in classification	59

<b>S5 Comparison to other frameworks</b>	<b>61</b>
S5.1 Estimation theory and the Cramér-Rao lower bound . . . . .	62
S5.1.1 Background: The Cramér-Rao lower bound in imaging . . . . .	63
S5.1.2 Cramér-Rao lower bound-based design and its limitations . . . . .	63
S5.1.3 The challenges of generalizing estimation-theoretic design . . . . .	65
S5.1.4 Connections between estimation and information theory . . . . .	66
S5.2 Compressed Sensing: Assumptions and Limitations . . . . .	67
<b>S6 Methods</b>	<b>68</b>
S6.1 Model training . . . . .	68
S6.2 Confidence intervals . . . . .	69
S6.3 Sample generation . . . . .	69
S6.4 Generation of synthetic experimental noise . . . . .	69
S6.5 Applications . . . . .	69
S6.5.1 Color Filter Array . . . . .	69
S6.5.2 Black hole imaging . . . . .	70
S6.5.3 Lensless imaging . . . . .	70
S6.5.4 LED array microscopy . . . . .	71
S6.6 Information Driven Encoder Analysis Learning (IDEAL) . . . . .	72
S6.7 1D simulations . . . . .	73

## S1 Information encoding formalism

Information theory enables quantification of uncertainty and randomness. A formal mathematical model of uncertainty and randomness requires probability. Thus in order to use information theory to analyze imaging systems, we must model them probabilistically.

This section assumes familiarity with probability and information theory fundamentals. A tutorial introduction to these concepts can be found in previous work [87], as well as the textbooks [69, 72] and Shannon's original paper [71].

### S1.1 Minimal probabilistic model of an imaging system

The minimal probabilistic model we present has been widely used in information-theoretic analyses of imaging systems [5, 14, 22, 31] and builds on established principles in statistical optics [32].

This minimal imaging system model involves three random variables (**Fig. S1**):

- The **object** has physical properties we want to measure
- The **noiseless image** is created when the imaging system encodes object properties through physical processes (e.g., electromagnetic fields in optical systems, pressure waves in ultrasound)
- The **noisy measurement** results from detection noise corrupting the noiseless image

Each variable is modeled as random to capture our uncertainty about its true value.

Information can be lost at two stages: During encoding, information may be irretrievably lost when creating the noiseless image (e.g., spatial frequencies beyond the system's passband). During detection, measurement noise further corrupts information present in the noiseless image. The goal of an imaging system is to preserve as much object information as possible through both encoding and detection.

Mathematically, these variables form a Markov chain with joint distribution:

$$p(\mathbf{o}, \mathbf{x}, \mathbf{y}) = p(\mathbf{o})p(\mathbf{x} | \mathbf{o})p(\mathbf{y} | \mathbf{x})$$

where:

- $p(\mathbf{o})$  is the distribution of possible objects
- $p(\mathbf{x} | \mathbf{o})$  is a mapping from objects to noiseless images
- $p(\mathbf{y} | \mathbf{x})$  represents the detection noise process

The relationship between object, noiseless image, and noisy measurement can be understood in two directions:

- Forward: Object  $\rightarrow$  Noiseless Image  $\rightarrow$  Noisy Measurement ( $p(\mathbf{o}, \mathbf{x}, \mathbf{y}) = p(\mathbf{o})p(\mathbf{x}|\mathbf{o})p(\mathbf{y}|\mathbf{x})$ )
- Reverse: Noisy Measurement  $\rightarrow$  Noiseless Image  $\rightarrow$  Object ( $p(\mathbf{o}, \mathbf{x}, \mathbf{y}) = p(\mathbf{y})p(\mathbf{x}|\mathbf{y})p(\mathbf{o}|\mathbf{x})$ )

The Data Processing Inequality [72] reveals key limitations in each direction:

- Forward:  $I(\mathbf{O}; \mathbf{X}) \geq I(\mathbf{O}; \mathbf{Y})$  - noise can only reduce information about the object.
- Reverse:  $I(\mathbf{Y}; \mathbf{X}) \geq I(\mathbf{Y}; \mathbf{O})$  - the measurement's ability to carry information about the object is limited by the information it carries about the noiseless image.

In our model, encoding is deterministic - each object maps to exactly one noiseless image ( $p(\mathbf{x} | \mathbf{o})$  is a Dirac delta function). This means the noiseless image's randomness comes entirely from object uncertainty. Consequently, any information the measurement contains about the object must equal the information preserved through noise:  $I(\mathbf{Y}; \mathbf{X}) = I(\mathbf{Y}; \mathbf{O})$ .

This equality is powerful - it means we can evaluate imaging system performance by measuring information between noiseless images and noisy measurements ( $I(\mathbf{X}; \mathbf{Y})$ ), without having to characterize the more challenging distribution over possible objects ( $p(\mathbf{o})$ ). While simplified object models can provide valuable insights - as in the two-point resolution case (Sec. S1.4.1) - real objects are rarely known well enough to create accurate models. By focusing on  $I(\mathbf{X}; \mathbf{Y})$ , we can develop practical methods for estimating information in imaging systems.

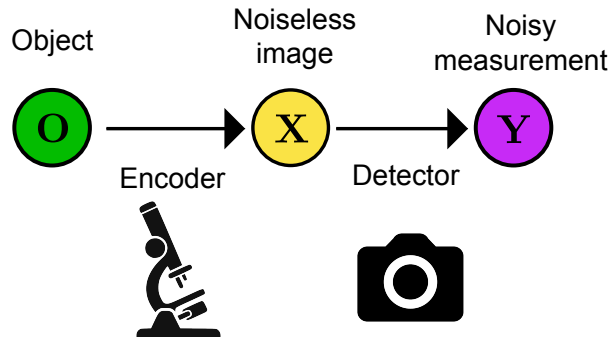


Figure S1: **A minimal probabilistic graphical model of an imaging system.** Three key variables describe the imaging process: (1) the object, which has unknown physical properties we want to measure, (2) the noiseless image, created when the imaging system encodes object properties through a deterministic process, and (3) the noisy measurement, produced when detection adds random noise to the noiseless image. The arrows show how information flows: the measurement can only reveal information about the object if that information was preserved in the noiseless image.

### S1.1.1 Separation of encoding and noise

This minimal model, which separates image encoding from detection noise, has been widely used in information-theoretic analyses of imaging systems [5, 14, 22, 31] and general imaging models [88]. For optical systems, this separation is justified by the “semi-classical” approach common in statistical optics [32]. This method treats light classically until it reaches the detector, where quantum effects introduce noise. Optical systems can experience two types of noise:

- **Classical noise** from fluctuations in light intensity (e.g., thermal light from a bulb or intensity variations in laser light)
- **Quantum “shot” noise** from the random arrival times of individual photons at the detector

In the visible spectrum, quantum noise typically dominates classical noise. This justifies treating light propagation as deterministic until it reaches the detector, where quantum effects become significant. This physical reality supports separating encoding and detection in optical systems.

### S1.1.2 Visualizing high-dimensional distributions in energy coordinates

The probability distributions over images ( $p(\mathbf{y})$ ) and measurements ( $p(\mathbf{x})$ ) are high-dimensional, and thus not possible to visualize directly. In microscopy, for example (Fig. S2a), a microscope transforms a distribution of possible cells into noiseless images, which detection then converts into noisy measurements. To provide insight into these complex distributions, we adapt a representation from [89] (Fig. S2b). This representation, which we call energy coordinates, offers a complementary perspective to the traditional spatial coordinate representation, enabling a more comprehensive understanding of image distributions and information flow in imaging systems.

Traditionally, images are represented in **spatial coordinates** – the normal way to show images, where each pixel’s intensity is plotted at its corresponding position in a 2D space. In this representation, each displayed image is a single sample drawn from the underlying probability distribution of all possible images. While intuitive and familiar, this representation doesn’t directly convey the statistical

properties of image distributions, as it only shows one or a few instances at a time rather than the full range of possibilities and their relative probabilities.

Alternatively, image distributions can be visualized in the **energy coordinate** representation, which shows the probability mass over pixel values. In this representation, each image of  $D$  pixels is a  $D$ -dimensional vector, and the  $D$ -dimensional probability density function describes how likely each image is. Low-dimensional projections of the full distribution, such as the marginal distribution  $p(x_k)$  or the joint distribution  $p(x_k, x_j)$  of two pixels can be plotted and provide insight into the full  $D$ -dimensional distribution's behavior.

Visualizing the distribution of noisy measurements for a single noiseless image (i.e.,  $p(\mathbf{y} | \mathbf{x})$ ) in energy coordinates demonstrates the effect of measurement noise (**Fig. S2c**). Noise spreads the probability mass further from the point corresponding to the noiseless image, which increases the overlap between noisy distributions of different images. This overlap makes it harder to determine the true object from a noisy measurement, with the extent of overlap determining how much object information is lost due to noise corruption.

The energy coordinate representation is particularly useful for comparing different imaging modalities (**Fig. S2d**). For example, when comparing two microscope illumination patterns with different spatial coherence, energy coordinates reveal how the encoders affect image distinguishability. An encoder using spatially incoherent illumination maps different objects to more similar images, resulting in overlapping measurement distributions that are difficult to distinguish. In contrast, an encoder using spatially coherent illumination creates more distinct images, leading to measurement distributions that remain separable even in the presence of noise. This visualization demonstrates how different illumination patterns affect the information content of the resulting measurements, with more distinct encoded images being more robust to noise corruption. This concept of distinguishability in the presence of noise is identical to the two-point resolution problem (See **Probabilistic two-point resolution**), only with spatial coherence as the variable parameter instead of signal-to-noise ratio and resolution. This demonstrates how the information-theoretic approach comprehensively captures imaging system performance while abstracting away the specific physical details of different imaging modalities.

### S1.1.3 Mathematical formalism for encoders

There is a family of encoders  $\mathcal{E}$  consisting of functions  $e_\theta : \mathcal{O} \rightarrow \mathcal{X}$ , where  $\mathcal{O}$  is the domain - the space of possible objects,  $\mathcal{X}$  is the codomain - the space of possible noiseless images, and  $\theta$  is the parameter(s) that define a particular encoder. For example, in the case of a linear, shift-invariant encoder,  $\mathcal{E}$  would be the set of all linear, shift-invariant functions and  $\theta$  would define a specific point spread function.

The action of an encoder is to take an object  $\mathbf{o} \in \mathcal{O}$  and form a noiseless image  $\mathbf{x} \in \mathcal{X}$  of it. This noiseless image will then undergo a measurement process, resulting in a noisy measurement  $\mathbf{y} \in \mathcal{Y}$ . The measurement process is modeled as a conditional probability distribution  $P_{\mathbf{Y}|\mathbf{X}}$ , which describes the probability of observing a particular noisy measurement given a particular noiseless image.

The information carried by noisy measurements is determined by the distributions  $P_{\mathbf{Y}|\mathbf{X}}$  and  $P_{\mathbf{X}}$ . It is quantified by the mutual information between the noiseless image and the noisy measurement,  $I(\mathbf{X}; \mathbf{Y})$ , which can be expressed as:

$$I(\mathbf{X}; \mathbf{Y}) = \mathbb{E}_{\mathbf{X}, \mathbf{Y}} \left[ \log \left( \frac{p(\mathbf{X}, \mathbf{Y})}{p(\mathbf{X})p(\mathbf{Y})} \right) \right] \quad (6)$$

where  $p(\mathbf{x}, \mathbf{y})$  is the joint probability of observing a particular noiseless image and a particular noisy measurement, and  $p(\mathbf{x})$  and  $p(\mathbf{y})$  are the marginal probabilities of observing a particular noiseless image and a particular noisy measurement, respectively.

Better encoders will produce noisy measurements that contain higher mutual information. It is thus of interest to investigate what limits the mutual information. One way of doing this is based on a decomposition of the mutual information into two terms:

$$I(\mathbf{X}; \mathbf{Y}) = H(\mathbf{X}) - H(\mathbf{X} | \mathbf{Y}) \quad (7)$$

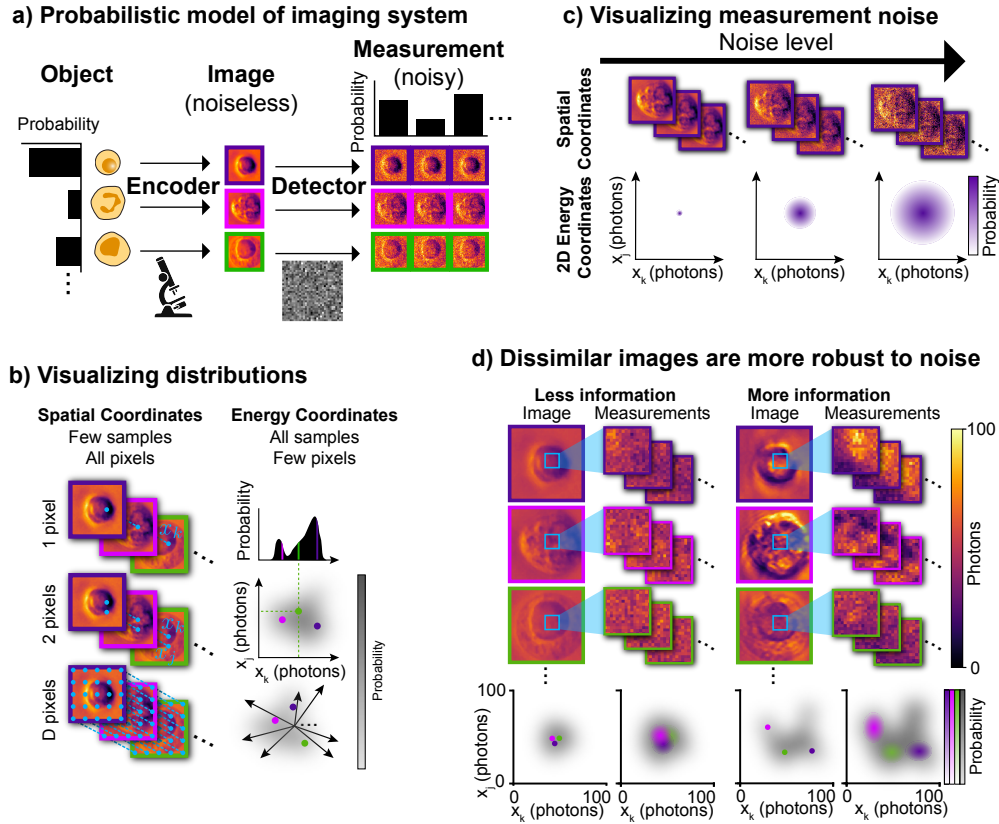


Figure S2: **Probabilistic modeling and visualization of imaging systems.** **a)** Probabilistic model of microscopy, in which a distribution of objects (cells) are encoded to a distribution of images by a microscope and detected as noisy measurements. **b)** Two complementary ways to visualize measurement distributions: spatial coordinates show all pixels for a few samples, while energy coordinates show the full probability distribution for selected pixels. **c)** Visualization of how measurement noise affects distributions: as noise increases, measurement probability spreads further from the noiseless value. **d)** Demonstration of how encoder design affects information preservation: more distinct noiseless images (right) create measurements that remain separable even with noise, while similar images (left) produce overlapping distributions that make object discrimination harder.

$H(\mathbf{X})$  is the entropy of the noiseless images, and  $H(\mathbf{X} | \mathbf{Y})$  is the conditional entropy of the noiseless images given the noisy measurements, which quantifies the uncertainty about the noiseless images that remains after observing the noisy measurements.

There are multiple ways of mathematically modeling the space of noiseless images  $\mathbf{X}$ , which depends on whether the images are continuous or discrete over space and in energy. For example, a model of noiseless images over continuous space and energy would be a space of continuous functions over space which output real numbers corresponding to an amount of energy, whereas a discrete model would be a space of finite-dimensional vectors that take discrete values (the number of photons) at a discrete set of locations (the pixels). Combinations of these are also possible, such as a continuous model over space and discrete model over energy, or a discrete model over space and continuous model over energy.

With any model, the space of noiseless images is ultimately finite in some sense. Energy cannot be infinitely concentrated in a single point<sup>1</sup>, and the physics of wave-propagation effectively constrain electromagnetic waves to a finite number of degrees of freedom [90]. This means that even in the

<sup>1</sup>...without collapsing space into a black hole [90]

continuous/continuous case, any noiseless image can be represented to an arbitrary level of precision by a finite number of samples.

It is thus of interest to understand the limits of the entropy of the noiseless images, because this will determine the limits of the mutual information. The space  $\mathbf{X}$  will have either finite volume or finite cardinality, as dictated by physical constraints. A uniform distribution over this space, in which all noiseless images are equally likely, will have the maximum possible entropy. However, due to their physical constraints, encoders will not in general be able to produce noiseless images that are uniformly distributed over  $\mathbf{X}$ , leading to an inefficiency in the amount of information that can be carried by the noisy measurements.

## S1.2 Probabilistic two-point resolution

To illustrate information-theoretic analysis of imaging systems, we first provide a simplified example: the classic two-point resolution problem. Typically, resolution is determined by the Abbe diffraction limit, which says that two diffraction-limited point sources will be “resolved” if they are sufficiently far apart (at least  $\lambda/(2NA)$ , where NA is the numerical aperture). The Abbe criteria, however, does not take into account the effects of noise, aberrations, coherence, or pixel sampling, among other factors. Our mutual information analysis can naturally incorporate all these effects into a single comprehensive metric.

We demonstrate with a simplified scenario, where the task is to distinguish between one point source or two closely spaced dimmer point sources, in the presence of measurement noise. We can derive the information content analytically for this idealized case (see **Section S1.4.1**) in which we model the object as either one point or two half-energy points, with equal probability [91, 92]. We assume that the imaging system has a diffraction-limited point spread function, with measurements corrupted by additive Gaussian noise (**Fig. S3a**). This simplified setup allow us to examine how information content accounts for both resolution and signal-to-noise ratio.

We seek to find the minimum numerical aperture needed to resolve two points that are spaced  $\delta d$  apart. The Abbe diffraction limit says the numerical aperture should be at least  $\lambda/(2\delta d)$ . However, without noise we can theoretically resolve any arbitrarily spaced points. Conversely, if there is a lot of noise, we need a larger numerical aperture than the Abbe limit predicts to resolve these same two points. Below, we show how mutual information can quantify this interplay between resolution and noise (**Fig. S3c**), predicting the achievable classification accuracy (**Fig. S3b**).

With two equally probable object states, the maximum possible information is 1 bit. Since the optical system is deterministic, it introduces no randomness and  $I(\mathbf{O}; \mathbf{Y}) = I(\mathbf{X}; \mathbf{Y})$  exactly, because the randomness in the object distribution is the only source of randomness in the noiseless image. This allows us to directly calculate the information preserved through the imaging process. Unlike the general case where we must estimate the entropy of measurements  $H(\mathbf{Y})$  through a cross-entropy upper bound, in this scenario we can derive the probability density of measurements analytically:

$$p(\mathbf{y}) = \frac{1}{2}\mathcal{N}(\mathbf{y}; \mathbf{x}_1, \sigma^2 I) + \frac{1}{2}\mathcal{N}(\mathbf{y}; \mathbf{x}_2, \sigma^2 I)$$

Here,  $\mathbf{x}_1$  is a vector of pixels for a noiseless image of a single point,  $\mathbf{x}_2$  is a vector corresponding to two points, and  $\mathcal{N}(\mathbf{y}; \boldsymbol{\mu}, \boldsymbol{\Sigma})$  is the multivariate normal probability density function.  $\sigma^2 I$  represents a diagonal covariance matrix with additive Gaussian noise with variance  $\sigma^2$  at each pixel.

Using this probability density, we can generate  $N$  samples from the distribution of measurements and use them to compute the entropy of measurements  $H(\mathbf{Y})$  using a Monte Carlo approximation:

$$\begin{aligned} H(\mathbf{Y}) &= \mathbb{E}[-\log p(\mathbf{Y})] \\ &\approx -\frac{1}{N} \sum_{i=1}^N \log p(\mathbf{y}_i) \end{aligned}$$

In this case of additive Gaussian noise,  $H(\mathbf{Y}|\mathbf{X})$  also has a closed form analytical expression (**Sec. S2.3.2**). Subtracting these two quantities enables computation of mutual information with error converging to zero as the number of samples increases.

In **Figure S3c**, we plot the mutual information for a range of diffraction-limited resolutions and signal-to-noise ratios. As expected, there is a trend towards more information for higher resolution (higher numerical aperture) systems and higher signal-to-noise ratio measurements. However, a high-resolution measurement can contain less information than a low-resolution one, if the low-resolution one has a sufficiently better signal-to-noise ratio. When mutual information is equal to 1 bit, the measurements can be classified as coming from one or two point sources with perfect accuracy. When mutual information is zero, the measurement contains no information about which of the two scenarios it is, so the best classifier will only achieve 50 percent accuracy through random guessing. **Figure S3b** shows this relation between mutual information and classification accuracy, after deriving an optimal classifier analytically. As expected, the more information preserved in the measurement, the better an optimal classifier can perform.

This two-point resolution example demonstrates how our unified treatment with information theory can evaluate resolution limits with noise effects taken into consideration. Such analysis can be extended to more complex imaging scenarios, where many different factors influence the encoder (e.g. aberrations, filters) and the measurement quality (e.g. spectral sensitivity, coherence). While our analysis here can provide valuable intuition about when two points will be “distinguishable,” real imaging scenarios involve high-dimensional measurements of complex objects. The key insight carries over: better encoders create measurements that are more distinguishable in the presence of noise. The geometric interpretation of these high-dimensional probability distributions provides additional insight into why information theory is well-suited for analyzing imaging systems (**Sec. S1.1.2**).

### S1.3 Encoder inefficiency in 1D

To understand how physical constraints limit information encoding, we expand on the 1D two-point resolution example to analyze a more general 1D model system of an imaging system. This example reveals a fundamental concept we call “encoder inefficiency” - the gap between theoretically optimal encoding and what physical constraints allow.

The family of encoders  $\mathcal{E}$  studied were 1D bandlimited, nonnegative, linear-shift invariant, infinitely periodic point spread functions. **Figure S4a** shows the outputs of a representative encoder in this family (i.e. a specific point spread function) acting on a distribution of delta function objects. This system can be thought of as a simplified version of an imaging system that uses spatially incoherent illumination, such as in photography or microscopy [93].

The set of possible output signals  $\mathbf{X}$  for this family of encoders is identical to the set of possible point spread functions: bandlimited, nonnegative, and infinitely periodic signals (**Fig. S6b**). These output signals (which are analogous to the noiseless images in discussed in **Formulation of information estimator**) can be viewed either in spatial coordinates, in which their energy density is plotted as a function of space, or in energy coordinates (**Fig. S2**), with values found by integrating areas of the signal corresponding to “pixels.”

Signals cannot have both finite bandwidth and finite extent in space, and they thus require infinite samples to represent with arbitrary accuracy in the absence of further constraints. This is typically handled in one of two ways: treating signals as both band-limited and spatially finite and sampling at finite density over finite extent; or considering band-limited signals with infinite spatial extent, which asymptotically have finite degrees of freedom and can thus be sampled at finite rates with arbitrary accuracy [90].

Here, we avoid these complications by considering band-limited signals that are infinitely periodic in space. This means the signal can be represented exactly by sampling at the Nyquist rate over a single period (because sampling beyond this period would yield the same values).

As a result of this simplification, there is a bijective mapping between the set of possible signals and non-negative vectors in  $D$ -dimensional space—that is, each signal in the set corresponds to a point in  $D$ -dimensional space (similar to the argument made in [89]). This allows us to computationally analyze this finite-dimensional space with insights that can be applied to the more complicated space of continuous signals.

As discussed in **Visualizing high-dimensional distributions in energy coordinates**, the effect of measurement noise in the energy coordinate representation is to turn a point (i.e. a signal/image)

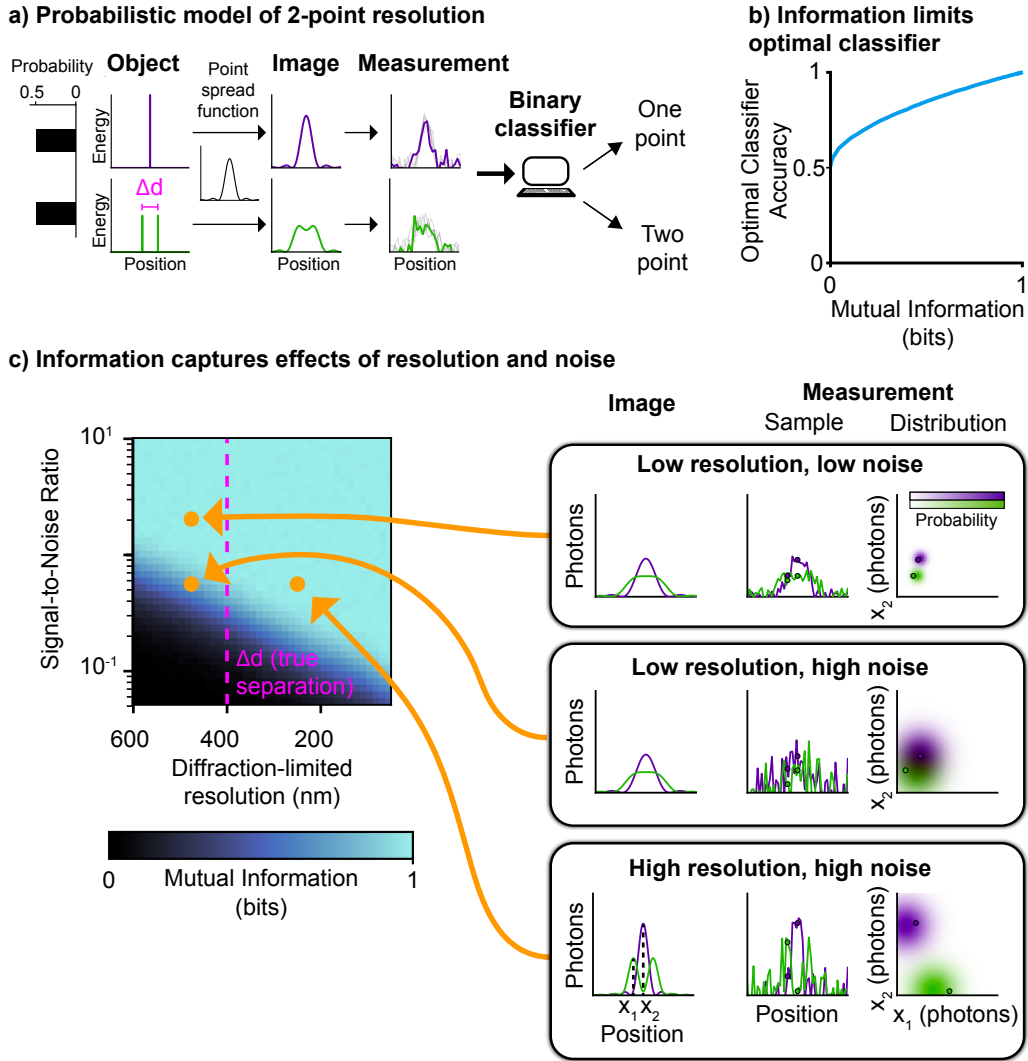
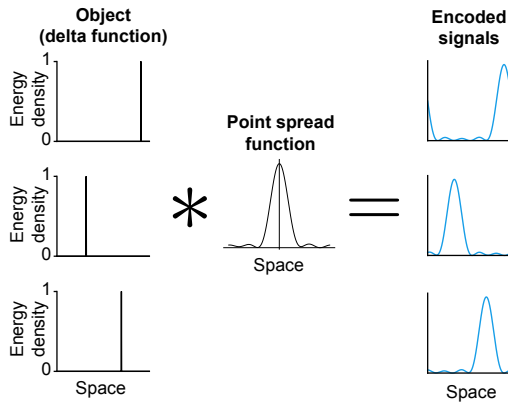


Figure S3: **Mutual information captures imaging trade-offs between resolution and noise for a simplified case of two-point resolution.** **a)** Probabilistic model of two-point resolution: an object (one point or two half-energy points) is blurred by a point spread function and corrupted by noise. A binary classifier attempts to determine the object type from the measurement. **b)** The accuracy of an optimal classifier is fundamentally limited by the information content of the measurements. **c)** Information analysis reveals how resolution and noise interact: (Left) information in measurement as a function of signal-to-noise ratio and diffraction-limited resolution. (Right) Example images, measurements, and measurement distributions (at pixel locations  $x_1$  and  $x_2$ ). The top row and bottom row achieve equivalent information with low-resolution, low-noise measurements and high-resolution, high noise measurements.

### a) Model system



### b) Output space: positive, bandlimited, periodic signals

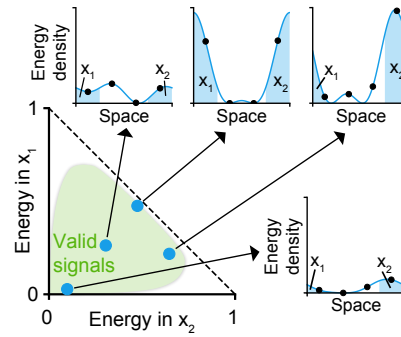


Figure S4: **1-dimensional model system.** **a)** An object distribution (e.g. a randomly-located delta function) and a linear, shift-invariant point spread function encoder. **b)**  $M$ -dimensional energy coordinate representation of the set of all encodable signals in which each signal corresponds to a single point.

into a cloud of probability mass representing the possible noisy realizations of that signal/image. Here we assume, without loss of generality, that all measurement noise is additive Gaussian (See **Conditional entropy with additive Gaussian noise**). The amount of information that can be encoded is determined by how well dispersed the distribution of encoded signals can be in this space such that the noisy versions of different signals minimally overlap. Thus, the volume of the space of possible signals is critical: it determines how much room there is to map different objects to non-overlapping signals. Though there are an infinite number of signals in the set, only a finite number can be distinguished with a given level of certainty in the presence of noise.

What is the volume of the space of possible signals? Given that all signals have energy  $\leq 1$ , the vector that defines their representation in energy coordinates must have  $L_1$  norm also  $\leq 1$ . Thus, all signals must correspond to points that lie inside the positive orthant of the  $L_1$  unit ball. However, not every point in this space will correspond to a valid signal: for example, a vector with a single 1 and the rest 0s will not be possible, because this would entail concentrating all of the signal's energy within a single pixel.

It is unclear to us if there is an analytical expression that defines the set of possible signals, but we can investigate the size of this set empirically. To do so, we set up an optimization problem in which we pick a fixed object and a target energy coordinate representation of a signal (e.g. a vector with a single 1 and the rest 0s). We then find the optimal point spread function that brings the object closest to the target signal by optimizing an encoder to minimize this distance using gradient descent. Repeating this experiment over a grid of target signals shows which signals can be reached, and which cannot, thereby revealing the limits of the space of possible signals.

Repeating this experiment with different fixed objects illustrates an important insight about encoders: Their range is object dependent (**Fig. S5**). This is a direct result of their physical constraints. The 1D encoder in this simulation is representative of imaging systems governed by intensity point spread functions [93]. Such encoders have at least two important physical constraints: 1) they can only reduce energy (if they attenuate light) or preserve it. They cannot, for example, encode a dim object to a signal with greater energy. 2) They can only disperse, and not re-concentrate, energy. Every point spread function (under the constraints of non-negativity and linear shift invariance) can only map objects to signals that are blurrier versions of themselves.

**Figure S5** shows the consequence of the second constraint for three different objects with equal energy. The single delta function in the top row can be encoded to the broadest range of possible signals, since it is the most concentrated to begin with. More dispersed objects, like the 8 delta functions each with  $\frac{1}{8}$  energy in the bottom row can only be encoded to a smaller volume of possible signals.

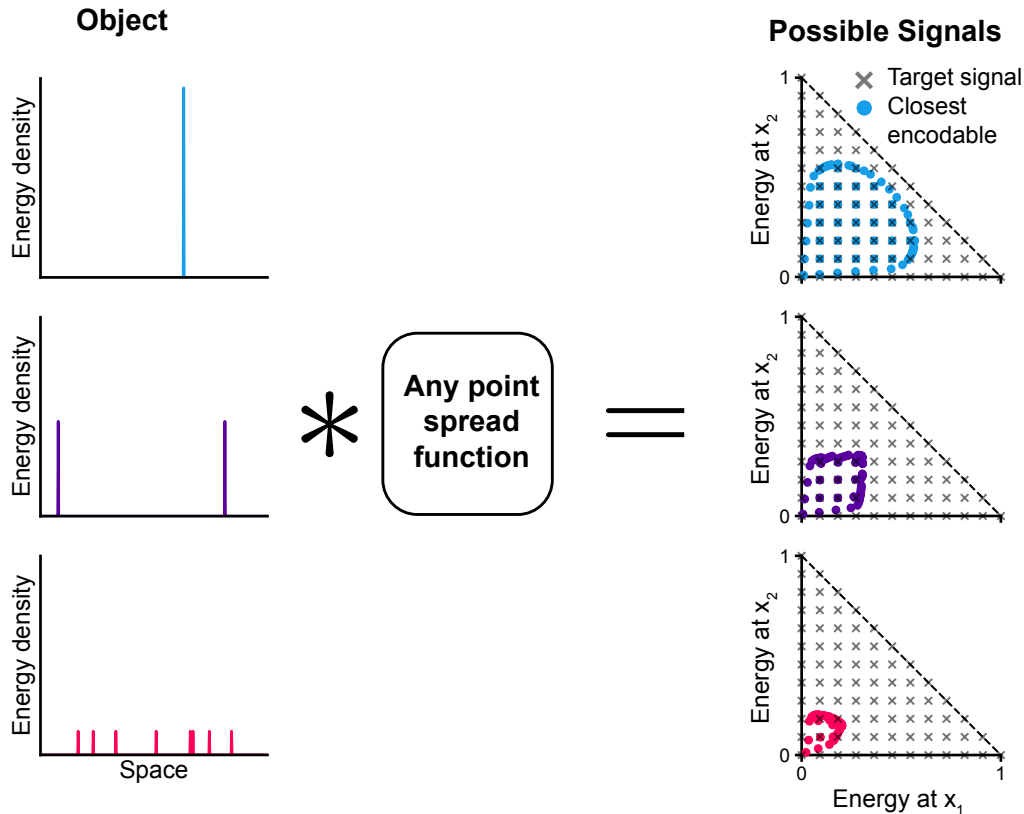


Figure S5: **Object-dependence of encoder range.** The set of signals encodable from an object depends on that object’s properties. More dispersed objects like the 8 delta functions (bottom) can only reach a subset of the signals reachable from a concentrated delta function (top), despite equal energies. This is due to physical constraints preventing reconcentrating energy. The closest encodable signals to the target signals were found by solving an optimization problem to find the optimal encoder that encodes the object to the target signal.

The range of a family of encoders for a fixed object of a particular type determines the volume of the set of possible encoded signals, and thus places an upper limit on the amount of encoded information. Physical constraints limit the functions an encoder family can implement. As a result, even optimal encoders generally cannot achieve the theoretically ideal signal distribution (which would be uniform over all possible signals when dealing with additive Gaussian noise). An encoder must handle not just one object, but an entire distribution of objects. While we might find different encoders that each map a specific object to a desired signal, no single encoder can optimally map all objects simultaneously. This fundamental limitation prevents achieving the theoretically ideal signal distribution.

Given three constraints - an object distribution, an energy limit on signals, and a noise model - the optimal signal distribution maximizes mutual information between objects and encoded signals. However, physical constraints and object-dependence often prevent encoder families from achieving this optimum. We define “encoder inefficiency” as the gap between this theoretical optimum and the best distribution achievable by a given encoder family.

We can measure encoder inefficiency experimentally using a simplified test case with delta functions of unit energy at random positions as objects, and additive Gaussian measurement noise. Under these conditions, the distribution of signals carrying maximum information has uniform probability over the set of possible signals.

To find the best achievable distribution, we first use Information-Driven Encoder Analysis Learning (IDEAL) (See **Information-Driven Encoder Analysis Learning (IDEAL)**) to learn the optimal encoder. We then generate random objects and encode them with this optimal encoder to sample

from the distribution of encoded signals, add noise, and estimate the mutual information. We use the PixelCNN-based estimator<sup>2</sup>, treating the signals as 2D images to match the estimator’s design.

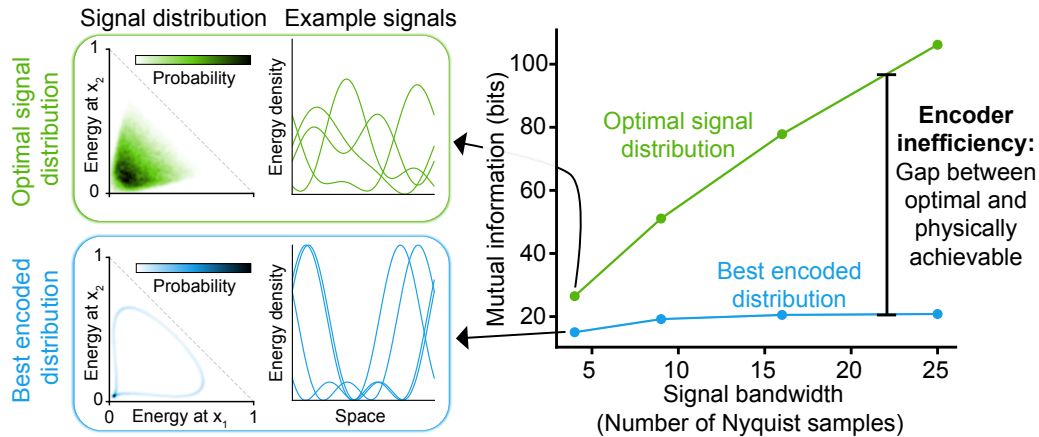


Figure S6: **Physical constraints limit the amount of information that can be encoded.** (Top left) The optimal distribution of energy limited signals for additive, signal-independent Gaussian noise is uniform (it appears non-uniform in this 2D projection of a 4D space). (Bottom left) The best encodable distribution using an optimal point spread function is far from uniform. (Right) The gap between the information in the optimal signal distribution and the best encodable distribution quantifies the inefficiency of the encoder family.

The results of this experiment are shown in **Figure S6**. The optimal point spread function encodes objects to only a small fraction of the total volume of possible signals, resulting in encoded signals that are significantly less random in appearance than the optimal uniform distribution of signals. (Note: the energy coordinate representation of these signals shown on the left side is a 2-dimensional projection of an  $D$ -dimensional space, with  $D = 4$  for the picture shown, which is why the distribution appears non-uniform.) The mutual information estimates shown on the right side demonstrate the gap between the optimal distribution of signals and the best encodable distribution given the family of linear, shift-invariant encoders.

#### S1.4 Effects of signal-to-noise ratio, resolution, and sampling on information

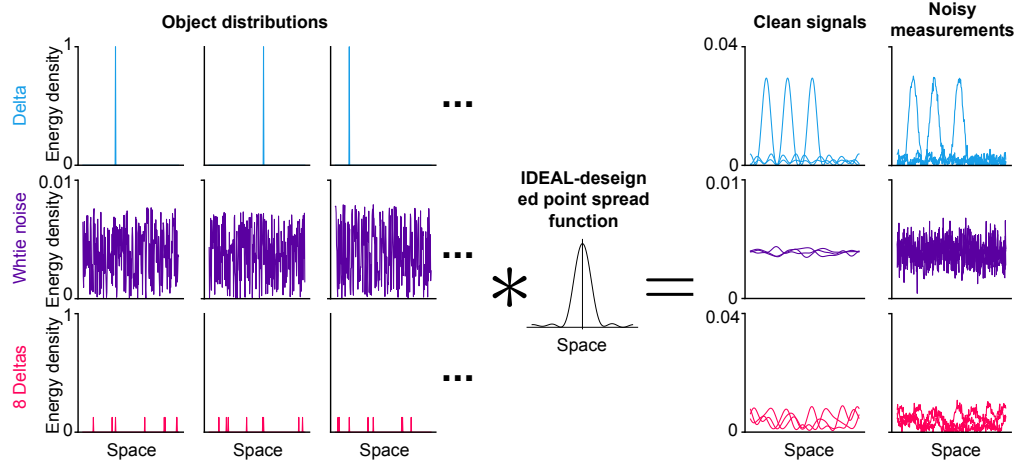
This same experimental setup can be used to investigate how different properties of the encoder/detection process, such as bandwidth, signal-to-noise ratio, and sampling density, affect the amount of information that can be encoded. These experiments provide insight into the tradeoffs between different system parameters as well as connections to the existing literature analyzing information in imaging systems.

**Signal-to-noise ratio** Signal-to-noise ratio is a key parameter in imaging systems, and it is widely-appreciated that higher signal-to-noise ratio is a desirable characteristic. For the additive Gaussian noise measurement model, noise is fixed, and the signal-to-noise ratio is determined by the amount of energy in the signal. It is simplest to consider the average signal-to-noise ratio over each signal, which can be found by dividing the energy of the signal by the standard deviation of the noise. Choosing an maximum average signal-to-noise ratio defines a set of signals that can be encoded, which consists of all possible signals with this average signal-to-noise ratio or less. This set has a finite volume, and thus a finite maximum amount of information that can be encoded. Within this set, there are subsets of signals that each have the same signal-to-noise ratio.

Sets of signals with higher average signal-to-noise ratios have increasing large volumes, and can thus carry larger amounts of information. As described in the previous section, physical constraints of encoders impose object-dependent limits on the the maximum amount of information that can be encoded. To test how the maximum average signal-to-noise ratio affects the amount of information

<sup>2</sup>We used PixelCNN for convenience, though estimators designed for 1D signals [94, 95] might provide better accuracy.

## a) Experimental framework



## b) Effects of measurement properties on information

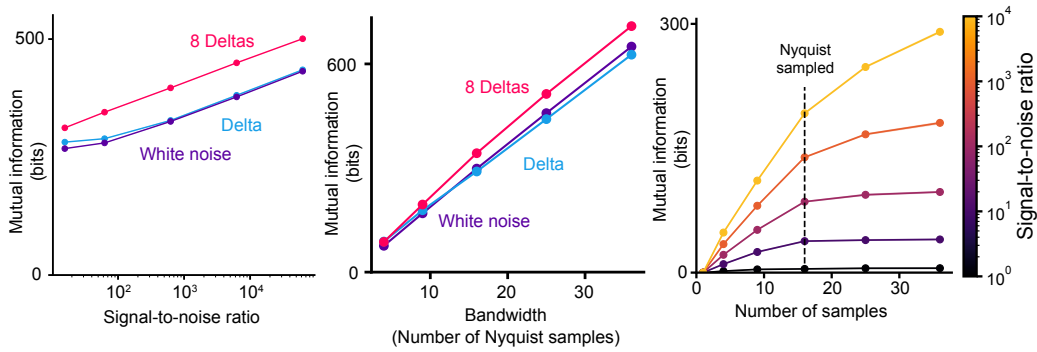


Figure S7: **Effects of signal-to-noise, space-bandwidth product, and sampling density on encoded information.** **a)** Samples from three different object distributions and the signals and noisy measurements to which they are encoded with an optimal point spread function. **b)** The amount of encoded information increases (Left) logarithmically with the average signal-to-noise ratio with object-dependent rates, (Middle) linearly with the space-bandwidth product of the signal with object-dependent rates. (Right) Sampling signals of fixed bandwidth at increasing densities increases the amount of encoded information, but with diminishing returns across different signal-to-noise ratios (for the 8 delta object distribution).

that can be encoded, we repeated the procedure described on three different distributions of objects: single, randomly-located, unit energy delta functions, 8 randomly-located, delta functions each with  $\frac{1}{8}$  energy, and unit energy white noise patterns (note, these are objects, not measurement noise) (**Fig. S7a**). The results show that for all three object distributions, the best encodable distribution of signals grows logarithmically with the average signal-to-noise ratio, with different objects having different absolute amounts of information for a given signal-to-noise ratio (**Fig. S7b, left**). This is consistent with the intuition that higher signal-to-noise ratio allows for more information to be encoded, and that the amount of information that can be encoded is object-dependent.

**Space-bandwidth product** Next, we tested the effect of signal bandwidth on information capacity. Optical imaging systems are often characterized in terms of their space-bandwidth product [96], and the space-bandwidth product is often used synonymously with the word “information.” A more accurate term for the space-bandwidth product is “degrees of freedom,” since it quantifies the potential complexity of an electromagnetic field wave propagating through the system [90]. Information (in Shannon’s entropy/mutual information sense) also depends on the signal-to-noise ratio and the object-dependent ability of encoders to map to distinct signals. In our numerical simulation, the spatial

extent of signals is fixed, so increasing the bandwidth of the signal increases the space-bandwidth product. We found that captured information increases linearly with the space-bandwidth product, with rate of increase depending on the object distribution (**Fig. S7b, center**).

**Sampling density** Finally, we examined the effect of sampling density on the amount of information that can be encoded. For a fixed bandwidth, the sampling density determines the number of pixels in the signal. The Nyquist sampling theorem [97, 89] states that a bandlimited signal can be perfectly reconstructed from its samples if the sampling density is at least twice the bandwidth. However, in the presence of noise, even when sampling at the Nyquist rate, there remains residual uncertainty about the signal, and additional samples can reduce this uncertainty. Experimentally, we found that, as expected, increasing the sampling density increases the amount of information, even beyond the Nyquist rate (**Fig. S7b, right**). However, the additional increases in information were progressively smaller. These results were consistent across both different object distributions and different average signal-to-noise ratios (for a delta function object distribution).

#### S1.4.1 Full mathematical treatment of two-point resolution

In this section we describe the example of 1-dimensional two-point resolution (See **Probabilistic two-point resolution**) in full mathematical detail. By making assumptions about the object distribution, the encoder, and the noise model, we can write down the exact probability density functions of the object, the noiseless image, and the noisy measurement. This enables writing an exact expression for the mutual information between object and noisy measurement, as well as the classification accuracy of the optimal binary classifier decoder that uses the noisy measurement to classify the object as being a single point source or two point sources.

**Object** The object is a mixture of two possibilities that each occur with probability  $\frac{1}{2}$ : Either a single point source with energy 1 or two point sources with energy  $\frac{1}{2}$  and separation distance  $\Delta$  with their midpoint at the same location as the single point source. We represent these objects mathematically as  $\mathbf{o}_1$  and  $\mathbf{o}_2$  respectively. Using  $r$  to denote spatial position, with the single-point source object located at  $r = 0$ :

$$\begin{aligned}\mathbf{o}_1(r) &= \delta(r) \\ \mathbf{o}_2(r) &= \frac{1}{2}\delta(r - \frac{\Delta}{2}) + \frac{1}{2}\delta(r + \frac{\Delta}{2})\end{aligned}$$

where  $\delta$  is the Dirac delta function.

The random object  $\mathbf{O}$  has probability  $\frac{1}{2}$  of being  $\mathbf{o}_1$  and  $\frac{1}{2}$  of being  $\mathbf{o}_2$ . Thus, its probability density function can be written as:

$$p(\mathbf{o}) = \frac{1}{2}\delta(\mathbf{o} - \mathbf{o}_1) + \frac{1}{2}\delta(\mathbf{o} - \mathbf{o}_2)$$

$\delta(\mathbf{o} - \mathbf{o}_1)$  is 1 when the object is  $\mathbf{o}_1$  and 0 otherwise, and similarly for  $\delta(\mathbf{o} - \mathbf{o}_2)$ .

**Encoder** The encoder is a 1-dimensional linear shift-invariant imaging system with a diffraction-limited intensity point spread function  $h(r)$ :

$$h(r) = \frac{\sin(\frac{2\pi\text{NA}}{\lambda}r)}{\frac{2\pi\text{NA}}{\lambda}r}$$

where NA is the numerical aperture of the system,  $\lambda$  is the wavelength of light, and  $r$  is the spatial coordinate.

The noiseless image is the convolution of the object with the point spread function:

$$\mathbf{x} = \mathbf{o} * h$$

This gives rise to two possible noiseless images,  $\mathbf{x}_1$  and  $\mathbf{x}_2$ , corresponding to the two possible objects  $\mathbf{o}_1$  and  $\mathbf{o}_2$  respectively. The probability density function of the random noiseless image  $\mathbf{X}$  is thus:

$$p(\mathbf{x}) = \frac{1}{2}\delta(\mathbf{x} - \mathbf{x}_1) + \frac{1}{2}\delta(\mathbf{x} - \mathbf{x}_2)$$

**Detector** The noisy measurement is formed by adding independent Gaussian noise with variance  $\sigma^2$  to each pixel of the noiseless image. We assume a pixel size much smaller than the minimum pixel size dictated by the Nyquist sampling theorem, so sampling effects minimally influence the results.

The random noisy measurement  $\mathbf{Y}$  is thus a length  $D$  vector of pixels. Its probability distribution is found by taking the mixture of two deltas distribution of the noiseless images and adding Gaussian noise to each pixel. This gives a mixture of two multivariate Gaussian distributions with mean vectors given by the noiseless images and a diagonal covariance matrix with variances equal to the noise variance. The probability density function of the noisy measurement is thus:

$$p(\mathbf{y}) = \frac{1}{2}\mathcal{N}(\mathbf{y}; \mathbf{x}_1, \sigma^2 I) + \frac{1}{2}\mathcal{N}(\mathbf{y}; \mathbf{x}_2, \sigma^2 I) \quad (8)$$

where  $\mathcal{N}(\mathbf{y}; \mathbf{x}, \sigma^2 I)$  is the multivariate Gaussian distribution with mean vector  $\boldsymbol{\mu} = \mathbf{x}$  and covariance matrix  $\boldsymbol{\Sigma} = \sigma^2 I$ .

**Mutual information** The mutual information between the object and the noisy measurement  $I(\mathbf{O}; \mathbf{Y})$  is equal to the mutual information between the noiseless image and the noisy measurement  $I(\mathbf{X}; \mathbf{Y})$ , since the object is fully determined by the noiseless image. We focus on the mutual information between the noiseless and noisy images, which can be calculated by decomposing it into a difference of entropies:

$$I(\mathbf{X}; \mathbf{Y}) = H(\mathbf{Y}) - H(\mathbf{Y}|\mathbf{X})$$

where  $H(\mathbf{Y})$  is the entropy of the noisy measurement and  $H(\mathbf{Y}|\mathbf{X})$  is the conditional entropy of the noisy measurement given the noiseless image.

Under the additive Gaussian noise model,  $H(\mathbf{Y}|\mathbf{X})$  is a constant that is a function of the the variance  $\sigma^2$  and the number of dimensions (pixels)  $D$ . It can be analytically simplified as shown in Equation 23.

The entropy of the noisy measurement  $H(\mathbf{Y})$  can be expanded as:

$$H(\mathbf{Y}) = -\mathbb{E}[\log p(\mathbf{y})]$$

Since we can easily generate samples from the distribution of the noisy measurements and we know the true probability density  $p(\mathbf{y})$ , we can estimate this entropy with a Monte Carlo approximation of  $N$  samples:

$$H(\mathbf{Y}) \approx -\frac{1}{N} \sum_{i=1}^N \log p(\mathbf{y}_i)$$

**Decoder** Since the goal of the imaging system in this simple example is to classify the object as being a single point source or two point sources [91], the decoder is a binary classifier that takes in the noisy measurement and outputs a decision as to whether the object was a single point or two points.

The optimal decoder is the Bayes classifier, which chooses the object class that maximizes the posterior probability given the noisy measurement. In this case, since the prior probabilities of the two object classes are equal, the Bayes classifier is equivalent to the maximum likelihood classifier, which chooses the object class that maximizes the likelihood of the noisy measurement.

Given the probability density of the noisy measurement in Equation 8, the Bayes/maximum likelihood classifier decides the object is two points if:

$$\mathcal{N}(\mathbf{y}; \mathbf{x}_2, \sigma^2 I) > \mathcal{N}(\mathbf{y}; \mathbf{x}_1, \sigma^2 I)$$

Plugging in the expressions for the multivariate Gaussian distributions, this simplifies to:

$$\|\mathbf{y} - \mathbf{x}_2\|^2 < \|\mathbf{y} - \mathbf{x}_1\|^2$$

In other words, the noisy measurement  $\mathbf{y}$  is classified as two points if its Euclidean distance to the noiseless image  $\mathbf{x}_2$  is less than its distance to  $\mathbf{x}_1$ , and classified as one point otherwise.

Using the analytic expressions for mutual information and classification accuracy, they can be shown to have a monotonic relationship with each other (**Fig. S8**). This demonstrates the fundamental link between the information content of the measurements and the achievable performance of downstream decoding in this minimal example.

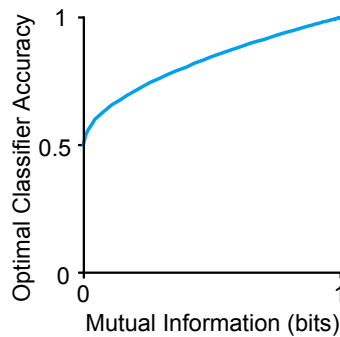


Figure S8: **Classification accuracy vs information in two-point resolution.** Performance of the optimal binary classifier decoder that uses the noisy measurement to classify the object as being a single point source or two point sources. The classification accuracy in this simple example has a monotonic relationship with the mutual information between the object/noiseless image and the noisy measurement.

## S1.5 Expanded model

The minimal model from the previous sections makes simplifying assumptions and abstracts away details that are relevant to real imaging systems. In the section we generalize to a more complex model, and explain the deeper insights and capabilities such a model can provide.

### S1.5.1 Encoder uncertainty and calibration

In the minimal model in the previous sections, the encoder function is fixed, so all variations in the noiseless images come from variations in the objects. This enables the simplifying assumption that the mutual information between the noisy measurements and noiseless images equals the mutual information between the noisy measurements and the objects:  $I(\mathbf{Y}; \mathbf{X}) = I(\mathbf{Y}; \mathbf{O})$ . As a result, estimating the former also reveals how much information about the objects is contained in the noisy measurements.

However, in practice the encoder may vary for different objects. For example, dust or imperfections in optical components, fluctuations in illumination brightness, and non-uniform resolution across the field of view can all change from measurement to measurement. Imaging systems are generally designed to minimize such variations - lenses provide uniform resolution across the field of view, light sources are engineered for stability, and care is taken to avoid dust in the optical path. But some degree of variation is inevitable.

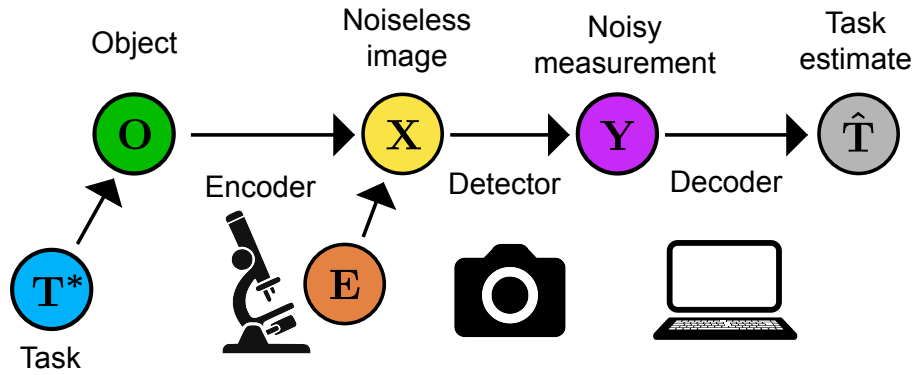


Figure S9: **An expanded probabilistic graphical model of an imaging system.** A generalization of the minimal probabilistic model in **Figure S1**, which in addition to modeling the object, noiseless image, and noisy measurement as random variables, also models randomness of the encoder, and the true and estimated values of the decoder task.

As a result, observing noisy measurements provides information both about the object and about the measurement system itself. Not accounting for encoder variations will lead to overestimates of the object information contained in the measurements.

The randomness of encoders is qualitatively different than the randomness caused by detection noise. Detection noise arises from inherently unpredictable quantum phenomena like photon arrival times. In contrast, the randomness of the encoder models a fixed but unknown distortion applied to the signal that, if learned, can be accounted for and will no longer be a source of randomness.

Mathematically, the encoder sits outside the Markov chain from object to image. Thus the data processing inequality does not imply permanent information loss as a result of its randomness. Through calibration, the nature of the distortion can be learned. Once characterized, the apparent randomness in future measurements is reduced, enabling recovery of information about the object. There are many examples of this concept in practice - deconvolution algorithms can incorporate spatially varying point spread functions, shading corrections can be applied to account for varied illumination of the field of view [98, 99], etc.

A similar calibration approach can be taken with information estimators to avoid over-estimating the object information in the measurement. We describe a theoretical framework for implementing this in **Section S2.7**, and demonstrate its practical importance through experiments with LED array microscopy in **Section S4.1**. These experiments show how failing to account for encoder uncertainty can significantly impact information estimates, particularly in sensitive imaging systems.

### S1.5.2 Task-specific information

Another useful generalization is to explicitly model the relationship between the decoding task and the object being imaged [23, 68]. For example, a perfect decoder for a specific task may require only a subset of the information needed to fully describe the object's physical properties. Alternatively, even complete knowledge of the object's physical properties may be insufficient to perfectly predict the task outcome - no encoder could encode enough task-relevant information to enable a flawless decoder.

To account for this, the model includes an additional random variable:

$T^*$  - the true value of the decoding task, which sits upstream of the object  $O$  in the Markov chain. This expresses that the object may not contain all task-relevant information, and also may contain additional irrelevant details.

The full Markov chain is now  $T^* \rightarrow O \rightarrow X \rightarrow Y$ . The key quantity of interest is  $I(T^*; Y)$ , the mutual information between the true task value and the noisy measurement. This quantifies how

much task-relevant information makes it through the entire imaging system. It can be substantially less than  $I(\mathbf{O}; \mathbf{Y})$ , as it excludes irrelevant object details.

The greater the disparity between  $I(\mathbf{T}^*; \mathbf{Y})$  and  $I(\mathbf{O}; \mathbf{Y})$ , the less predictive estimated information may be of decoder performance.

This seems especially likely when the task is very simple, capturing just a small fraction of the information in the measurements about the full object state. As an example, in **Section S4.2** we observe a scenario where a simple classification task requires only a small fraction of the information present in the full measurements.

## S2 Estimating information: Theory

In this section, we develop the mathematical framework for estimating information in imaging systems.

### S2.1 Background

As described in **Formulation of information estimator**, our probabilistic model represents noiseless images as a random 2D array  $\mathbf{X}$  with distribution  $p(\mathbf{x})$ , where each element quantifies the energy at a single pixel. The corresponding noisy measurements form array  $\mathbf{Y}$  with distribution  $p(\mathbf{y})$ . These distributions determine how much object-relevant information survives the measurement process.

We estimate  $I(\mathbf{X}; \mathbf{Y})$ , the mutual information between noiseless images and noisy measurements. The units are bits, which have a concrete operational meaning: in ideal conditions, each bit enables perfect discrimination between  $2^{I(\mathbf{X}; \mathbf{Y})}$  different objects. In practice, noise prevents such perfect discrimination—instead, each bit quantifies how well multiple object states can be partially distinguished from each other.

While imaging system performance typically varies across the field of view, we can quantify overall information content using a single value: the mutual information rate (information per pixel). This parallels how optical resolution is often characterized by a single number despite spatial variations [93].

### S2.2 Mutual information estimator

Mutual information estimation is a well-studied problem in many fields, including machine learning, neuroscience, and computational biology, and a number of different approaches have been proposed, some of which attempt to estimate mutual information directly [33–35], and others which try to infer its value by computing upper or lower bounds [43, 36]. It is a challenging statistical problem to solve in general, and many estimators and bounds are known to suffer from high bias and/or variance, particularly on high-dimensional problems [43, 36].

Many mutual information estimators rely on first estimating entropy, which is a measure of the uncertainty of a random variable. The outcome of random variables with higher entropy are more uncertain and harder to predict than the outcome of those with lower entropy, because they are more random. Equivalently, the higher a distribution’s entropy is, the more spread out it is, and the harder it would be to digitally compress samples from it. Mathematically, entropy is defined as the expected value of the negative log of the probability density/mass function:

$$H(\mathbf{Y}) = -\mathbb{E}[\log p(\mathbf{Y})] \tag{9}$$

Like mutual information estimation, there is a large body of literature on entropy estimation and many different approaches have been proposed [100], including those that form an estimate of the probability density function  $\hat{p}(\mathbf{y})$  and plug it into the definition of entropy and those that estimate entropy based on the similarity of samples from  $p(\mathbf{y})$  [101–103]. Both approaches, however, face difficulties in high dimensions.

There are multiple ways of decomposing mutual information into a difference of entropies. Our approach is based upon the decomposition:

$$I(\mathbf{X}; \mathbf{Y}) = H(\mathbf{Y}) - H(\mathbf{Y} | \mathbf{X}) \quad (10)$$

Here,  $H(\mathbf{Y})$  is the entropy of the noisy image distribution  $p(\mathbf{y})$ . Both variations in the object and measurement noise contribute to the randomness of measurements. We are interested in the information about the object, thus to quantify how much of these variations the measurements contain, we must subtract the entropy contributed by the noise,  $H(\mathbf{Y} | \mathbf{X})$ .

This decomposition is especially valuable for optical imaging because measurement noise typically acts independently at each pixel, greatly simplifying the calculation of the conditional entropy  $H(\mathbf{Y} | \mathbf{X})$ .

(A technical note: in optical systems, the outcomes of the random variables  $\mathbf{X}$  and  $\mathbf{Y}$  in our model are discrete, because they are 2D arrays of pixels, where each pixel takes on an intensity value that is an integer number of photons. However, for computational simplicity, we will approximate them as continuous random variables and use differential entropy instead of discrete entropy [72, 69]. These approximations break down at very low photon counts, less than  $\sim 20$  photons, so in this paper, we use only data with photon counts greater than this. A possible direction of future work is to extend our approach to work with discrete random variables, which would allow it to be applied to data with lower photon counts.)

We begin by describing the simpler of the two terms to estimate, the conditional entropy  $H(\mathbf{Y} | \mathbf{X})$ .

### S2.3 Estimating conditional entropy of measurement noise

The conditional entropy of noisy measurements given noiseless images can be written out in terms of expectations over the logarithm conditional probability of noisy measurements given a noiseless image  $p(\mathbf{y} | \mathbf{x})$ :

$$H(\mathbf{Y} | \mathbf{X}) = -\mathbb{E}_{\mathbf{X}, \mathbf{Y}} [\log p(\mathbf{Y} | \mathbf{X})] \quad (11)$$

By the Law of Total Expectation, this can be written as:

$$\mathbb{E}_{\mathbf{X}, \mathbf{Y}} [\log p(\mathbf{Y} | \mathbf{X})] = \mathbb{E}_{\mathbf{X}} [\mathbb{E}_{\mathbf{Y}} [\log p(\mathbf{Y} | \mathbf{X}) | \mathbf{X}]] \quad (12)$$

$$= \mathbb{E}_{\mathbf{X}} [\mathbb{E}_{\mathbf{Y}} [\log p(\mathbf{Y} | \mathbf{X})]] \quad (13)$$

$p(\mathbf{y} | \mathbf{x})$  embodies the various sources of noise in the detection process, including photon shot noise, detector read noise, etc. Here, we utilize established analytic models of detection noise in optical imaging [32]. Empirical results suggest that the true noise in systems deviates from these models in low-light conditions [104], but since our experiments are conducted in the high-light regime, we will assume that these models are accurate for the purposes of this paper. A possible direction for future work is to learn more accurate noise models from the data, as was done in [105].

Assuming we have access to a dataset of  $N$  samples from the distribution of noiseless images  $\{\mathbf{x}^{(1)}, \mathbf{x}^{(2)}, \dots, \mathbf{x}^{(N)}\}$ , the outer expectation can be estimated through Monte Carlo approximation:

$$-\mathbb{E}_{\mathbf{X}} [\mathbb{E}_{\mathbf{Y}} [\log p(\mathbf{Y} | \mathbf{X})]] \approx -\frac{1}{N} \sum_{i=1}^N \mathbb{E}_{\mathbf{Y}} [\log p(\mathbf{Y} | \mathbf{x}^{(i)})] \quad (14)$$

$$= -\frac{1}{N} \sum_{i=1}^N H(\mathbf{Y} | \mathbf{x}^{(i)}) \quad (15)$$

Here,  $H(\mathbf{Y} | \mathbf{x}^{(i)})$  is the conditional entropy of the distribution of noisy images given the  $i$ th noiseless image.

### S2.3.1 Conditionally independent noise at each pixel

$H(\mathbf{Y} | \mathbf{x}^{(i)})$  is a function of the noise introduced in the detection process, which is modeled by the probability distribution  $p(\mathbf{y} | \mathbf{x}^{(i)})$ . In optical imaging, common analytic noise models like additive Gaussian and Poisson shot noise typically assume that the noise at each pixel is conditionally independent of the noise at other pixels, given the true (noiseless) pixel value. When this is true,  $p(\mathbf{y} | \mathbf{x}^{(i)})$ , which is a joint distribution over all  $D$  pixels in the noisy measurement, can be simplified by factoring it into a product of scalar distributions for each pixel, where  $y_k$  and  $x_k^{(i)}$  are the intensity values at the  $k$ th pixel in the noisy measurement and the  $i$ th noiseless image, respectively:

$$\begin{aligned} p(\mathbf{y} | \mathbf{x}) &= p(y_1, y_2, \dots, y_D | x_1^{(i)}, x_2^{(i)}, \dots, x_D^{(i)}) \\ &= \prod_{k=1}^D p(y_k | x_k^{(i)}) \end{aligned}$$

This factorization simplifies the calculation of conditional entropy, because it is much easier to compute  $D$  scalar conditional entropies than a single joint conditional entropy over  $D$  variables. Mathematically, this simplification can be seen by plugging the factorized distribution into the definition of conditional entropy:

$$H(\mathbf{Y} | \mathbf{x}^{(i)}) = -\mathbb{E}_{\mathbf{Y}} \left[ \log \prod_{k=1}^D p(y_k | x_k^{(i)}) \right] \quad (16)$$

$$= -\mathbb{E}_{\mathbf{Y}} \left[ \sum_{k=1}^D \log p(y_k | x_k^{(i)}) \right] \quad (17)$$

$$= -\sum_{k=1}^D \mathbb{E}_{\mathbf{Y}} \left[ \log p(y_k | x_k^{(i)}) \right] \quad (18)$$

$$= \sum_{k=1}^D H(Y_k | x_k^{(i)}) \quad (19)$$

Here,  $H(Y_k | x_k^{(i)})$  is the conditional entropy of the  $k$ th pixel in the noisy image given the intensity of the  $k$ th pixel in the noiseless image.

This is a scalar quantity and can be calculated analytically for many common noise models. We will discuss two such models here: additive Gaussian noise and Poisson noise.

### S2.3.2 Conditional entropy with additive Gaussian noise

Additive Gaussian noise is a simple noise model often used in optical imaging, especially in low-light conditions where the read noise of the detector is the dominant source of noise. In this model, the noise at each pixel is drawn from a Gaussian distribution with mean zero and variance  $\sigma^2$ . Mathematically:

$$\begin{aligned} Y_k &= X_k + N_k \\ N_k &\sim \mathcal{N}(0, \sigma^2) \end{aligned}$$

The entropy of a (scalar) Gaussian distribution  $\mathcal{N}(\mu, \sigma)$  is [72]:

$$H(N_k) = \frac{1}{2} \log_2(2\pi e\sigma^2)$$

Since the noise is independent of the noiseless image, the conditional entropy of the noise at each pixel is the same, and the full conditional entropy (Equation 19) simplifies to:

$$H(\mathbf{Y} | \mathbf{x}^{(i)}) = \sum_{k=1}^D H(Y_k | x_k^{(i)}) \quad (20)$$

$$= \sum_{k=1}^D H(N_k) \quad (21)$$

$$= \frac{D}{2} \log_2(2\pi e \sigma^2) \quad (22)$$

Plugging this result into Equations 15 and 11 yields:

$$H(\mathbf{Y} | \mathbf{X}) = \frac{D}{2} \log_2(2\pi e \sigma^2) \quad (23)$$

To summarize, the conditional entropy of the noisy image given the noiseless image is a constant, independent of the intensity values of the noiseless images, and is equal to the number of pixels in the image times the entropy of the noise distribution at each pixel.

### S2.3.3 Conditional entropy with shot noise

Images with high photon counts are fundamentally limited by shot noise - randomness in photon arrival times due to the quantum nature of light. This shot noise follows a Poisson distribution with rate parameter equal to the expected number of photons at each pixel. When shot noise is the dominant source of noise, it can be accurately approximated by a Gaussian distribution with equal mean and variance [32].

Thus, the conditional entropy of the noise at pixel  $k$  for the  $i$ th noiseless image can be approximated with the entropy of a gaussian distribution:

$$H(Y_k | x_k^{(i)}) = \frac{1}{2} \log_2(2\pi e x_k^{(i)}) \quad (24)$$

Once again making use of the fact that the measurement noise at each pixel is independent of the noise at other pixels conditional on the intensity of the noiseless image at that pixel (Section S2.3.1), we can write the conditional entropy for noiseless image  $\mathbf{x}^{(i)}$  as:

$$H(\mathbf{Y} | \mathbf{x}^{(i)}) = \sum_{k=1}^D H(Y_k | x_k^{(i)}) \quad (25)$$

$$= \sum_{k=1}^D \frac{1}{2} \log_2(2\pi e x_k^{(i)}) \quad (26)$$

The full conditional entropy (Equation 19) simplifies to:

$$H(\mathbf{Y} | \mathbf{X}) \approx \frac{1}{N} \sum_{i=1}^N \sum_{k=1}^D \frac{1}{2} \log_2(2\pi e x_k^{(i)}) \quad (27)$$

To summarize, the conditional entropy under a Poisson noise model can be approximated as a sum of the log of the intensity values of the noiseless image at each pixel, averaged over  $N$  noiseless images. This approximation is accurate when the photon counts are high, and breaks down when the photon counts are low, and is discussed further in **Section S3.5**.

## S2.4 Estimating entropy of noisy images

The second term in the mutual information decomposition,  $H(\mathbf{Y})$ , presents a greater estimation challenge. Unlike the conditional entropy calculated in **Section S2.3**, the joint probability distribution  $p(\mathbf{y})$  cannot be factored into independent distributions for each pixel, as pixels throughout both noisy and noiseless images exhibit complex dependencies.

We estimate this entropy by computing an upper bound, an approach that has proven more accurate than alternative bounds in high-dimensional settings [43]. Our method fits a parametric model  $p_\theta(\mathbf{y})$  to the empirical distribution of noisy images using maximum likelihood estimation. The optimal parameters  $\hat{\theta}_{\text{MLE}}$  are found by minimizing the negative log likelihood of the observed data:

$$\hat{\theta}_{\text{MLE}} = \arg \min_{\theta} -\mathbb{E} [\log p_\theta(\mathbf{Y})] \quad (28)$$

This loss function,  $-\mathbb{E} [\log p_\theta(\mathbf{Y})]$ , is also known as the cross-entropy between the model distribution  $p_\theta(\mathbf{y})$  and the empirical distribution  $p(\mathbf{y})$ .

In practice, it is fit using a dataset of  $N$  samples from the empirical distribution  $p(\mathbf{y})$ :

$$\hat{\theta} = \arg \min_{\theta} -\frac{1}{N} \sum_{i=1}^N \log p_\theta(\mathbf{y}^{(i)}) \quad (29)$$

When the model distribution  $p_\theta(\mathbf{y})$  is identical to the empirical distribution  $p(\mathbf{y})$ , the data has been fit perfectly, and the value of the cross-entropy loss function is equal to the entropy of the noisy images,  $H(\mathbf{Y})$ .

$$-\mathbb{E} [\log p_\theta(\mathbf{Y})] = -\mathbb{E} [\log p(\mathbf{Y})] \quad (30)$$

$$= H(\mathbf{Y}) \quad (31)$$

In practice, the model will not be able to fit the true distribution exactly, and the average value of the loss function will be greater than the entropy of the noisy images. The gap between the entropy that we are interested in estimating and the cross-entropy loss function is given by the Kullback-Leibler divergence between the empirical distribution and the model distribution:

$$-\mathbb{E} [\log p_\theta(\mathbf{Y})] = H(\mathbf{Y}) + D_{KL}(p \parallel p_\theta) \quad (32)$$

The Kullback-Leibler divergence is a measure of the difference between two probability distributions. It is always non-negative and is zero only when the two distributions are identical. Thus, the cross-entropy loss function is an upper bound on the entropy of the noisy images. The better our model fits the data, the tighter this bound will be. Finding the right model that balances the accuracy of this bound with the computational cost of fitting the data is an important choice that is discussed further in **Section S3.2**.

In practice, the cross-entropy loss function is evaluated on separate test set of samples from the empirical distribution, to avoid overfitting to a subset of the data and generating a model that is overly optimistic about its performance.

This process is mathematically equivalent to data compression in information theory<sup>3</sup>. In data compression, the goal is to map each outcome to a bit string while minimizing the average string length. Optimal compression assigns shorter bit strings to more probable outcomes and longer ones to less probable outcomes. The achievable compression - measured by the average bit string length -

<sup>3</sup>Technically, this is only completely true when the model distribution is discrete, because continuous data cannot be losslessly compressed. For example, it would take an infinite number of bits on a computer to represent an arbitrary real number exactly. But the intuition remains the same.

has a fundamental lower bound equal to the entropy of the data distribution. Just as no compression scheme can achieve a shorter average bit length than that dictated by the true distribution’s entropy, no model we fit can achieve a lower entropy than the true distribution - any mismatch between our model and reality can only increase our entropy estimate.

## S2.5 Probabilistic models

In this section, we describe three probabilistic models  $p_\theta(\mathbf{y})$  used to estimate the entropy of noisy measurements via upper bounds, as described in **Section S2.4**. The models offer different tradeoffs between accuracy and computational efficiency.

The simplest model assumes stationary Gaussian statistics, providing fast estimation with minimal data requirements. A more complex full-covariance Gaussian model removes the stationarity assumption, offering improved accuracy while maintaining computational efficiency. The most sophisticated model, based on the PixelCNN neural network architecture, provides the tightest bounds but requires substantially more computation time and training data.

Other models could be used within this framework, provided they allow direct evaluation of likelihood functions. Recent neural network architectures such as transformers [76], normalizing flows [106], and diffusion models [107, 108] offer promising directions for future work.

While generative models are often evaluated by the visual quality of their samples, this metric does not necessarily correlate with cross-entropy performance [109] - though some state-of-the-art models can achieve both [110]. We selected PixelCNN for its demonstrated effectiveness in minimizing test set cross-entropy [47], combined with its relative simplicity and computational efficiency. However, the rapid advancement of generative models suggests that more efficient architectures providing tighter entropy bounds for a given computational efficiency are likely to emerge.

### S2.5.1 Full Gaussian process

The full Gaussian process model approximates the distribution of noisy images with a multivariate Gaussian distribution, which is specified by a mean vector  $\boldsymbol{\mu}$  and covariance matrix  $\boldsymbol{\Sigma}$ . The mean vector contains  $D$  parameters describing the average value at each pixel, while the covariance matrix requires  $\frac{D(D+1)}{2}$  parameters to capture all possible correlations between pixels.

We fit this model by directly estimating the mean and covariance from the data.

### S2.5.2 Stationary Gaussian process

To reduce model complexity and quantify performance over the full field of view with a single scalar quantity, we can make the simplifying assumption that images are stationary stochastic processes. This is the probabilistic analog of assuming constant optical resolution across the field of view [93].

A stationary stochastic process with distribution  $p(\mathbf{y})$  is one in which the joint distribution of any set of pixels is invariant to translations across the field of view. For a 1D process (i.e., a single row of pixels), this means that the joint distribution of pixels depends only on their relative locations, not absolute positions.

Mathematically, for any vector of pixels  $(y_1, y_2, \dots, y_D)$ , the joint distribution remains unchanged when all pixels are offset by a constant amount  $k$ :

$$p(y_1, y_2, \dots, y_D) = p(y_{1+k}, y_{2+k}, \dots, y_{D+k}) \quad (33)$$

This stationarity assumption constrains our Gaussian model in two ways. First, the mean vector must be constant across all pixels, reducing it from  $D$  parameters to just one. Second, the covariance between any two pixels must depend only on their relative positions. For a 1D process, this makes the covariance matrix Toeplitz (constant along diagonals). For 2D processes, it becomes a doubly Toeplitz matrix: blocks of Toeplitz matrices arranged in a Toeplitz pattern (**Fig. S10**). This structure reduces the number of covariance parameters from  $\frac{D(D+1)}{2}$  to just  $D$ .

Stationary processes have another useful property: a constant entropy per pixel, called the entropy rate [72] (explained in Figure 8 of [87]). This rate can be defined in two equivalent ways:

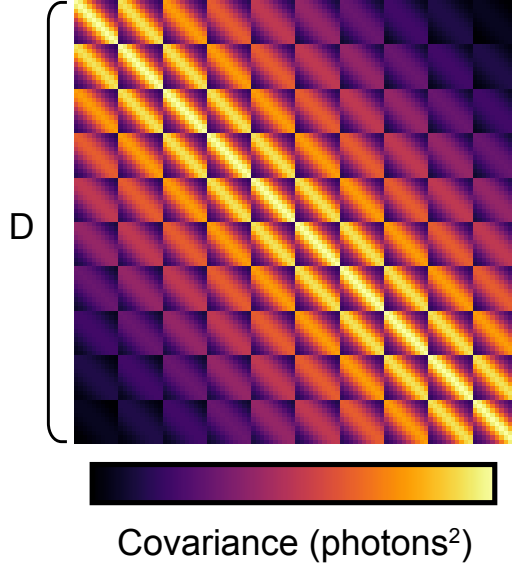


Figure S10: **The doubly Toeplitz  $D \times D$  covariance matrix of a stationary 2D Gaussian process.**

$$\lim_{D \rightarrow \infty} \frac{1}{D} H(y_1, y_2, \dots, y_D) = \lim_{D \rightarrow \infty} H(y_D | y_1, y_2, \dots, y_{D-1}) \quad (34)$$

The second formulation reveals why the entropy rate decreases with  $D$ : as we observe more pixels, it is easier to predict the value at the next pixel, because more context about neighboring pixels is available.

### S2.5.3 PixelCNN

Our most flexible model is the PixelCNN [45–47], which uses neural networks to capture complex pixel dependencies through an autoregressive approach.

Autoregressive models factorize a joint distribution into a product of conditional distributions:

$$p(\mathbf{y}) = \prod_{k=1}^D p(y_k | y_1, y_2, \dots, y_{k-1}) \quad (35)$$

$$= p(y_1)p(y_2 | y_1)p(y_3 | y_1, y_2) \dots p(y_M | y_1, y_2, \dots, y_{D-1}) \quad (36)$$

This factorization does not require specific assumptions about the joint distribution, so in theory it can be applied to any distribution. Creating the full model requires  $D$  conditional distribution models, each taking between 1 and  $D - 1$  previous pixel values as input and outputting a 1D probability distribution for the next pixel. While this could be implemented with  $D$  separate models, PixelCNN uses masked convolutions in a single neural network to model all conditionals simultaneously, dramatically reducing computational complexity.

Following previous work [45, 46], our architecture uses a series of masked convolutions to maintain the autoregressive ordering, producing a conditional probability distribution at each pixel.

However, we make one crucial modification: instead of the standard softmax output layer, we use a mixture of Gaussians parameterized by the network (a mixture density network [111]). This strategy is capable in theory of approximating any conditional probability distribution, in the same way that a neural network is capable of approximating any function [112]. This modification is essential for estimating entropy in our framework, because it means the output distributions will be continuous probability densities, instead of discrete probability mass functions. Since our noise models  $p(\mathbf{y} | \mathbf{x})$

are continuous (Gaussian), our entropy estimates for  $H(\mathbf{Y})$  must also use continuous distributions to allow proper subtraction of the conditional entropy  $H(\mathbf{Y} | \mathbf{X})$ .

## S2.6 Sampling and likelihood evaluation

While our models' primary purpose is likelihood evaluation for entropy estimation (**Section S2.4**), generating samples provides valuable insight into model behavior. For simple models like the stationary Gaussian process, sample quality correlates well with likelihood accuracy, making visual inspection a useful diagnostic tool. However, this correlation breaks down for more complex models like PixelCNN [109], though samples remain helpful for understanding model behavior.

Both PixelCNN and stationary Gaussian models are trained on fixed-size patches ( $\sqrt{D} \times \sqrt{D}$  pixels), limiting their ability to capture longer-range dependencies. While increasing patch size allows modeling of longer-range correlations, both models can handle arbitrary-sized images despite their fixed patch size. This is possible because their stationary nature allows them to be factored into conditional distributions, enabling evaluation over larger images by sliding the fixed-extent window (though this iterative process is substantially slower than processing native-sized patches). For a 1-dimensional model with  $D$  pixels, this factorization means the joint distribution can be written as:

$$p(\mathbf{y}) = \prod_{k=1}^D p(y_k | y_1, y_2, \dots, y_{k-1}) \quad (37)$$

$$= p(y_1)p(y_2 | y_1)p(y_3 | y_1, y_2) \dots p(y_D | y_1, y_2, \dots, y_{D-1}) \quad (38)$$

Taking the log likelihood turns this product into a sum:

$$\log p(\mathbf{y}) = \sum_{k=1}^D \log p(y_k | y_1, y_2, \dots, y_{k-1}) \quad (39)$$

$$= \log p(y_1) + \log p(y_2 | y_1) + \log p(y_3 | y_1, y_2) + \dots + \log p(y_D | y_1, y_2, \dots, y_{D-1}) \quad (40)$$

Computing the likelihood over an image larger than the length  $D$  model the pixel was trained on can be accomplished by adding additional terms to this sum. For example, computing the log likelihood of an  $D + 1$  length image would require adding an additional term to the sum of the log likelihood of the  $D + 1$  pixel conditioned on the previous  $D - 1$  pixels (the maximum extent of the model) that preceded it:

$$\log p(\mathbf{y}) = \left( \sum_{k=1}^D \log p(y_k | y_1, y_2, \dots, y_{k-1}) \right) + \log p(y_{D+1} | y_2, y_3, \dots, y_D) \quad (41)$$

Details of the likelihood computations for PixelCNNs are described in [45]. For stationary Gaussian processes, there is a closed form solution for finding the mean  $\mu_D$  and variance  $\sigma_D^2$  of a 1-dimensional Gaussian distribution conditioned on  $D - 1$  previous values. This involves decomposing the covariance matrix into a top left  $(D - 1) \times (D - 1)$  block  $\Sigma_{1,1}$ , a top right  $(D - 1) \times 1$  column vector  $\Sigma_{1,2}$ , and a bottom left  $1 \times (D - 1)$  row vector  $\Sigma_{2,1}$ :

$$\Sigma = \begin{bmatrix} \Sigma_{1,1} & \Sigma_{1,2} \\ \Sigma_{2,1} & \sigma_M^2 \end{bmatrix} \quad (42)$$

Given  $D - 1$  previous values  $\mathbf{y}_{D-1}$ , the mean and variance of the  $D$ th value can be computed as:

$$\mu_D = \mu + \Sigma_{2,1} \Sigma_{1,1}^{-1} (\mathbf{y}_{D-1} - \mu) \quad (43)$$

$$\sigma_D^2 = \sigma^2 - \Sigma_{2,1} \Sigma_{1,1}^{-1} \Sigma_{1,2} \quad (44)$$

The likelihood the the  $D$ th pixel can then be evaluated using the probability density function of a 1D Gaussian distribution with mean  $\mu_D$  and variance  $\sigma_D^2$ .

Similarly, sampling images larger than the patch size on which the models were trained can be accomplished by iteratively sampling each pixel conditioned on the previous  $D - 1$  pixels.

### S2.7 Accounting for encoder uncertainty

Calibration presents a fundamental challenge in applying information estimation to experimental imaging systems (**Section S1.5.1**). While the basic approach treats object properties and detection noise as the primary sources of measurement randomness, real systems introduce additional variations through optical imperfections, mechanical instabilities, and illumination fluctuations. These variations can inflate information estimates by misattributing system randomness to object information.

The most effective approach to this challenge is to minimize system variations through careful engineering: building mechanically stable optical systems, using temperature control to reduce thermal drift, and implementing precise electronic control of components like illumination sources. However, some level of system variation often remains unavoidable in practice.

When measurements contain information about both the object and the system itself, the estimation of mutual information can be modified by considering the encoder state. Rather than estimating the full entropy of noisy measurements  $H(\mathbf{Y})$ , the conditional entropy  $H(\mathbf{Y}|\mathbf{E})$  accounts for system variation, where  $\mathbf{E}$  represents the encoder state. The conditional entropy estimate  $H(\mathbf{Y}|\mathbf{X})$  remains unchanged, but  $H(\mathbf{Y})$  includes randomness from three sources:

- Object variations
- System variations
- Measurement noise

Conditioning on the encoder state  $\mathbf{E}$  eliminates the contribution of system variations, isolating the object and noise entropy components.

In practice, conditioning can be accomplished by providing additional encoder state information like field position or calibration images to the entropy model during training. Flexible models like PixelCNN can readily accept such conditional data [46]. This reduces the entropy estimate by eliminating variations predictable from the system state.

We leave developing such conditional entropy estimation to future work. However, we can already observe the impact of encoder uncertainty in practical systems - in **Section S4.1**, we demonstrate how it affects information estimates in LED array microscopy.

## S3 Estimating information: Experiments

Having developed a framework for estimating information in imaging systems, we now validate its performance through experiments on both simulated and real-world data.

### S3.1 Fitting stationary Gaussian processes

Fitting a stationary Gaussian process to  $N$  image patches ( $\sqrt{D} \times \sqrt{D}$  pixels) requires estimating both the mean vector  $\boldsymbol{\mu}$  and covariance matrix  $\boldsymbol{\Sigma}$ . While the mean is easily computed by averaging all pixels across patches, estimating the covariance matrix presents a greater challenge.

As described in **Section S2.5.2**, the covariance matrix must be both symmetric positive definite and doubly Toeplitz, with repeated patterns along diagonal blocks. Our initial approach was to compute the sample covariance matrix from vectorized patches and enforce the Toeplitz structure by averaging along diagonals and blocks. However, this averaging operation sometimes produced matrices with negative eigenvalues, violating the positive definite requirement and creating invalid covariance matrices.

To address this issue, we initially tried enforcing a minimum positive value (floor) for the eigenvalues. However, this approach proved problematic for two reasons. First, modifying eigenvalues disrupted

the doubly Toeplitz structure, violating the stationarity requirement. More critically, since the likelihood evaluation used for entropy estimation is highly sensitive to small eigenvalues in the covariance matrix, the arbitrary choice of eigenvalue floor significantly impacted our entropy bounds. This sensitivity varied across datasets, making the approach unreliable for comparing different imaging systems.

To overcome these limitations, we developed an iterative optimization procedure that improves the covariance matrix fit while maintaining required properties. Given  $N$  image patches (each  $\sqrt{D} \times \sqrt{D}$  pixels) vectorized to length- $D$  vectors  $\mathbf{y}^{(i)}$ , we minimize the negative log likelihood of a multivariate Gaussian distribution  $\mathcal{N}(\cdot; \hat{\boldsymbol{\mu}}, \boldsymbol{\Sigma})$ :

$$\hat{\boldsymbol{\Sigma}} = \arg \min_{\boldsymbol{\Sigma}} - \sum_{i=1}^N \log \mathcal{N}(\mathbf{y}^{(i)}; \hat{\boldsymbol{\mu}}, \boldsymbol{\Sigma}) \quad (45)$$

Where  $\hat{\boldsymbol{\mu}}$  is the fixed mean vector estimated from the data as described above.

We solved this optimization problem using proximal gradient descent with momentum, initializing from the direct sample estimate. Each iteration consisted of three steps:

- Computing the eigendecomposition of the covariance matrix and applying gradients to eigenvalues while keeping eigenvectors fixed
- Applying a proximal operator that enforced the doubly Toeplitz structure by averaging along diagonals and blocks
- Enforcing the minimum eigenvalue constraint

The procedure was regularized through early stopping: optimization terminated when the loss hadn't decreased for a fixed number of iterations, with parameters from the lowest-loss iteration selected as the final estimate.

Empirically, we found that the optimization procedure was unstable and prone to divergence. This seemed to be because the likelihood was very sensitive to small eigenvalues of the covariance, which tended to produce extremely large gradients for these eigenvalues. To account for this, we implemented gradient clipping to limit the magnitude of the gradients for the eigenvalues.

The likelihood of a probability distribution can be very sensitive to small changes in parameters because the Euclidean distance between parameter vectors does not always accurately reflect the dissimilarity of the resulting distributions (as described in section 2.3 of [113]). In theory this can be corrected by multiplying the gradient by the inverse of the Fisher information matrix to reorient it from the steepest direction in Euclidean space to the steepest direction in Riemannian space, which accounts for the natural geometry of the parameters. However, in practice we found this to be expensive to compute without obvious performance benefits over gradient clipping.

**Figure S11** shows the results when fitting stationary Gaussian processes to images from the BSCCM dataset [65]. The direct estimate contained several negative eigenvalues, which were then set to an arbitrary eigenvalue floor. The optimization procedure was able to correct these negative eigenvalues, and produced robust results for a variety of settings of the eigenvalue floor parameter (provided it was smaller than the true minimum eigenvalue) (**Fig. S11b**). As a consequence of the small, incorrect eigenvalues in the direct estimate, samples produced from the model that were larger than the patch size on which they were trained (**Sec. S2.6**) exhibited numerical instability that created large oscillation in the samples. In contrast, samples from the optimized model were stable and did not exhibit this oscillation (**Fig. S11b**). The optimization quickly converged in a few iterations (**Fig. S11c**), taking  $\sim 3$  seconds to complete on an NVIDIA GeForce RTX 3090 GPU. Comparing estimates of a non-stationary Gaussian process, the direct estimate stationary Gaussian process, and the optimized stationary Gaussian process showed that the optimized stationary Gaussian process produced more robust results in terms of its eigenvalue distribution using smaller datasets (**Fig. S11d**).

### S3.2 Comparing stationary Gaussian process and PixelCNN estimates

We evaluated model performance through two approaches: negative log likelihood on held-out test data and qualitative assessment of model-generated samples.

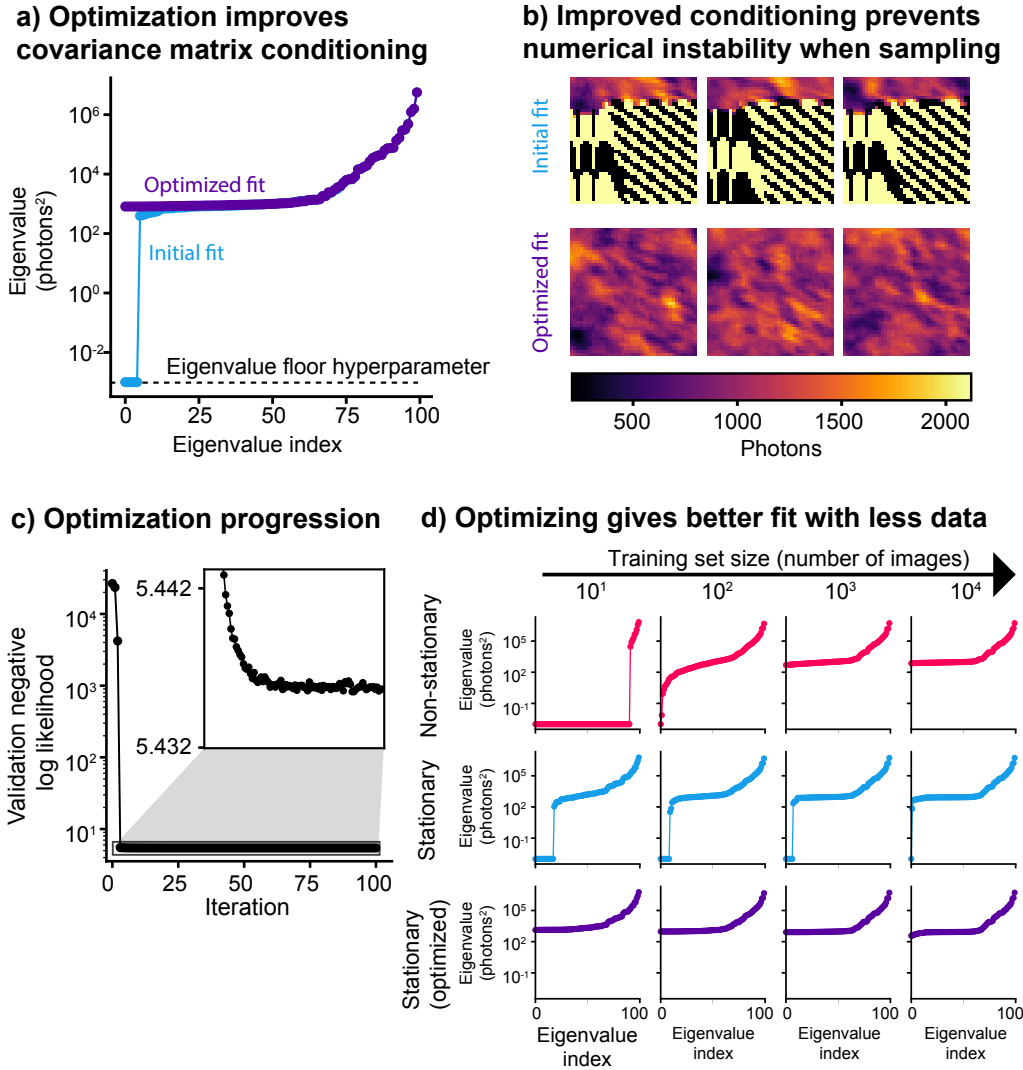
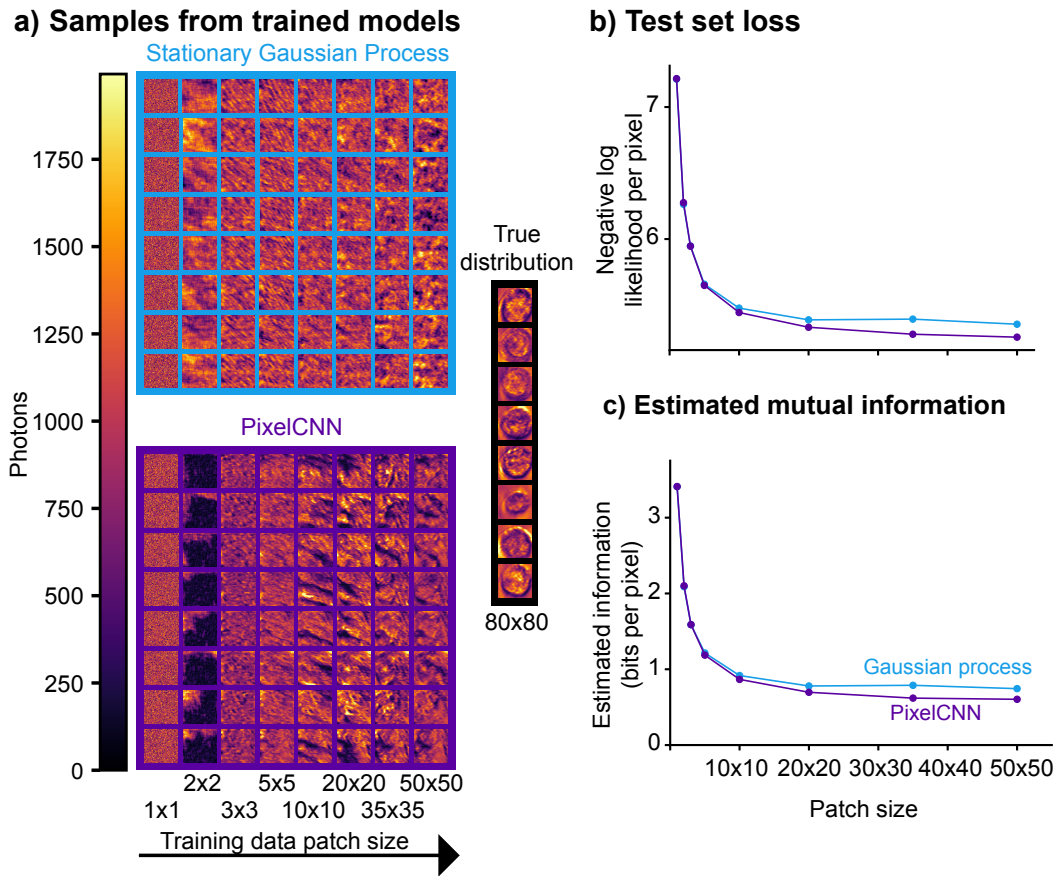


Figure S11: **Fitting Gaussian Process models.** **a)** Eigenvalues of the covariance matrix before and after optimization, indicating improved conditioning post-optimization. The conditioning of the covariance matrix of non-optimized fits is highly dependent on the choice of the eigenvalue floor hyperparameter. **b)** Comparison of numerical stability during sampling pre- and post-optimization, demonstrating that optimization prevents the instability that manifests in the initial fit. **c)** The optimization process takes only a few iterations to converge and shows an extremely large improvement in the negative log likelihood of the data for poor initial fits. **d)** Efficacy of the optimization across varying training set sizes, illustrating that optimized fitting requires fewer images to achieve a comparable or better fit than the non-optimized approach and outperforms the full Gaussian model when training data is limited.

An important consideration for both models is the choice of training patch size. Larger patches capture longer-range dependencies and improve per-pixel likelihood, but require more training data and computational resources. We therefore sought to determine the minimum patch size that would provide reliable entropy estimates while maintaining computational efficiency.

**Figure S12** shows samples produced when fitting models to patches of different sizes. As expected, larger patch sizes were able to capture more complex statistical relationships between pixels (**Fig. S12a**), decrease the per-pixel loss (**Fig. S12b**), and more tightly upper bound the entropy of the noisy images (**Fig. S12c**). The gains in performance were minimal beyond a patch size of  $35 \times 35$  pixels for the Gaussian model, while the PixelCNN was able to continue to produce a more accurate estimate as patch size increased further. This is presumably due to its much greater flexibility in modeling complex dependencies between pixels. However, the magnitude of the gains was small relative to the differences between the estimates of mutual information for different contrast modalities (**Fig. S13**) for these experimental images.



**Figure S12: The effects of patch size on model fit.** **a)** Samples generated from a Stationary Gaussian Process and PixelCNN, alongside samples from the true distribution. As the patch size increases, the models are able to capture more long range dependencies between pixels, and **b)** achieve lower negative log likelihood per pixel and thus **c)** a tighter upper bound on mutual information.

When comparing the samples produced by the two models when fit to images with different illumination patterns on the LED array, both the stationary Gaussian process and PixelCNN models were able to capture statistical patterns to each type of contrast modality (**Fig. S14a**). Samples from the trained models appear to show that the stationary Gaussian model was able to learn the statistical patterns of the texture of the images of objects under different illumination, while the PixelCNN model additionally learned higher order structures like the edges of cells.

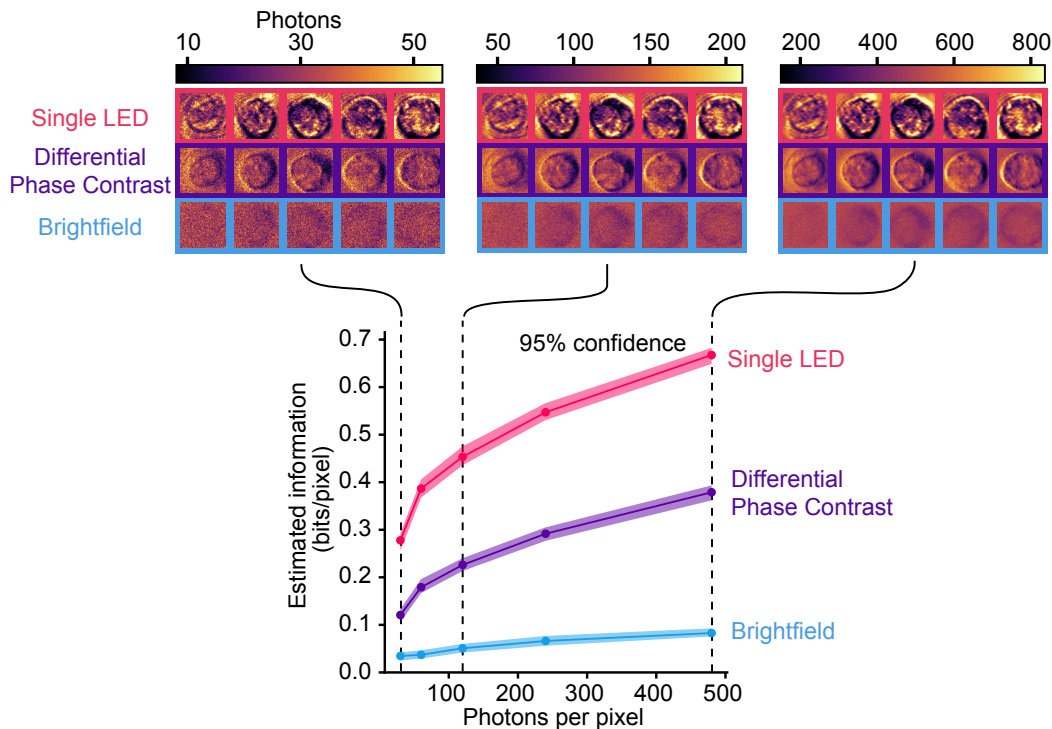


Figure S13: **Mutual information and photon count.** As the average number of photons per pixel increases, the signal-to-noise ratio and mutual information both increase. (Top) Example images of three different contrast modalities at varying photon counts. (Bottom) The mutual information per pixel for each contrast modality as a function of photon count.

### S3.3 Failures of stationary Gaussian estimates on highly non-Gaussian data

The comparable performance of stationary Gaussian and PixelCNN models on the BSCCM dataset (single cells under coded-angle illumination) likely reflects the near-Gaussian statistics of these images. However, this similarity cannot be assumed for all datasets. This becomes evident when testing on the MNIST handwritten digits dataset [114] (GNU General Public License), where image statistics deviate significantly from Gaussian distributions due to the nearly bimodal nature of pixel values (predominantly 0 or 1).

To demonstrate this, we take the MNIST dataset and simulate a minimal optical encoder (i.e. a single lens) by convolving the images with a Gaussian point spread function. We then add Poisson noise to simulate noisy measurements, and fit both the stationary Gaussian process and PixelCNN models to the data. Sampling from the fitted models shows that the PixelCNN model can produce images that appear similar to true measurements, unlike the Gaussian process model (**Fig. S15a**).

This occurs because the best approximating stationary Gaussian fit is very dissimilar to the true distribution of the measurements. This can be seen by looking at the histograms of image pixels of the true data and samples from the models, pooled across all many images (**Fig. S15b**). The true data and PixelCNN samples have similar histograms, while the histogram from the stationary Gaussian process samples has a very different shape. As a result of this poor fit, the upper bound given by the mutual information estimator is quite loose for the stationary Gaussian model compared to the PixelCNN model (**Fig. S15c**).

These findings demonstrate that a stationary Gaussian process model is inadequate to capture certain image distributions. Since the tightness of the upper bound in our information estimation procedure depends on accurately fitting the distribution of noisy measurements, this suggests that achieving a tight upper bound/accurate estimate in many cases may require more flexible probabilistic models, like the PixelCNN.

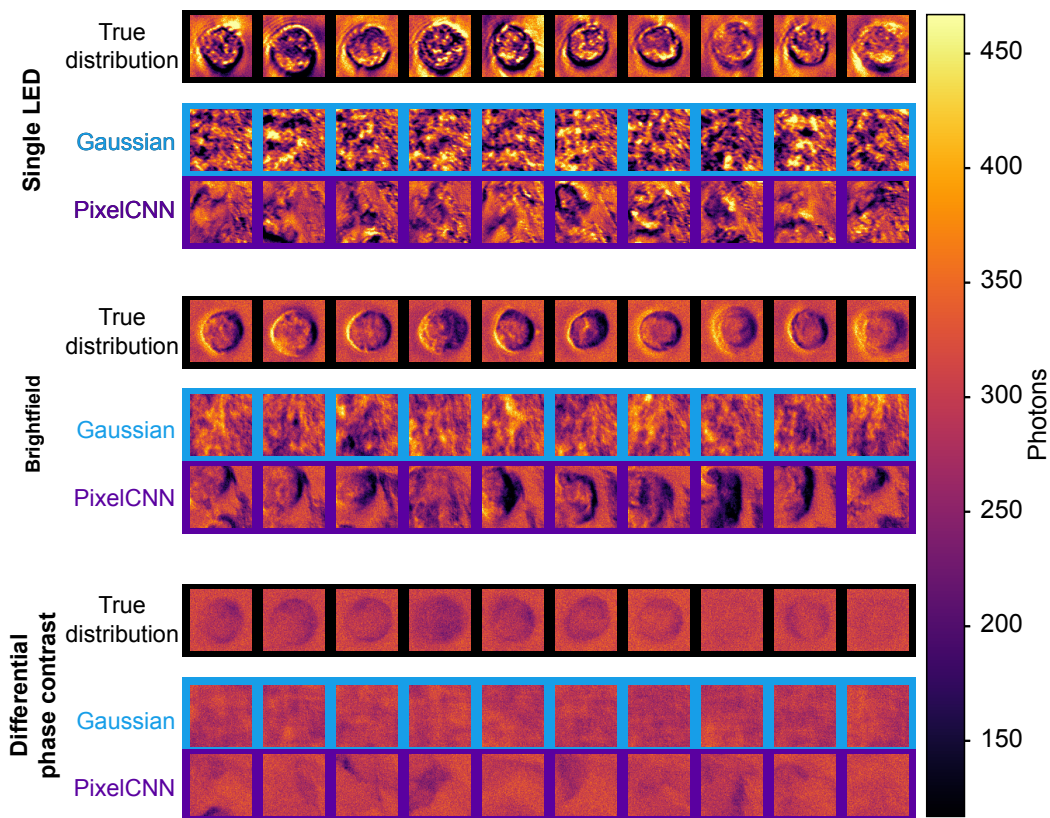


Figure S14: **Model samples for different contrast modalities.** Samples from the stationary Gaussian process and PixelCNN models for Brightfield, Differential phase contrast, and Single LED illumination.

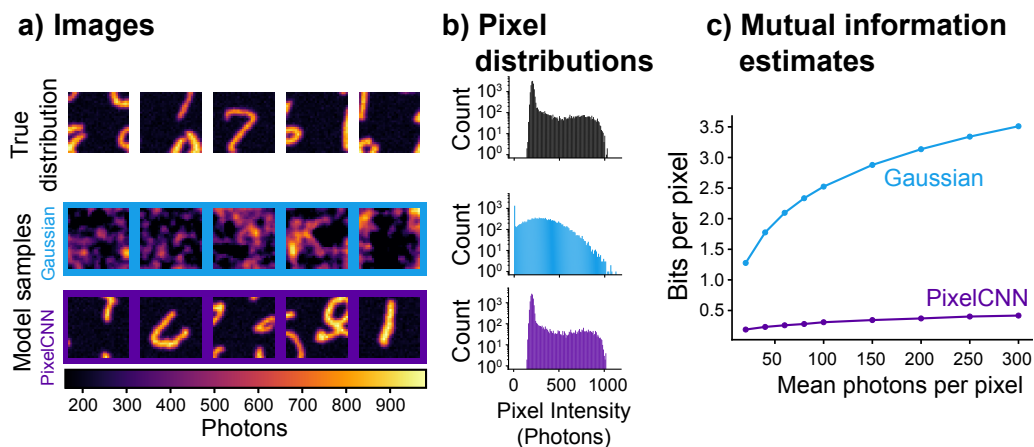


Figure S15: **PixelCNN can fit non-Gaussian data better than stationary Gaussian processes.** **a)** Samples from the stationary Gaussian process and PixelCNN models for MNIST digits. The Gaussian process samples do not resemble the true distribution, indicating a poor fit. **b)** Histograms of pixel values for the true distributions and samples from the two models indicate that the marginal distribution of pixels is non-Gaussian, which the PixelCNN, unlike the Gaussian model, is able to fit. **c)** As a result of the poor fit, the upper bound on mutual information given by the Gaussian process estimator is much looser than the PixelCNN estimator.

An important and desirable property of an estimator is its consistency: whether it converges to the true value of the parameter being estimated given enough data. This has practical implications for determining how much data is needed to achieve a desired accuracy level.

To evaluate our estimators on high-dimensional data, we first tested them on samples from a known distribution: a stationary multivariate Gaussian with independent additive Gaussian noise at each pixel (Equation 23). In this case,  $H(\mathbf{Y} | \mathbf{X})$  is constant, and  $H(\mathbf{Y})$  can be computed analytically by adding the noise variance to the diagonal of the data covariance matrix and analytically calculating the entropy of the resultant multivariate Gaussian distribution.

**Figure S16a** shows that all three estimators converge to the true value given sufficient samples, with the stationary Gaussian estimator being most accurate for a given sample size. This is expected since the test data perfectly matches the model’s assumptions.

To evaluate performance on real microscopy data, we tested two different patch sampling strategies. When patches were taken from fixed locations across different images (**Fig. S16b**), the full Gaussian model outperformed the stationary model. This suggests the presence of location-specific image statistics that violate the stationarity assumption. However, when patches were sampled from random locations (**Fig. S16c**), the stationary Gaussian model performed better than the full Gaussian model, as the random sampling effectively enforces stationarity in the data distribution.

The PixelCNN model demonstrated good performance across all scenarios due to its flexibility, though the stationary Gaussian model was able to outperform it for small training dataset sizes.

### S3.4 Model training times

The three models offer different tradeoffs between accuracy and computational efficiency. As shown in **Figure S17**, training times on a typical  $20 \times 20$  pixel patch dataset vary significantly: the full Gaussian process is fastest ( $\sim 0.1s$ ), while the stationary Gaussian process requires longer ( $\sim 10s$ ) due to its iterative optimization procedure. The PixelCNN is most computationally intensive ( $\sim 100s$ ), reflecting the cost of its greater modeling flexibility.

### S3.5 Conditional entropy estimates on noisy data

The accuracy of mutual information estimates depends on both  $H(\mathbf{Y})$  and  $H(\mathbf{Y} | \mathbf{X})$ . For additive Gaussian noise, the conditional entropy is independent of the noiseless images and can be computed analytically (**Sec. S2.3.2**). However, for signal-dependent Poisson noise (**Sec. S2.3.3**), estimation becomes more challenging.

Using simulated data derived from the BSCCM [65] dataset, we first examined the consistency of our conditional entropy estimator. We created ground truth data by applying a  $3 \times 3$  median filter to produce noiseless images, then added simulated shot noise. Our estimator rapidly converges to the true value (**Fig. S18a**), with variations on the order of  $10^{-2}$  differential entropy per pixel - significantly smaller than the variations in  $H(\mathbf{Y})$  estimation.

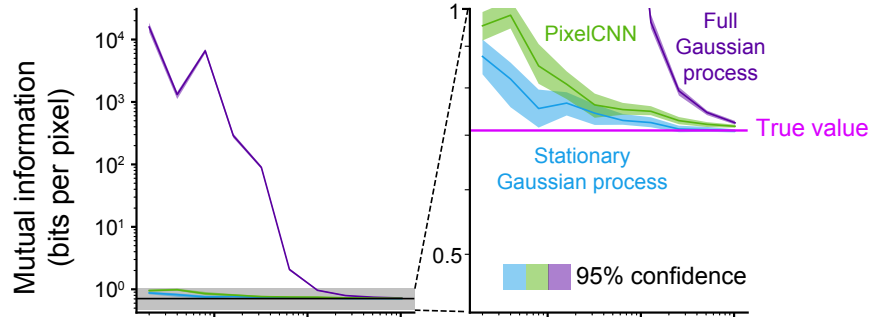
In experimental settings, noiseless images are typically unavailable. Instead, we must estimate conditional entropy directly from noisy measurements, replacing noiseless pixel values in Equation 27 with noisy ones:

$$H(\mathbf{Y} | \mathbf{X}) \approx \frac{1}{N} \sum_{i=1}^N \sum_{k=1}^D \frac{1}{2} \log_2(2\pi e x_k^{(i)}) \tag{46}$$

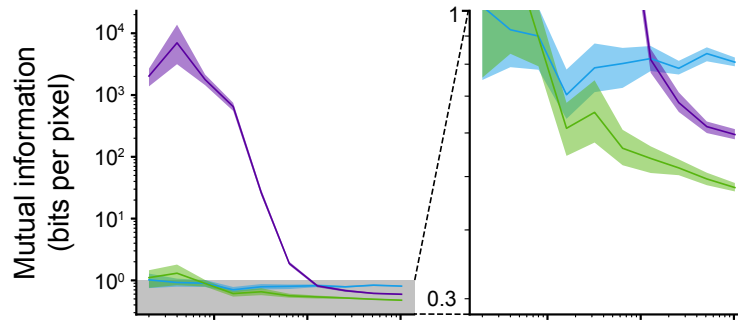
$$\approx \frac{1}{N} \sum_{i=1}^N \sum_{k=1}^D \frac{1}{2} \log_2(2\pi e y_k^{(i)}) \tag{47}$$

To evaluate this approximation, we compared mutual information estimates using either noiseless or noisy images for conditional entropy estimation across different imaging modalities (**Fig. S18b**). The estimates show good agreement except at very low photon counts (below  $\sim 40$  photons per pixel). At these low counts, using noisy measurements leads to slight overestimation of mutual information due to underestimation of conditional entropy. While this bias could potentially be corrected, other

**a) Stationary Gaussian data**



**b) Real data (fixed location patches)**



**c) Real data (random location patches)**

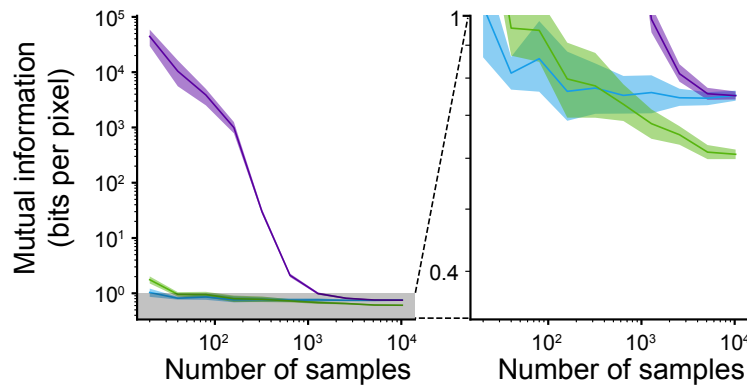


Figure S16: **Estimator consistency.** **a)** On simulated data from a stationary Gaussian process, all estimators converge to the true mutual information value, with the stationary Gaussian being most accurate per sample. **b)** With fixed-location patches from real data, the full Gaussian model outperforms the stationary model due to location-specific image statistics. **c)** With random-location patches, the stationary model performs better as sampling enforces effective stationarity in the data distribution.

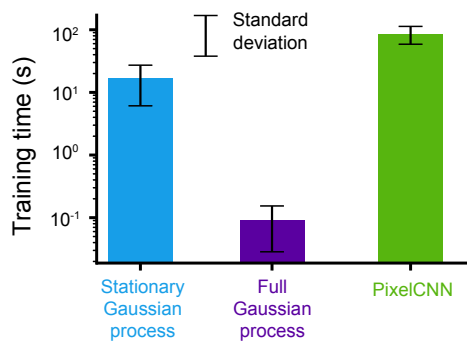
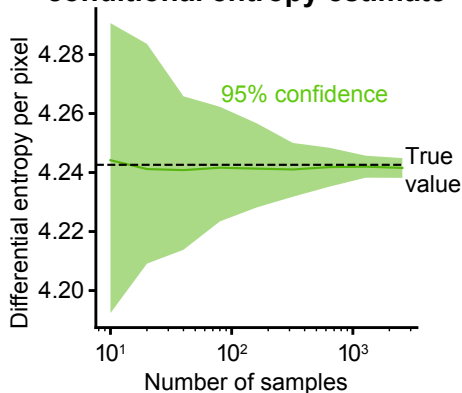


Figure S17: **Model training times.** Comparison of training times for each model type on a typical dataset of  $20 \times 20$  pixel patches on an NVIDIA RTX A6000 GPU. Error bars show standard deviation across multiple training runs.

approximations in our framework (such as the Gaussian approximation to Poisson noise (Sec. S2.3.3)) also break down in this regime.

### a) Consistency of shot noise conditional entropy estimate



### b) Estimating from noisy samples

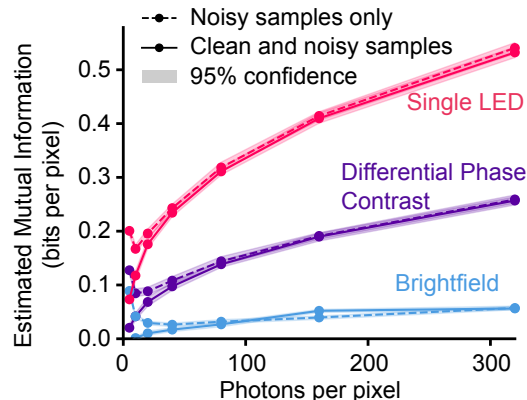


Figure S18: **Conditional entropy estimation.** **a)** The estimator converges rapidly to the true conditional entropy for shot noise as sample size increases, with variations much smaller than those seen in entropy estimation (Figure S16). **b)** Comparison of mutual information estimates using noisy versus noiseless measurements for conditional entropy estimation across different imaging modalities, showing good agreement except at very low photon counts.

## S3.6 Comparing analytic and upper bound entropy estimates

For Gaussian models, we can estimate entropy in two ways: by computing an upper bound using test set negative log likelihood, or by analytically calculating the entropy of the fitted model. While the upper bound approach provides theoretical guarantees, the relationship between analytic estimates and true entropy is less clear.

We compared both approaches empirically across three imaging modalities in the BSCCM dataset using three estimators: analytic stationary Gaussian entropy, stationary Gaussian upper bound, and PixelCNN upper bound (Fig. S19). While we lack theoretical guarantees for the analytic stationary Gaussian estimates, they consistently track close to the PixelCNN bounds, which represent our best estimate of the true entropy. The differences between estimation methods remain small compared to the variations across imaging modalities and photon counts. This close agreement

is particularly relevant for our IDEAL framework (See **Information-Driven Encoder Analysis Learning (IDEAL)**), where we use the analytic form in our optimization loss function.

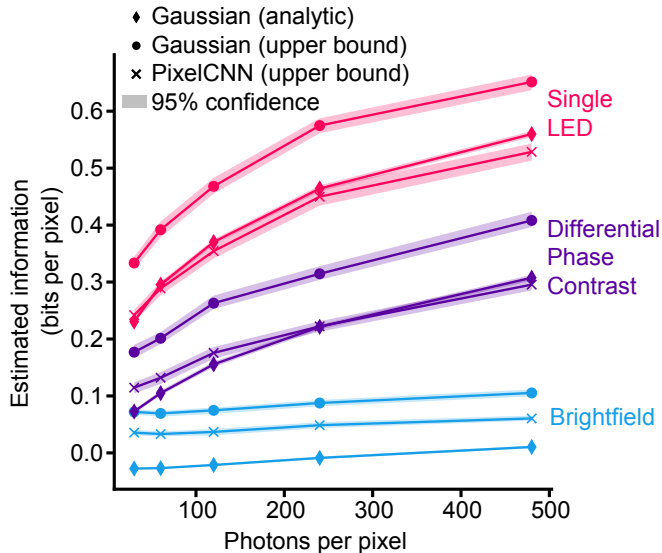


Figure S19: **Comparison of entropy estimation methods.** Three approaches to entropy estimation - analytic stationary Gaussian, stationary Gaussian upper bound, and PixelCNN upper bound - across different illumination patterns and photon counts. The error bars for the upper bound methods (Gaussian and PixelCNN) are computed by bootstrapping both the marginal and conditional entropy estimates from the test set. For the analytic estimates, multiple Gaussian models were fit to bootstrapped versions of the full dataset to estimate  $H(\mathbf{Y})$ , while  $H(\mathbf{Y} | \mathbf{X})$  was bootstrapped as before. While the relationship between analytic estimates and true entropy lacks theoretical guarantees, they remain close to our best estimates across conditions.

## S4 Additional decoder experiments

### S4.1 Experimental evidence of encoder uncertainty effects

To demonstrate how encoder uncertainty (**Sec. S1.5.1**) affects information estimates in practice, we examined measurements from an LED array microscope using different illumination patterns. We estimated the mutual information in empty image patches containing no biological sample, allowing us to directly measure information content arising purely from system variations rather than objects of interest.

As shown in **Figure S21**, single-LED illumination exhibited higher background information content than either differential phase contrast or brightfield illumination. This aligns with the theoretical prediction that more sensitive imaging methods encode more information about both objects and system imperfections. The measurements reveal a fundamental tradeoff: illumination patterns that capture more object information also capture more system-derived information, potentially inflating information estimates.

These results highlight the practical importance of developing the conditional entropy estimation methods described in **Section S2.7** to separate object information from system variations on highly sensitive systems with uncontrolled and unmodeled sources of randomness. Without such corrections, information estimates may tend to overestimate the true information content for highly sensitive encoders or those with large amounts of uncontrollable system randomness.

### S4.2 Task-specific information in classification

For tasks like deconvolution that aim to recover full image structure, any additional information helps reduce reconstruction error. However, simpler tasks like classification may only need specific features.

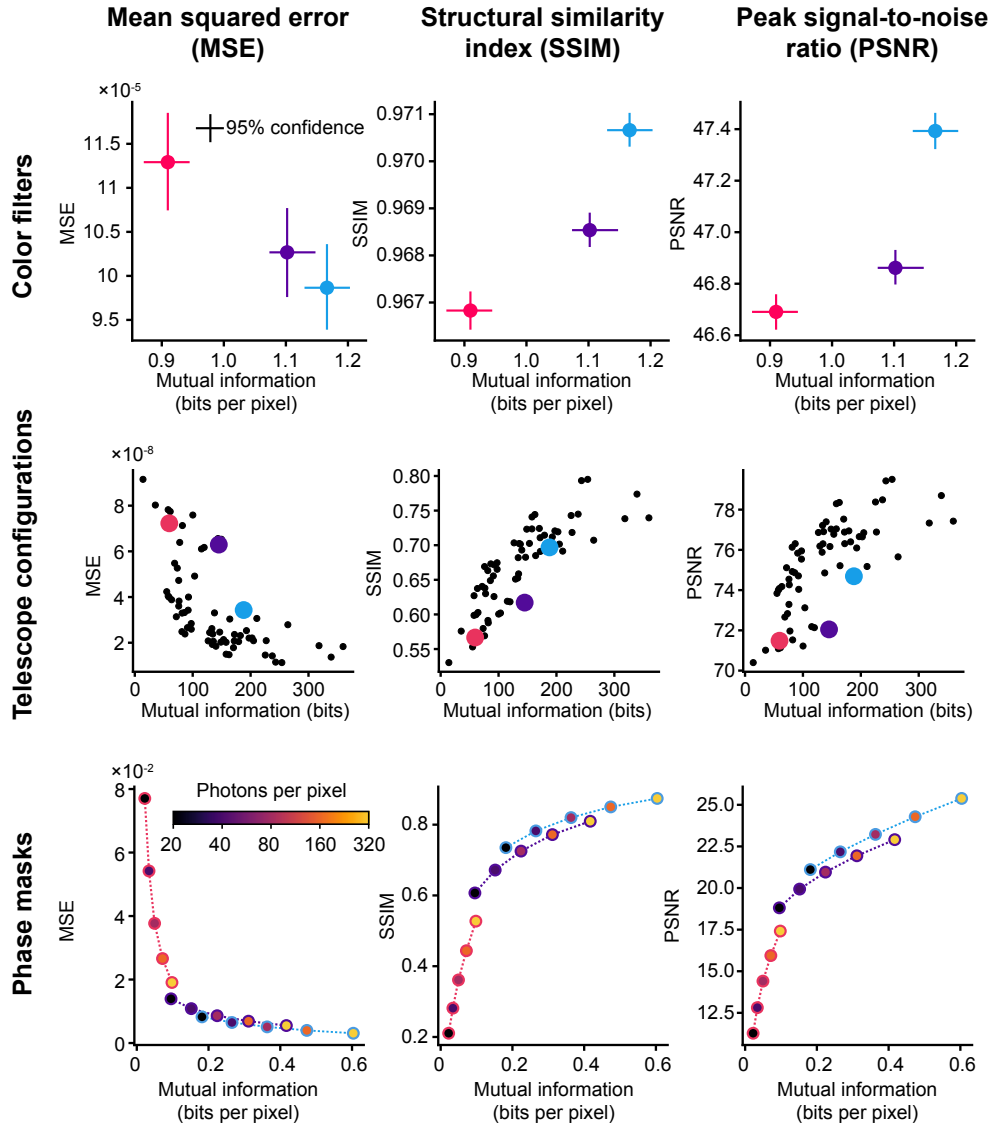


Figure S20: **Performance across multiple metrics correlates with information estimates.** Comparison of mean squared error (MSE), structural similarity index (SSIM), and peak signal-to-noise ratio (PSNR) for the color photography, radio telescope, and lensless imaging systems shown in **Fig. 2a-c**. For the radio telescope configurations (middle row), colored dots correspond to the three example configurations shown in the main text, while black dots show additional tested configurations. Each metric shows consistent correlation with information estimates across different imaging modalities.

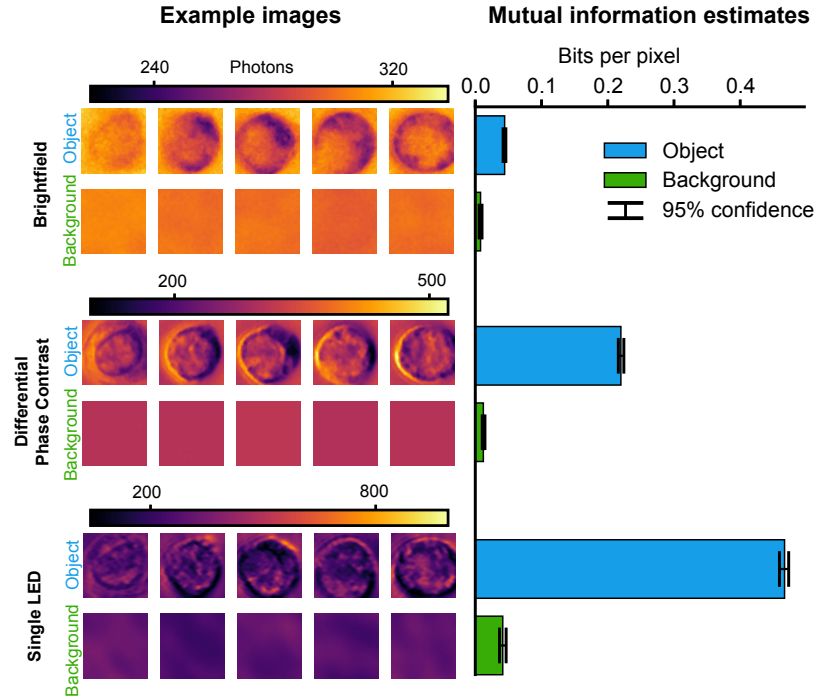


Figure S21: **The effect of encoder uncertainty on information estimates.** By computing mutual information estimates on empty image patches with no objects in them, the information about the system present in the measurements can be estimated. This can be seen by comparing Single LED, Differential Phase Contrast, and Brightfield illumination patterns on an LED array microscope, and estimating the mutual information between noiseless image and noisy measurement with and without an object. Encoders that capture more information about the object also capture more information about the system.

We tested this using a 10-class object classification task on our lensless imaging measurements (**Fig. S22**). Unlike deconvolution, where higher information consistently predicted better performance across all encoders, classification accuracy varied significantly between encoders with similar total information content.

This disparity arises because classification requires only the information that distinguishes between classes. Most of the measured information ( $\sim 307$  bits for our  $32 \times 32$  pixel images at  $0.3$  bits/pixel) captures within-class variations irrelevant to the classification task, which requires at most  $\log_2 10 \approx 3.32$  bits. Different encoders may preserve this class-discriminative information more or less effectively, even while capturing similar total information.

## S5 Comparison to other frameworks

Mathematical assumptions about object structure underlie several established frameworks for imaging system design. Like our approach, estimation theory [115] and compressed sensing [116] offer ways to design imaging systems without requiring ground truth data or human-interpretable measurements. Estimation theory assumes objects can be described by a few key parameters and uses the Cramér-Rao lower bound [117, 86] to optimize system performance. Compressed sensing assumes objects are sparse in some basis, enabling efficient measurement with theoretical guarantees.

These frameworks take a deductive approach: they start with specific assumptions about objects, encoders, and decoders to prove performance guarantees. While powerful, this approach has inherent

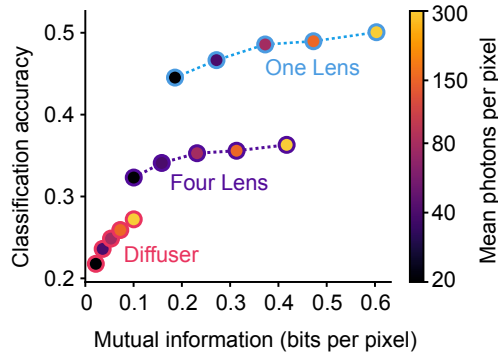


Figure S22: **Classification accuracy vs. information content in lensless imaging.** Unlike deconvolution (Fig. 2c), classification performance does not show a consistent relationship with total information content across different optical designs, suggesting the importance of preserving task-specific information. Points represent median over five classification networks with different random weight initializations.

limitations. The theoretical guarantees only apply when all assumptions are met—a condition that can be difficult or impossible to verify in practice. Moreover, these frameworks often focus on best or worst-case scenarios for individual objects, which may not reflect the average performance over a range of objects.

Our information-based framework can complement these approaches. Like estimation theory and compressed sensing, it can be used deductively to derive theoretical limits when specific assumptions hold, as demonstrated in our analysis of two-point resolution (See **Probabilistic two-point resolution**). However, it also offers a unique advantage: the ability to work inductively from experimental data. By estimating information content directly from measurements, our approach automatically adapts to the actual properties of objects being imaged, without requiring explicit mathematical models of the imaging process. The only assumption we rely on is a noise model, which itself could be learned from data rather than specified analytically.

This flexibility enables novel capabilities: comparing different imaging modalities, identifying subtle performance tradeoffs, and understanding complex relationships between encoding physics and measurement quality. By learning from data rather than relying on predetermined assumptions, our framework can evaluate and optimize a broader range of imaging systems.

Detailed comparisons between our approach and these established frameworks are provided in **Sections S5.1** and **S5.2**.

### S5.1 Estimation theory and the Cramér-Rao lower bound

Estimation theory provides tools for optimizing imaging systems by minimizing measurement uncertainty. Its central tool, the Cramér-Rao lower bound [115], defines the minimum achievable error when estimating object parameters from noisy measurements. This bound enables systematic comparison of different optical designs by identifying those with the lowest theoretical error.

While both estimation theory and our information-based framework aim to reduce measurement uncertainty (**Sec. S5.1.4**), our approach offers several key advantages:

- **Data-driven adaptation:** Rather than requiring explicit mathematical models, our framework learns system behavior directly from measurements, automatically capturing complex optical effects.
- **Task flexibility:** Estimation theory requires expressing imaging goals as parameter estimation problems (e.g. modeling point source localization in terms of position coordinates). Many practical imaging tasks lack such tractable parameterizations.
- **Minimal assumptions:** We require only a noise model, which can be measured empirically, reducing the risk of model misspecification.

- **Decoder generality:** The Cramér-Rao bound traditionally applies only to unbiased estimators, which are rarely optimal in practice. While extensions to biased estimators exist, they introduce additional complexity without clear benefits (**Sec. S5.1.3**). Our framework places no restrictions on decoder type.

Our framework’s flexibility allows it to operate in both deductive and inductive modes. When analytical object models are available, it can provide theoretical guarantees similar to estimation theory. However, it can also learn directly from experimental data when such models are impractical. This dual capability enables our framework to handle a wider range of imaging scenarios, from well-modeled systems to those with complex, difficult-to-model behavior.

### S5.1.1 Background: The Cramér-Rao lower bound in imaging

The Cramér-Rao lower bound has guided the design of numerous imaging systems. Its most successful application has been in fluorescence microscopy, where it has helped optimize point spread functions for localizing single molecules [118, 117, 119–121, 86, 122]. Similar approaches have proven valuable in phase microscopy [123] and wavefront sensing [124].

At its core, the Cramér-Rao bound provides a fundamental limit on measurement precision. Consider measuring a single parameter  $\theta$  (such as a particle’s position) from noisy data  $X$ . The measurement process is described by a probability distribution  $p(x; \theta)$ , which captures both the imaging physics and measurement noise. For instance, in fluorescence microscopy, this distribution might describe how likely different intensity patterns are when imaging a point source at position  $\theta$ .

The bound states that any unbiased estimator  $\hat{\theta}(X)$  (one that gets the right answer on average) must have a mean squared error greater than or equal to the inverse of the Fisher information:

$$\mathbb{E} \left[ (\hat{\theta}(X) - \theta)^2 \right] \geq \frac{1}{I_F(\theta)} \quad (48)$$

where  $I_F(\theta)$  is the Fisher information of  $\theta$ , defined as:

$$I_F(\theta) = E \left[ (\nabla_{\theta} \log p(x; \theta))^2 \right]$$

For many common distributions, the Fisher information behaves like the inverse of the distribution’s variance. Intuitively, this means that noisier measurements (higher variance) make it harder to accurately estimate the true value of  $\theta$ .

This mathematical framework has direct practical applications. In single-molecule microscopy, for example, the Cramér-Rao bound quantifies how precisely a point source’s position can be determined from an image. By calculating this bound for different optical designs (such as various point spread functions), researchers can systematically identify and optimize systems that enable more precise localization.

It’s important to note that Fisher information, despite sharing the word “information,” is distinct from Shannon’s mutual information and entropy used elsewhere in this work. While both concepts quantify aspects of measurement uncertainty, they arose from different fields—estimation theory and information theory—and were developed independently. Though theoretical connections exist between them in certain cases [115], they serve different purposes in analysis and design.

### S5.1.2 Cramér-Rao lower bound-based design and its limitations

The approach of designing physical systems based on the Cramér-Rao lower bound has inherent limitations that prevent its application outside of a narrow set of applications in which the decoding problem is limited to estimation of one or a few parameters. Furthermore, even when it can be applied, it requires developing a complete mathematical model of the physics of image formation with respect to the parameter of interest. These limitations have thus far prevented its application outside a narrow range of problems, which include estimation of the position or mass of a single particle [118, 117, 119–121, 86, 125], or estimating a single optical aberration such as defocus [124]. Below, we discuss these limitations in more detail.

**The difficulties of creating parametric models** Creating parametric models is essential for calculating the Cramér-Rao lower bound, but it becomes challenging when dealing with high-dimensional objects due to the difficulty of parameterizing objects in a way that captures important aspects of decoders, while also retaining computational tractability.

The computation of the Cramér-Rao lower bound requires calculation of Fisher Information, which in turn requires a parametric model of the data distribution, denoted as  $p(x; \theta)$ . This parametric model stipulates the probability of a specific outcome  $x$ , given a certain parameter  $\theta$ .

In certain scenarios,  $p(x; \theta)$  can be analytically defined. For example, in the point localization problem,  $\theta$  denotes a 3-dimensional vector that marks the XYZ location of a point emitter (the bold type indicates it is a vector of parameters), and  $x$  denotes the intensity of a specific pixel. Given known equations for the system's noise characteristics and image formation mechanism,  $p(x; \theta)$  can be precisely defined. This can be used to compute Fisher Information and the Cramér-Rao lower bound for a single pixel, and the process can be repeated over each pixel  $x$  to get an averaged bound.

However, creating a straightforward equation-based model for imaging most types of objects is usually very challenging due to the difficulty and increasing complexity of adding additional parameters. Most objects being imaged lack the simplicity of a single point emitter, which can be fully described by its XYZ location. One potential way to circumvent this issue is a more general purpose parameterization of the object in which it is represented by a discrete array of pixel values [123]. However, unbiased estimators are rarely used on high-dimensional estimation problems like this. Furthermore, the Cramér-Rao lower bound is in terms of mean squared error, which, when applied to an array of pixels, generally does not effectively capture semantically meaningful information about objects [126].

**Generalizing from the simple case** In light of the the difficulties of extending this approach to objects with high-dimensional parameterizations, another possibility is to design imaging systems on simple classes of objects with the hope that they will generalize to other classes of objects. Taking such an approach requires making additional assumptions with unknown effects on results. Our experiments in minimal 1-Dimensional simulations show that the object-dependence of imaging systems can be readily demonstrated (**Sec. S1.3**), which may in part explain why empirical solutions to particle localization problems deviate from theoretical predictions [122].

**Unbiased estimators are usually suboptimal** In addition to the practical difficulties of formulating complex parametric models and computing corresponding Cramér-Rao lower bounds, there remains the limitation that the (standard) Cramér-Rao lower bound quantifies the minimum mean squared error only of unbiased estimators. While constraining an estimator to be unbiased is arguably a reasonable choice for simple, low-dimensional parameters like the location of a single point in 3D space, most estimators used in practice are in fact biased [127, 128] and state-of-the-art methods for solving image processing tasks almost exclusively use biased estimators to achieve high performance.

The bias-variance tradeoff [129] provides a useful perspective: biased estimators, while possessing higher bias, can have lower variance, thereby potentially reducing overall error. Thus, with bias, estimators with better error than the standard Cramér-Rao lower bound can be achieved. A classic illustration of this principle is the James-Stein estimator [130], which improves the estimation of multiple parameters simultaneously by shrinking individual estimates towards a common mean. It is based on the counterintuitive principle that, under certain conditions, an estimator that partially pools the data towards a central value can produce overall estimates that are closer to the true values than those obtained by estimating each parameter independently, especially when dealing with small sample sizes or high-dimensional data. It results in lower average error than the unbiased sample mean approach for Gaussian random variables when the number of dimensions is  $\geq 3$ .

Furthermore, the advantages of biased estimators are clear on empirical problems, particularly high-dimensional ones. State of the art methods on image-to-image estimation problems like denoising and deconvolution are usually achieved using deep neural networks [131] or with iterative optimization procedures that use regularization to bias the estimates towards certain classes of solutions.

Since computational imaging relies heavily on biased estimators for most image processing tasks, designing systems focused solely on minimizing the error of unbiased estimators, or assessing empirical performance based on this criterion, can provide only a narrow range of guarantees, and it is unclear if the conclusions reached by these guarantees can be generalized to a broader range of

applications. This raises the question of what additional theoretic tools can be used to address this more general case.

### S5.1.3 The challenges of generalizing estimation-theoretic design

This section explores alternative approaches to estimation theory, focusing on the use of biased estimators and Bayesian Cramér-Rao lower bounds to address the limitations of the Cramér-Rao lower bound.

**The biased Cramér-Rao lower bound** Though the (standard) Cramér-Rao lower bound only pertains to unbiased estimators, there are variants and related inequalities that can be applied more broadly.

The first is the biased version of the Cramér-Rao lower bound:

$$\mathbb{E} \left[ (\hat{\theta}(X) - \theta)^2 \right] \geq \frac{(1 + \nabla_{\theta} b(\theta))^2}{I_F(\theta)} + b(\theta)^2$$

Where  $b(\theta)$  is the bias of the estimator as a function of  $\theta$ :

$$b(\theta) = \mathbb{E} \left[ \hat{\theta} \right] - \theta$$

While this form may appear promising, it is in practice challenging for similar reasons to those described in section S5.1.2. Computing the gradient of the expectation of the estimator in high dimensions is a challenging statistical problem in its own right, and this process would need to be repeated for each value of  $\theta$ , necessitating another high-dimensional integration. Furthermore, this bound is not universal—it changes depending on the bias of the estimator in question. This makes it more difficult to determine the best performance of an ideal theoretical estimator, and thus more difficult to determine how close a real estimator come to achieving that performance.

**The Bayesian Cramér-Rao lower bound (van Trees inequality)** One way of addressing the limitations of the (standard) Cramér-Rao lower bound for unbiased estimators and its biased estimator variant can be found by generalizing the estimation problem to consider not just a single value of the parameter  $\theta$ , but instead consider it to also be random (the upper case  $\Theta$  is used to denote the corresponding random variable).

Like the standard Cramér-Rao lower bound, the van Trees inequality (also known as the Bayesian Cramér-Rao lower bound) [132, 127] provides a lower bound on the squared error that can be achieved in a parameter estimation problem. Mathematically:

$$\mathbb{E} \left[ (\hat{\theta}(X) - \Theta)^2 \right] \geq \frac{1}{\mathbb{E} [I_F(\Theta)] + J(\Theta)} \quad (49)$$

Compared to the standard Cramér-Rao lower bound (Equation 48), this inequality makes two important changes. First, the Fisher information of a particular parameter value  $\theta$  has been replaced with a probability-weighted average over all possible values of  $\theta$ . Second, there is an additional term  $J(\Theta)$ , defined as:

$$J(\Theta) = \mathbb{E} \left[ (\nabla p(\Theta))^2 \right] \quad (50)$$

where  $p(\cdot)$  is the probability of a particular value of  $\Theta$ . This can be approximately understood as quantifying how concentrated the distribution of the random variable  $\Theta$  is. The more concentrated the distribution of the parameter  $\Theta$  is, the more precisely it can be estimated from noisy measurements. Biasing estimates towards more probable values of  $\Theta$  enables estimation error to be lowered on average.

This inequality formalizes an important intuition: The theoretical limit of the average error with which a parameter of interest can be estimated (such as some property of an object being imaged) is dependent upon the distribution of that parameter. Changing the distribution of the parameter can change the theoretical limits of performance, as well as the the form of optimal estimators.

#### S5.1.4 Connections between estimation and information theory

Originally, information-theoretic quantities like entropy and mutual information were developed for noise-affected message transmission. However, these tools have significant theoretical links to estimations of the precision of noise-corrupted random variables. Though these connections are mostly known only for simpler analytical cases such as Gaussian random variables, they nonetheless provide insights into the relationships between these fields [115]. Here we highlight some of these connections.

An important insight is that where these connections are recognized, designing imaging systems using either estimation or information measures tends to have similar objectives. However, estimation measures have inherent limitations in their applicability, as previously discussed. In contrast, information theory tools don't share these restrictions, positioning them as potentially universal tools for designing physical imaging systems across a variety of applications. Several known inequalities capture the known relationships between these findings and goals of information and estimation theory.

Much of estimation theory centers on limits defined in terms of mean squared error of signals. While mean squared error has many appealing properties, its shortcomings, particularly in the context of quantifying the perceptual and semantic quality of images are readily apparent [126]. This has, for example, motivated work on alternative ways of quantifying error [133, 134].

**Efrosimovich inequality** In contrast, rate distortion theory, a branch of information theory, can be used to understand the fundamental limits and behavior of a wide variety of loss functions. The connection from the lower bounds used in estimation theory and information theory can be readily seen in the Efrosimovich inequality [135], which generalizes the van Trees inequality (Equation 49) from providing a bound on only mean squared error to providing a bound on a more general way of quantifying uncertainty, the entropy of a parameter  $\theta$  given a noisy measurement  $X$ :

$$\frac{1}{2\pi e} e^{2h(\Theta|X)} \geq \frac{1}{\mathbb{E}[I_F(\Theta)] + J(\Theta)}$$

Here,  $h(\Theta | X)$  is the differential entropy of a parameter given data  $X$ . This inequality can be used to derive bounds on loss functions other than mean squared error in terms of information-theoretic quantities [128, 136].

**I-MMSE formula** Another known relationship with particular relevance to this work is known as the I-MMSE formula (short for Information - minimum mean squared error), which states that [137, 115]:

$$I(X; Y) = I(X; \sqrt{s}X + N) = \frac{1}{2} \int_0^s \text{mmse}(X | \gamma X + N) d\gamma$$

In this equation,  $X$  is a signal of interest, and  $Y = \sqrt{s}X + N$  is a noisy measurement of that signal, created by adding independent Gaussian noise  $N$  to the original signal such that the resultant signal-to-noise ratio is  $\sqrt{s}$ .  $\text{mmse}(\cdot)$  is the minimum mean squared error of estimating  $X$  given  $Y$  (i.e. the Bayesian Cramér-Rao lower bound shown in Equation 49). From this formula, the mutual information  $I(X; Y)$  is equal to the minimum mean squared error of the optimal estimator, averaged over all achievable signal-to-noise ratios.

This formula shows that mutual information quantifies the same operational idea as the (Bayesian) Cramér-Rao lower bound in the case of additive Gaussian noise, which strongly suggests that the quantities may serve similar purposes under more general noise models. This relationship has been leveraged to develop task-specific information estimators [23].

This relationship can be visualized in the signal coordinate representation, which provides further intuition as to why these quantities are closely related. **Figure S23** shows the distributions of noisy measurements for 6 different signals with a measurement system that imparts additive Gaussian noise. Since mutual information is operationally defined as the number of signals that can be reliably distinguished in the presence of noise, decreasing the maximum signal-to-noise ratio lowers the mutual information. Simultaneously from the estimation theory perspective, it impedes the ability to

estimate the original signal from a noisy measurement of it, because it increases the ambiguity as to which input signal gave rise to the measurement.

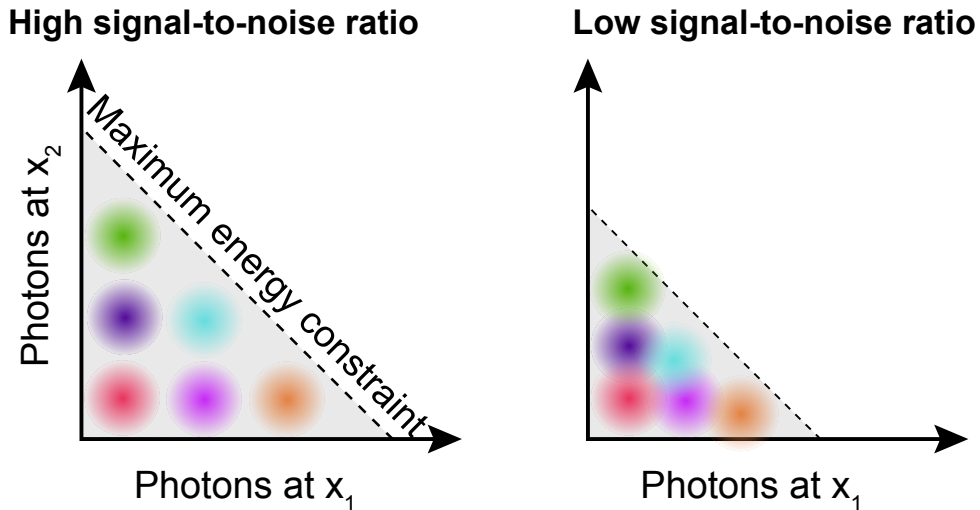


Figure S23: **Visualizing the connection between information and estimation.** Shown are noisy measurements of 6 distinct signals with high and low signal-to-noise ratios. With less noise, the signals remain more distinguishable, increasing mutual information. Simultaneously, lower noise reduces uncertainty in inferring the true signal, improving estimability.

This theoretical connection, combined with the developments in the present work that enable estimation of mutual information across many types of imaging systems provides a means of generalizing the successes of estimation-theoretic design criteria to a wide variety of imaging systems, without the requirements for detailed, system-specific mathematical modeling.

## S5.2 Compressed Sensing: Assumptions and Limitations

Compressed sensing theory showed that certain signals can be accurately reconstructed from fewer measurements than traditionally thought possible. While conventional sampling theory (Nyquist) requires sampling at twice the highest signal frequency, compressed sensing demonstrates that sparse signals—those with few nonzero components in some basis—can be recovered from fewer measurements.

In its original formulation, the framework relies on specific assumptions:

- **Signal sparsity:** Most signal components must be zero in some basis
- **Incoherence:** The measurements of the signal should *not* be sparse. The degree of incoherence between the measurement matrix and the sparsity basis gauges the level to which this requirement is met.
- **Gaussian noise:** Measurement noise must be normally distributed and signal-independent
- **Specific reconstruction algorithms:** Recovery requires optimization methods with provable guarantees

When these assumptions hold, compressed sensing approaches theoretical performance limits [138]. However, real-world imaging often violates these assumptions. Natural objects rarely exhibit perfect sparsity, and measurement noise may not be Gaussian. Studies have shown that compressed sensing strategies become suboptimal when objects don't match the assumed structure [31, 30].

Recent work has shown that incorporating additional object knowledge can improve upon basic compressed sensing. When signals can be generated by passing low-dimensional vectors through

nonlinear models, reconstruction accuracy can improve by an order of magnitude compared to traditional compressed sensing approaches [139–141].

More broadly, probabilistic models offer a framework for describing signal structure beyond sparsity. These models enable analysis of average-case performance and can incorporate various forms of prior knowledge about signals [142, 143]. Theoretical work has shown how measurement limits depend fundamentally on the complexity of the objects being measured [144], and how probabilistic approaches can achieve optimal performance for specific signal classes [145, 146].

## S6 Methods

### S6.1 Model training

Memory, computational, and data constraints often made it impractical to estimate information from full images. We therefore randomly sampled fixed-size patches from across the images for training.

**Full Gaussian model** The full (non-stationary) Gaussian model estimates a complete covariance matrix directly from vectorized image data without assuming stationarity. The mean vector is computed as the average across all training samples. The covariance matrix is estimated using the empirical covariance of the centered data. To ensure numerical stability and prevent degenerate solutions, we enforce positive definiteness by applying an eigenvalue floor - any eigenvalues below this threshold (typically  $10^{-3}$ ) are set to the floor value. If numerical issues persist, the floor is automatically increased until the covariance matrix becomes positive definite. This model offers greater flexibility than the stationary version but requires more training data and computation due to the larger number of parameters. For discrete-valued data, small uniform noise is added during training to prevent infinite likelihoods.

**Stationary Gaussian process model** The stationary Gaussian process model enforces translation invariance through a doubly Toeplitz structure in the covariance matrix. The model is initialized by computing the empirical covariance matrix from vectorized image patches and averaging along diagonals and block diagonals to impose the Toeplitz constraint. The mean is estimated as the average pixel value across all patches. We then refine these estimates through an optimization procedure that maximizes the data likelihood. The optimization uses a parameterization based on eigendecomposition, where only the eigenvalues are updated while keeping the eigenvectors fixed. We employ stochastic gradient descent with momentum and gradient clipping to prevent numerical instability. After each gradient step, a proximal operator ensures the eigenvalues remain above a minimum floor value (typically  $10^{-3}$ ) to maintain positive definiteness. The optimization typically runs for 60 epochs with early stopping based on validation likelihood, using batch sizes of 12 images and a learning rate of 100. During both training and evaluation, small uniform noise is added to discrete-valued data to enable proper likelihood computation with the continuous model. The stationary assumption significantly reduces the number of parameters compared to the full Gaussian model, enabling more efficient training and better generalization with limited data.

**PixelCNN model** The images were modeled using a PixelCNN architecture adapted from prior work [45, 46]. The model consists of vertical and horizontal masked convolution layers arranged in a stack, enabling modeling of the conditional distribution of each pixel given the previous pixels in raster scan order. The network includes seven gated masked convolution layers with alternating dilation rates (1,2,1,4,1,2,1) to increase the receptive field while maintaining computational efficiency. Each gated layer combines information from vertical and horizontal stacks through masked convolutions followed by a gating mechanism using tanh and sigmoid activations.

We modified the original categorical output distribution to instead use a Gaussian mixture density [111] with 40 components at each pixel. The mixture parameters (means, standard deviations, and mixing weights) were computed through separate dense layers. The Gaussian means were initialized randomly uniformly between the training image minimum and maximum values and clipped to this range during inference. The standard deviations were computed as the softplus output of a dense layer, clipped to be between 1 and the training set standard deviation to avoid degenerate solutions.

During training, small uniform noise was added to the discrete-valued images to account for modeling them with a continuous distribution. The noise prevents the likelihoods from going to infinity and overfitting to the exact training values. Input images were normalized by subtracting the mean and dividing by the standard deviation of the training set. The model was trained using the Adam optimizer with a learning rate of 0.01 on image patches, with early stopping based on validation likelihood to prevent overfitting. All models were implemented in JAX/Flax for efficient training on GPUs.

## S6.2 Confidence intervals

Our framework supports estimation of confidence intervals through bootstrapping to quantify uncertainty from finite test set size. For a specified confidence level (e.g., 90%), we repeatedly resample the test set with replacement and recompute both the marginal entropy (using the trained model) and conditional entropy. The mutual information is computed for all combinations of these resampled estimates. The confidence interval is then determined by taking appropriate percentiles of these bootstrap estimates - for example, the 5th and 95th percentiles for a 90% confidence interval. This approach captures uncertainty in both the marginal and conditional entropy estimates.

## S6.3 Sample generation

Images are generated using ancestral sampling, where pixels are drawn sequentially in raster scan order (left to right, top to bottom). For each new pixel, its value is sampled from a probability distribution conditioned on all previously generated pixels within its local neighborhood. For the Gaussian models, this is a Gaussian distribution whose parameters are computed using the Schur complement of the covariance matrix. For PixelCNN, this is a mixture of Gaussians whose parameters are computed by the neural network. To ensure physical plausibility in imaging applications, generated values can optionally be constrained to be non-negative by clipping negative values to zero. While slower than parallel generation methods, ancestral sampling maintains the local statistical dependencies captured by the models while enabling generation of arbitrarily large images.

## S6.4 Generation of synthetic experimental noise

Experimental data was simulated to have been collected with fewer photons by adding simulated photon shot noise. However, since the experimental data already contains some shot noise, it is necessary to determine how noisy the images already are, and then only add additional noise as needed.

To simulate a lower photon count, each pixel with photon count  $p$  was multiplied by a fraction  $f$  to reduce the photon count to  $fp$ . Assuming the dominant source of noise in the original image is photon shot noise, the variance of the noise in the original image is approximately  $p$ , and the variance in the reduced photon count image is approximately  $f^2p$ . The desired variance of the reduced photon count image is equal to its mean,  $fp$ . Since the sum of two independent Gaussian random variables with variances  $a$  and  $b$  is a Gaussian random variable with variance  $a + b$ , we can add noise to the reduced photon count image to achieve the desired variance. Additional zero-mean Gaussian noise was added with variance  $fp - f^2p$ . The standard deviation of the added noise was then  $\sqrt{fp(1 - f)}$ .

## S6.5 Applications

### S6.5.1 Color Filter Array

**Color imaging dataset** We conducted experiments using the Gehler-Shi dataset [54, 55] (implied license via explicit permission to use), which comprises 568 high-quality natural images. The dataset was partitioned into 461 training, 51 validation, and 56 test images, with each image subdivided into  $24 \times 24$  pixel patches. To establish a consistent baseline for illumination, we computed a white channel by summing the red, green, and blue channels, then normalized the dataset to achieve a mean of 1000 photons per pixel in the white channel, based on the training split mean. Signal-dependent Poisson noise was subsequently applied to all patches.

**Information content analysis** For mutual information estimation, we sampled 100,000 patches from the test set for fitting a PixelCNN, reserving 10,000 for evaluation. Conditional entropy

calculations were performed on clean images prior to synthetic Poisson noise application. We evaluated three distinct color filter array (CFA) designs: a Bayer pattern, a random configuration, and a learned pattern using the architecture in [53]. For each CFA design, we selected the minimum information estimate across the 20 replicates (since our estimator provides an upper bound) and the best prediction performance (lowest negative log likelihood on test data) to characterize system performance. Each replicate took  $\sim 3.5$ GB of memory. All replicates were trained in  $\sim 5$  hours on an Nvidia RTX A6000 GPU.

**Neural network architecture and training** Color image reconstruction was implemented using a bifurcated network architecture as proposed by Chakrabarti [53]. This approach processes  $24 \times 24$  pixel measurement patches through two parallel paths. The first path performs multiplicative operations in log-space with linear mixing, while the second employs convolutional layers with 128 filters. Each path generates 24 estimates per color value, which are then combined through learned weights for final reconstruction.

The network implementation features an  $8 \times 8$  repeated CFA pattern incorporating four channels (RGB and panchromatic). Training used the Adam optimizer ( $\beta_1 = 0.9$ ,  $\beta_2 = 0.999$ ) with a learning rate of  $1 \times 10^{-5}$  and a batch size of 128 patches, running for a maximum of 100,000 training steps with checkpoints every 5,000 steps. Training progress was monitored using a validation set comprising 10% of the training patches (100,000 patches total). The checkpoint achieving the lowest validation loss was selected for final reconstruction performance evaluation.

### S6.5.2 Black hole imaging

**Black hole dataset** For our site selection experiments, we generated a dataset of 100,000 synthetic black holes based on the physical models for black hole dynamics from [147]. Each synthetic black hole had a static envelope, right ascension, and source declination matching that of M87. The dynamic portion forming the accretion disk surrounding each black hole was modeled as a Gaussian random field generated by a different solution to an underlying anisotropic spatio-temporal diffusion partial differential equation with fixed diffusion and advection fields. Each black hole was formed by applying a Gaussian random field as a multiplicative perturbation to the static envelope, and normalized to have total flux of 1 Jansky. To simulate black hole imaging we selected combinations of four telescopes from the eight original telescope locations used in the Event Horizon Telescope 2017 array. We also included comparisons between reconstruction quality and information estimates for all 70 possible combinations of four telescopes (**Fig. S20**). For each combination we simulated radio telescope measurements including thermal noise using the methods described in [148].

**Information content analysis** For mutual information estimation from complex-valued radio telescope measurements we used the full Gaussian process model. Each complex-valued measurement with thermal noise was separated into real and imaginary components and concatenated into a single vector before being input to the model. The full Gaussian process was fit with 50,000 measurements and evaluated on a test set of 10,000 measurements with 100 bootstrapped estimates to form a 95% confidence interval. The conditional entropy was calculated based on the thermal noise statistics for each telescope array, modeled as Gaussian noise with independent and varying standard deviations at each measurement sample.

**Imaging inverse problem** Black hole images were reconstructed from simulated radio telescope measurements using a standard regularized maximum likelihood method with total variation regularization [148], with hyperparameters matching the implementation in [149]. Images were reconstructed for a 2,000 measurement subset of the test set used for information estimation. Each reconstruction was performed on the CPU and took  $\sim 10$ s.

### S6.5.3 Lensless imaging

**Natural image dataset** The CIFAR10 dataset [150] (implied license via permission to use) was used for the lensless imaging experiments. This dataset consists of 60,000 total images across 10 classes. To convert CIFAR10 image pixel values to synthetic photon counts, the dataset was scaled to have mean value equivalent to the desired photons per pixel. Encoded measurements for each lensless imaging system were generated by convolving (valid region, no zero padding) with the corresponding point spread function. The point spread functions for the one lens and four lens

encoders were modeled as Gaussian-blurred points. For the diffuser encoder, the point spread function is a downsampled version of an experimentally captured point spread function from DiffuserCam [59]. After convolution, synthetic Poisson noise was added to form the noisy encoded measurements.

**Information content analysis** For mutual information estimation, images from the CIFAR10 dataset were randomly selected in sets of 9 and tiled into  $3 \times 3$  grids before convolution with the encoding point spread functions. This tiling was implemented to prevent intensity falloff at the edges of a measurement, which occurs when convolving a non-tiled image due to the zero padding necessary to maintain measurement size. With tiling, image content was brought in uniformly at every point in the field of view, forming a spatially consistent texture. Information content was estimated using  $32 \times 32$  image patches, the same size as the original non-tiled CIFAR10 images. Patches were randomly sampled over the  $65 \times 65$  region corresponding to the valid convolution output and 10,000 patches were used for information estimation. Conditional entropy was calculated using clean images without synthetic Poisson noise. For each encoder and photon count combination, we trained four separate PixelCNN models to estimate information content, each including 100 bootstrap estimates with a test set of 1,500 images to form 95% confidence intervals. We selected the minimum information estimate across the replicated models to characterize system performance. Estimates were consistent across replicates, with less than 0.01 bits per pixel difference across replicates and confidence intervals smaller than the marker size in graphs.

**Image deconvolution** For the deconvolution task, images from the CIFAR10 dataset were convolved with an encoder. Then, Wiener deconvolution with an automatically tuned regularization parameter was used to reconstruct the original image from each convolved measurement. This was performed on the CPU, taking  $\sim 10 - 100$  ms per reconstruction.

Deconvolution is an ill-posed process and successful reconstructions with Wiener deconvolution require finite image extent. Therefore, instead of random tiling, we use non-tiled images with zero padding for this task. For each encoder and photon count combination, we evaluated image reconstruction metrics on a test set of 1,500 images. The images in this test set correspond to the center image of each of the  $3 \times 3$  tiled measurements used in the information estimation test set. The mean value for each metric was reported and 95% confidence intervals generated from 100 bootstrap estimates with the test set were smaller than the marker size.

**Image classification** In addition to the deconvolution task in the main paper, we study object classification using the same encoders. A simple CNN architecture, sufficiently powerful for regular CIFAR10 image classification is used. This consists of two convolutional layers (64 and 128 filters respectively with kernel size 5), each followed by a MaxPool, and two densely-connected layers, the first with 128 nodes and a ReLU activation, and the second with 10 layers and a Softmax activation for classification into the 10 classes. Classifiers were trained on an NVIDIA TITAN XP GPU using  $<5$ GB memory,  $\sim 10$  minutes training time per model.

The random tiling process used in mutual information estimation is used for the images in this task as well. The label for classification is based on the center image in the  $3 \times 3$  grid, for which maximum image content is present in the measurement. Classification is repeated 10 times for each photon count and encoder combination, from which the 90% confidence interval is generated.

#### S6.5.4 LED array microscopy

**Cell imaging dataset** We analyzed single leukocyte images and corresponding protein expression measurements from the Berkeley Single Cell Computational Microscopy (BSCCM) dataset [65] (CC0 1.0 Universal license). The dataset includes images acquired under multiple illumination conditions using an LED array microscope along with measurements of eight protein markers (CD3, CD19, CD56, CD123, HLA-DR, CD14, CD16, and CD45) obtained through antibody staining. To study performance at different signal levels, we simulated lower photon counts by adding synthetic Poisson noise to the original images.

**Neural network architecture and training** We developed a neural network to predict protein expression levels from single-cell images. The network uses a DenseNet121 [151] backbone pre-trained on ImageNet, modified to accept single-channel input by averaging the first convolutional layer's RGB weights. The backbone feeds into a global average pooling layer followed by eight

parallel fully-connected networks, each with two hidden layers. These networks output parameters for Gaussian mixture models corresponding to each protein marker, enabling direct evaluation of the negative log likelihood for target protein levels. Training used the Adam optimizer with a learning rate of  $5 \times 10^{-5}$  and batches of 16 images. A composite loss function summed the negative log likelihood across protein markers, with missing values masked out. Training proceeded for 4,000 steps per epoch and employed early stopping when validation loss failed to improve for 20 epochs. Typical trainings took 1-2 days on NVIDIA TITAN Xp GPUs with 12GB memory. 2-3 networks were trained in parallel sharing a single GPU.

**Information content analysis** To evaluate system performance, we performed 15 independent train-test splits of the data. For each split, we trained both a PixelCNN model to estimate information content and a protein prediction network. Information content was estimated using  $40 \times 40$  pixel patches uniformly sampled from the normalized images. For each illumination condition and photon count, we selected the minimum information estimate across the 15 replicates (since our estimator provides an upper bound) and the best prediction performance (lowest negative log likelihood on test data) to characterize system performance.

### S6.6 Information Driven Encoder Analysis Learning (IDEAL)

Using the Gehler-Shi dataset [54, 55] partitioned into training (461 images), validation (51 images), and test (56 images) sets, we extracted 100,000 patches of size  $24 \times 24$  pixels for training, along with 10,000 patches from the validation set. To establish consistent illumination conditions, the dataset was normalized to achieve a mean of 1000 photons per pixel in the white channel (sum of RGB channels) based on the training set statistics.

The mutual information between noiseless and noisy measurements was calculated using an analytic Gaussian approximation to ensure differentiability of the loss function with respect to the learnable parameters [53]. At each optimization step, we process a batch of 2304 measurement patches ( $24 \times 24$  pixels each), selected randomly from the Gehler-Shi dataset. These measurements were vectorized to compute their covariance matrix, whose log eigenvalues are used to estimate  $H(\mathbf{Y})$ . For numerical stability, any non-positive eigenvalues were set to  $10^{-8}$ . The batch size was chosen to be 2304, 4 times the number of pixels in a patch (576 pixels), as we found a batch of at least this size produces the most stable estimation.  $H(\mathbf{Y}|\mathbf{X})$  is calculated using the analytic formula detailed earlier (Sec. 23).

For the IDEAL optimization, we designed an  $8 \times 8$  repeating color filter array (CFA) pattern with four possible filters at each pixel: red, green, blue, and white. To learn which filter to place at each location, we used a temperature-based softmax approach [53]:

$$m(n) = \text{Softmax}[\alpha_t w(n)] \tag{51}$$

Here,  $m(n)$  is a 4-element vector that represents the probability of selecting each color filter at pixel location  $n$ . The learnable weights  $w(n)$  determine these probabilities through a softmax function whose sharpness is controlled by the temperature parameter  $\alpha_t = 1 + (\gamma t)^2$ , where  $t$  is the training iteration and  $\gamma = 0.001$ . Early in training when  $\alpha_t$  is small, the softmax produces soft probabilities that allow gradient-based learning. As training progresses and  $\alpha_t$  increases, these probabilities become increasingly binary, eventually forcing the network to select a single filter at each location.

The training procedure begins by passing clean image patches through the CFA pattern to generate noiseless measurements. Signal-dependent Poisson noise is then approximated using Gaussian noise with variance matching the signal intensity. We use the negative mutual information as our loss function, optimized using the AdamW optimizer (learning rate =  $10^{-4}$ ,  $\beta_1 = 0.9$ ,  $\beta_2 = 0.999$ ) until convergence. Training took  $\sim 3$  hours and  $\sim 1$  GB on a Nvidia RTX A6000 GPU.

To evaluate IDEAL’s ability to optimize a CFA, we computed the mutual information on the test set for the optimized pattern, as well as initial and intermediate patterns, using the estimation procedure described previously (See **Color Filter Array**). Reconstruction networks were subsequently trained for these three filters and evaluated following the protocol detailed above (See **Color Filter Array**).

## S6.7 1D simulations

We studied a simplified 1D imaging system with three key components: objects, encoders (point spread functions), and measurements. Objects were represented as periodic signals over a fixed spatial domain of 512 samples. Encoders were constrained to be bandlimited, non-negative, and infinitely periodic point spread functions that acted on objects through convolution. To ensure bandlimiting and enable stable optimization, encoders were parameterized in the Fourier domain using amplitude and phase components up to a specified bandwidth. The encoding process generated signals by convolving objects with these point spread functions. These signals were then integrated over fixed intervals (“pixels”) to simulate detector sampling, with independent additive Gaussian noise applied to each pixel to model measurement noise.

Information content was estimated using our PixelCNN-based estimator, requiring 1D signals to be reshaped into 2D arrays. Training datasets were generated by encoding random object instances drawn from specified distributions. To characterize encoder constraints, we mapped the space of achievable signals by optimizing encoders to match target signals, defined as points in the space of possible pixel measurements. This optimization minimized the L2 distance between encoded and target signals. We analyzed how information capacity varied with key system parameters. Signal-to-noise ratio effects were studied by varying noise standard deviation while keeping signal energy fixed. Bandwidth impact was assessed by adjusting the number of nonzero Fourier components in the encoder. Sampling density analysis involved changing the number of pixels while maintaining fixed bandwidth. These relationships were examined across different object distributions including single delta functions, multiple delta functions, and bandlimited noise patterns.

Encoder optimization employed stochastic gradient ascent on a Gaussian-approximated mutual information objective, with a proximal operator enforcing non-negativity and energy constraints on the point spread functions. All simulations were implemented in JAX for automatic differentiation and GPU acceleration.